UNIVERSITAT POLITÈCNICA DE VALÈNCIA

Control strategies for offshore wind farms based on PMSG wind turbines and HVdc connection with uncontrolled rectifier

Doctoral Dissertation

Author: Johel Rodríguez D´Derlée

Director: Ramón Blasco-Gimenez

July, 2013

CONTENTS

LIST OF FIGURES

LIST OF TABLES

Acknowledgements

The present work was supported by the Spanish Ministry of Science and Technology and the European Union FEDER funds under Grant DPI2007-64730. However, there are people who have influenced directly not only in my work but also the progress of this dissertation. Therefore, I would like to express my sincere gratitude to my advisor Professor Ramon Blasco-Gimenez for his friendship, meticulous guidance and support through my research work. Additionally, I also want to thank to the research team, particularly to Professor Salvador Año-Villalba and to Professor Soledad Bernal for sharing their knowledge and friendship during the time that we work together. Thanks are also to my colleagues and ai2 labmates for their active cooperation with whom I shared so many nice moments together. Finally, last but not least, I would like to thanks to my family in special to my wife and my daughter for their understanding, continuous support and encouragement.

Johel Rodríguez-D'Derlée
Valencia, January 2013

Abstract

The selection of the bulk power transmission technology in offshore wind farms is strongly related to the wind farm size and its distance to shore. Several alternatives can be evaluated depending on the rated power of the offshore wind farm, the transmission losses and the investment cost for constructing the transmission system. However, when is necessary to connect larger and more distant offshore wind farms; the best technological solution tends to the transmission system based on high-voltage and direct-current with line commutated converters (LCC-HVdc). This dissertation proposes the use of diode-based rectifiers as a technical alternative to replace the thyristor-based rectifiers in an LCC-HVdc link with unidirectional power flow. This alternative shows advantages with regard to lower conduction losses, lower installation costs and higher reliability. Nonetheless, as a counterpart the offshore ac-grid control performed by the thyristor-based HVdc rectifier is no longer available. This lack of control is compensated by using new control strategies over an offshore wind farm composed by wind turbines with permanent-magnet generators and fully-rated converters. The control strategies have been based mainly on the ability of the wind turbine grid-side converter to perform the control of the offshore ac-grid voltage and frequency. The performance has been evaluated by using PSCAD. Wherein, the most common grid disturbances have been used to demonstrate the fault-ride-through capability as well as the adequate steady state and transient response.

Keywords: *HVdc links, Offshore wind farms, Wind power generation, Power transmission.*

Resumen

La selección de la tecnología para la transmisión de grandes cantidades de potencia procedente de parques eólicos marinos está estrechamente relacionada con el tamaño del parque eólico y su distancia a la costa. Actualmente existen diversas alternativas que pueden ser evaluadas dependiendo de la potencia nominal del parque eólico, las perdidas de transmisión admisibles y la inversión necesaria para construir el sistema de transmisión. Sin embargo, a medida que el parque eólico aumenta sus dimensiones y su ubicación es mas distante de la costa, la mejor solución tecnológica para la transmisión de potencia tenderá al uso de de sistemas transmisión de alta tensión, en continua y basados en convertidores conmutados en línea (LCC-HVdc). Este trabajo de investigación propone el uso de rectificadores basados en diodo como una alternativa viable para reemplazar los rectificadores basados en tiristores en los enlaces LCC-HVdc con flujo unidireccional de potencia. Esta alternativa presenta ventajas relacionadas con la disminución en las perdidas de conducción, reducción en los costos de instalación y aumento en la confiabilidad del sistema. Sin embargo, como contraparte esto puede ser obtenido a costa de perder el control que ejerce el rectificador HVdc basado en tiristores sobre la red eléctrica en altamar. Este reporte muestra que la perdida del control en la red ac del parque eólico puede ser compensada a través de la implementación de nuevas estrategias de control; siempre y cuando el parque eólico marino esté compuesto por turbinas de viento basadas en generadores de imanes permanentes y convertidores de potencia nominal (full-rate converter). Las estrategias han sido basadas en la capacidad que

tiene el convertidor de la turbina para fijar la tensión y la frecuencia en la red de conexión en altamar. Además, el desempeño del sistema de control propuesto ha sido evaluado mediante el uso de PSCAD; donde se han usado las perturbaciones de red mas comunes para demostrar no solo la capacidad de recuperación de la red en presencia de huecos de tensión, sino también la estabilidad del sistema en estado estable y transitorio.

Palabras Clave: Enlace HVdc, Parque eólico Marino, Generación de Energía eólica, Transmisión de potencia.

Resum

La selecció de la tecnologia per a la transmissió de grans quantitats de potència procedent de parcs eòlics marins està estretament relacionada amb la grandària del parc eòlic i la seua distància a la costa. Actualment existeixen diverses alternatives que poden ser avaluades depenent de la potència nominal del parc eòlic, les perdudes de transmissió admissibles i la inversió necessària per a construir el sistema de transmissió. No obstant açò, a mesura que el parc eòlic augmenta les seues dimensions i la seua ubicació és més distant de la costa, la millor solució tecnològica per a la transmissió de potència tendirà a l'ús de sistemes de transmissió d'alta tensió, en contínua i basats en convertidors commutats en línia (LCC-HVdc). Aquest treball de recerca proposa l'ús de rectificadors basats en díode com una alternativa viable per a reemplaçar els rectificadors basats en tiristors en els enllaços LCC-HVdc amb flux unidireccional de potència. Aquesta alternativa presenta avantatges relacionats amb la disminució en les perdudes de conducció, reducció en els costos d'instal·lació i augment en la confiabilitat del sistema. Encara que aquest benefici pot ser obtingut a cost de perdre el control que exerceix el rectificador HVdc basat en tiristors sobre la xarxa elèctrica en alta mar. Aquest article mostra que la pèrdua del control en la xarxa ac del parc eòlic pot ser compensada a través de la implementació de noves estratègies de control; sempre que el parc eòlic marí estiga compost per turbines de vent basades en generadors d'imants permanents i convertidors de potència nominal (full-rate converter). Les estratègies han sigut basades en la capacitat que té el convertidor de la turbina per a fixar la tensió i la freqüència en la xarxa

de connexió en alta mar. Per altra banda , el comportament del sistema de control proposat ha sigut avaluat mitjançant l'ús de PSCAD; on s'han utilizat les pertorbacions de xarxa més comunes per a demostrar tant la capacitat de recuperació de la xarxa en presència de buits de tensió, com l'estabilitat del sistema en estat estable i transitori.

Paraules Clau: Enllaç HVdc, Parc eòlic en alta mar, Generació d'energia eòlica, Transmissió de potència.

CHAPTER 1

Thesis Overview

1.1 Introduction

At present, thyristor-based HVdc links is not only the most mature technology in use, but also the best economical solution to connect large offshore wind farms (rated power over 500 MW) located far away from the coastline (more than 100 km). Notwithstanding, the power electronics industry is continuously making new developments in order to increase the rated power of its components. Therefore, it is not inconceivable to think that some technologies employed nowadays for bulk power transmission, will no longer be the best option in the near future.

This is the case of the power transmission devices; wherein, the self-commutated voltage sourced converters (VSC) based on IGBT valves are considered as the most promising technology to be used for ac and dc transmission systems. Nonetheless, latest reports shows that the offshore wind farms that are currently under development tend to be larger, located in deeper waters and further away from the coastline; and consequently, the VSC technology is not completely mature to be used widely. In any case, it is important to state that the next generation of offshore wind farms not only will have to select its technology according to a more complex criterion; but also, many control strategies that could have not been carried out before, should be taken

into account.

An intermediate solution can be employed to avoid the use of active power electronics devices for transmission of large amount of power. This solution consists on considering the use of diode-bridge instead of the traditional HVdc rectifier. This is especially feasible if, on one hand, the offshore wind farm is composed of wind turbines with permanent magnet synchronous generators (PMSG); and on the other hand, the power flow can be considered as unidirectional.

The main advantages that can be achieved replacing the HVdc rectifier by a diode-bridge are: lower conduction losses, lower installation costs and higher reliability [4][5]. However, the HVdc rectifier normally sets the offshore ac grid voltage and frequency, and its replacement by a diode bridge could lead to loss of control on the offshore ac grid. Fortunately, this drawback can be compensated by applying different control strategies on the power converter of the wind turbines.

This dissertation introduces a proposal to solve the shortcomings of using diode-bridges as alternative to the traditional thyristor-based HVdc rectifier. The proposal is based on an offshore wind farm connected to the onshore grid through a modified version of the CIGRE benchmark model for HVdc studies. In addition, it has been demonstrated that by using the individual control of the wind turbines, it is possible to contribute to the grid support; compensating thereby, the lack of control caused by the use of a non-controlled HVdc rectifier [6][7].

The study is focused according to the latest trends reported for the offshore wind turbines. Therefore, the considered wind farm is composed exclusively by wind turbines based on PMSG and fully-rated converter. This is due to the fact that the fully-rated converters offer the best possibility to perform a tight control of the offshore grid. Additionally, the wind turbines with this technology are also considered as one of the best technical and economical options for distant offshore wind farms [8].

It is important to highlight that traditionally, the grid of a wind farm is supported by the power transmission devices; accordingly, the fully-rated converter of the wind turbine employs the back-end-converter side to set the power produced by the generator; whereas, the front-end-converter side is used to set the dc-link voltage shared by both sides of the converter. However, due to the use of a non-controlled HVdc

rectifier, the offshore grid is no longer supported by the power transmission devices. Therefore, the control strategy of the power converter must be redesigned.

The proposed solution is focused on redesigning the control strategy in order to support the offshore grid against electrical disturbances. The strategy uses the front-end-converter side of the wind turbine to support the grid; whereas, the dc-link voltage is set by using the back-end-converter side. Although, a similar proposal was carried out before to improve the grid support capability during grid faults [9]; the main contribution of this project is based on the use of the wind turbines to set the offshore grid when there is no active device for power transmission.

Finally, several reports have been developed in order to show the results achieved after evaluating the new control strategies [10][11][12][7][6]. Particularly, it is worth noticing that the proposed system is able to keep a similar behavior as the LCC-HVdc links. Moreover, the power transmission devices have been kept within their operational limits in presence of faults, with recovery times comparable to those achieved with controlled HVdc rectifiers.

The remainder of this dissertation is structured as follow. First, the state of the art and the research approach is used to define the main objectives and the scope. Next, the mathematical model of the selected wind turbine, the offshore wind farm and the HVdc link is defined. According to the models defined, a control strategy is proposed. Then, the implementation of the control is carried out assuming both, an aggregated model and a distributed model of the whole offshore wind farm. At this stage, the steady state and transient response is analyzed for grid compliancy. Finally, conclusions and future works summarize the important aspects and contributions provided by this dissertation and the future tasks that could be carried out.

1.2 Offshore Wind Farms

Offshore wind power expansion is paramount for a sustainable energy future around the world. Recent studies state that there is enough wind around Europe's coasts to power Europe over seven times [13]; therefore, it is not inconceivable that in the future a big portion of the world's energy would come from offshore wind power. In

order to exploit this abundant energy resource, the European experience shows a clear trend to increase the offshore wind energy penetration: larger wind farms located at deep waters far away from the coastline [13].

There are several advantages in placing wind turbines offshore as opposed to onshore. It has been demonstrated that offshore wind is more constant and stronger than on land; therefore, offshore wind turbines generate electricity 70-90% of the time [14]. Moreover environmental analyses have shown that offshore wind farms have had a reduced negative impact on marine life [15].

Offshore wind industry is flourishing, as shown in recent studies of the European Wind Energy Association (EWEA); who estimate that by 2020 the offshore wind installed capacity will be more than 7000 MW [13]. Currently (2012) offshore wind farms are concentrated in North Western Europe, primarily Denmark, the United Kingdom, the Netherlands, Sweden and Germany. However In the next years a number of other countries as USA, Canada, Brazil, China, India, Japan and Korea are planning to include offshore wind energy in their grids [13].

As technology develops and experience is gained, the offshore wind industry will move into deeper waters and further away from shore. The European Wind Energy Association has found that for the next years, the offshore wind farms proposed by project developers, will move gradually beyond the so-called 20:20 envelope (20m water depth, 20 km from shore) [13]. Therefore the next generation of offshore wind farms will have to deal with at least three challenges. First, the design of bigger and more reliable wind turbines in order to reduce the time and costs associated with offshore maintenance operations. Second, the development of an efficient, profitable and reliable power transmission system to deliver all generated power to onshore grid. Third, the development of both, wind turbine foundations for deep water and floating offshore wind turbine technology.

In the following sections the offshore wind turbine technologies and the offshore power transmission approaches will be introduced. Besides, these sections will be focused not only on the state of the art, but also on the latest trends in offshore wind energy.

1.2.1 Offshore wind turbine technologies

Wind turbine manufacturers have demonstrated that there exist many approaches to extract the wind energy efficiently. However, since the wind industry moved out of the coast, the technological challenges related to the offshore power generation and distribution have been studied in order to define the most optimal technology to extract the offshore wind energy.

Currently, the race to develop the best offshore wind turbine has clear technological trends; where, reliability and power rating are the main topics to improve in new wind turbine designs. Besides, a reliable wind turbine means fewer faults, less maintenance and better control systems. Hence, an appropriated wind turbine design for offshore applications will have to take into account aerodynamic, mechanical and electrical aspects. Offshore wind energy conversion systems (WECS) could be classified according to the four aspects shown in figure 1.1, i.e. wind turbine rotor, drive train, wind turbine generator and power converter [16][17].

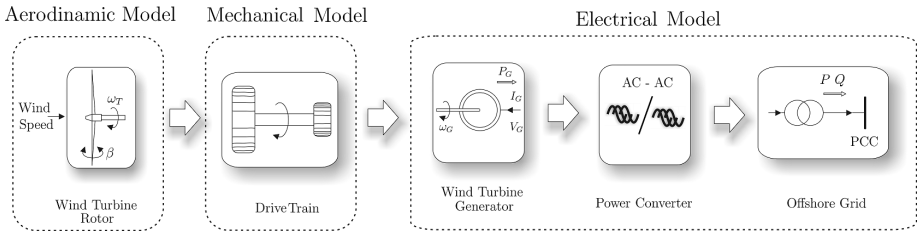

Figure 1.1: Wind turbine technologies

Wind turbine rotor

Regarding to wind turbine rotor, variable speed wind turbines (VSWT) with pitch and torque control are the most appropriate for offshore wind farms. This is due mainly to the capability of alleviate loads. Moreover, the VSWT with an optimal pitch and torque control could extract the power efficiently [18].

Wind turbine drive train

Equally important is the wind-turbine drive train, which could be direct-drive or with gear-box. Due to high maintenance costs in offshore wind farms, wind turbine manufacturers tends to avoid rotating components in order to reduce the mechanical stress and hence the mechanical wear [19]. As a consequence, failure points and maintenance tasks are minimized and therefore, the efficiency, reliability and service life of the equipment are increased.

Currently, the gearboxes with double and three stages are still used by important offshore wind turbine manufacturers. Although there are many advantages using direct-drive drive train, the gearbox selection is closely related with the generator and the power converter used [19]. Therefore, the selection is not evident and factors as cost, weight or size should be taken into account. Some characteristics of main multi-megawatts offshore wind turbines manufacturers are compared in table 1.1.

Wind turbine generator

With regard to the wind turbine generator, at least four types of generators are used in multi-megawatt wind turbines. These are: squirrel cage induction generator (SCIG), doubly feed induction generator (DFIG), electrical excited synchronous generator (EESG) and permanent magnets synchronous generator (PMSG) [20][21].

The SCIG was very popular because of its mechanical simplicity, low maintenance, high efficiency and robust construction. Additionally, the SCIG has low specific mass (kg/kW) and a small outer diameter (low number of poles), hence lower cost [17]. Their main disadvantage is that a gearbox is required in the drive train [21].

Most of the currently installed wind generation systems are based on DFIG. The DFIG has similar specific mass and outer diameter than their SCIG equivalent. But, the main advantage is that the power converter for a DFIG is around 30% of their rated power. Therefore, it is cheaper than the used for a direct-drive generator. However, DFIG is less attractive for offshore application due to maintenance tasks related to their brushes and the necessity of using a gearbox in the drive train [21].

With respect to the EESG, the main advantage is that it does not need a gearbox.

Therefore, that means high reliability, less noise and less cost. Compared to the PMSG, the EESG has better flux control capabilities, thus allows the minimization of losses in different power ranges. Furthermore, it does not require the use of permanent magnets, which would represent a large fraction of the generator costs, and might quickly suffer from performance loss in harsh atmospheric conditions [17].

The main drawback is due to the high cost of the EESG power converter; as it has to process all the generator power, then, the converter requires more expensive power electronic components and it needs intensive cooling. Moreover, their high specific mass (kg/kW) and large outer diameter (high number of poles) means higher cost and more weight [17]. This weight is partially balanced by the elimination of the gearbox.

Regarding to the PMSG, the main advantage is that it does not needs a gearbox and is brushless. So, that means high reliability, less noise and less cost. In addition, there is an improvement in the thermal characteristics of the PM machine due to the absence of the field losses. Moreover, the PMSG full power converter decouples totally the generator from the grid. Hence, grid disturbances have no direct effect on the generator [21].

On the other hand, the high cost of the permanent magnet material and large outer diameter (high number of poles) are the main disadvantages. However this is balanced through a lower specific mass (kg/kW) and the elimination of the gearbox. Other shortcomings are the demagnetization of the permanent magnet at high temp due to severe loading or short circuit and the difficulties to handle them in manufacture and transportation.

Notice that converters used for a PMSG are fully rated converter (100% of rated power) and therefore more expensive than DFIG converters [22]. However, more stringent code regulations and falling of prices in power electronic components have lead to an increase on the use of fully rated converter in wind turbines. Moreover, this extra cost is balanced by the elimination of the gearbox.

Wind turbine power converter

The three types of fully rate converter widely used for electrical power delivery are: Back-to-back two level converters, multilevel converters and matrix converters

[20][21][22]. The most conventional bidirectional power converter is the Back-to-Back two level converters. It consists of two identical voltage source converters (VSC) and a capacitor which is connected in between them. The main advantage is the control flexibility thanks to dc-link capacitor, which provides a separate control capability on both generator and grid side. However, the main drawbacks are the losses due to the high switching frequency of the pulse width modulation (PWM) [23].

In contrast with Back-to-Back two level converters, multi level converter can operate at both fundamental switching frequency and high switching frequency PWM. Hence, lower switching frequency means lower switching losses and higher efficiency [24].

Besides, in multilevel converters the output voltage has very low distortion due to the high number of power semiconductors [24]. However, it causes an increment in the overall system cost, and increases the complexity of the control strategies [25].

With respect to matrix converter, some limitations related to the maximum output voltage and the high conducting losses are the main shortcomings. Furthermore, although matrix converters has been used as research prototype [26], nowadays, there are not commercial wind turbines with matrix converters.

Summing up, Table 1.1 shows the technologies used by the major manufacturers of offshore wind turbines. From this table is possible to infer that the trend of the next generation of offshore wind turbines will have the following characteristics: Firstly, variable-speed wind turbines with pitch and toque control for an optimal power extraction; Secondly, the employment of brushless generators and minimal stages in the drive train in order to diminish the maintenance tasks; Lastly, the use of fully rated converter in order to decouple the generator from the grid, improving the grid integration and the grid code compliancy.

1.2.2 Offshore power transmission

Technical and economical aspects of offshore transmission systems are constantly changing due to the increase of semiconductor power rating and falling prices of power electronics. Currently, two alternatives are available to connect large offshore wind farms to the main grid, i.e. high voltage ac transmission (HVac) and high voltage dc transmission (HVdc) [3]. However, depending of the power rating and the distance

Table 1.1: Major manufacturers offering Multi-MW offshore wind turbines with fully rated converter

Manufacturer	WT Turbine Model	Rated Power	Rotor Diameter	Generator Type	Drive-Train
GAMESA	G14X*	5.0 MW	145 m	PMSG	2-Stages
GE WIND	4.1-113	4.1 MW	113 m	PMSG	Direct Drive
SIEMENS	SWT-6.0-154	6.0 MW	154 m	PMSG	Direct Drive
AREVA	Multibrid M5000-135	5.0 MW	135 m	PMSG	Planetary Gear
VESTAS	V164*	8.0 MW	164 m	PMSG	4-Stages
REPOWER	6M	6.15 MW	126 m	DFIG	3-Stages
XEMC	XD115/5MW	5.0 MW	115 m	PMSG	Direct Drive
BARD	BARD6.5*	2x3.25 MW	122 m	PMSG	Two Drive-Shaft
ALSTOM	HALIADE 150-6MW	6.0 MW	150 m	PMSG	Direct Drive
SINOVEL	SL6000	6.0 MW	128 m	SCIG	Pararell Axes Gear Transmission
NORDEX	N150/6000	6.0 MW	150 m	PMSG	Direct Drive

* Prototype

from the coast the HVac transmission could present serious disadvantages compared to the HVdc transmission [3].

The main drawbacks of HVac transmission are the dielectric losses and the reactive power produced by the ac transmission cable. These shortcomings can be compensated stepping up the transmission voltage level. However, due to the intrinsic characteristics of the cable and electrical components, there are physical limits that cannot be exceeded with current technologies, i.e. 220 MW at 132 kV,with a maximum distance of around 100km (without offshore compensation). Notice that, outside of these limits, the power transmission capability is severely reduced by the large amount of reactive power that is absorbed by the cable. According to reports of loss evaluation in HVac and HVdc systems [1], a 400 kV cable can deliver 900 MW for distances up to 25 km, but at 50 km of distance the maximum power is reduced to 800 MW and finally at 100 km no active power can be delivered at all.

In contrast, a feasible solution to connect larger and distant offshore wind farms is the HVdc transmission [1]. Figure 1.2 shows the comparison between the HVac and HVdc transmission with regard to both, the total power rating and transmission distance [1]. Notice that the HVdc transmission option is divided into the two technologies commercially available, i.e. line-commutated converter (LCC-HVdc) and voltage source converter (VSC-HVdc).

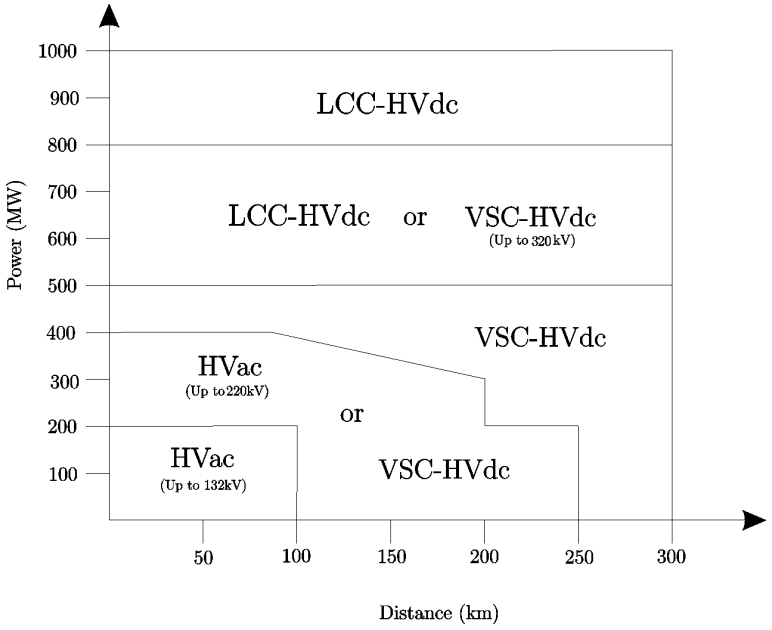

Figure 1.2: High voltage transmission technologies as function of power rating and distance

The LCC-HVdc is a mature converter technology based on thyristor valves, which has been in use since the 1970's and has been well documented by many authors in different books [2][27][28][29]. LCC-HVdc can be used for the transmission of significant amounts of power at large distances having low losses [1]. However, their main drawbacks are the huge converter station for both onshore and the offshore sides [3] and the lack of independent control for active and reactive power. Additionally, the thyristor valves in the converter requires reactive power that have to be delivered by capacitor banks and the STATCOM. Moreover, the dc-voltage at the terminals of

the converter has to be set by changing the ac-voltage via load tap changer on the converter transformer.

As a counterpart, the VSC-HVdc is a relatively new technology but with sufficient maturity to be commercialized. This technology represents an alternative to conventional ac-transmission, and their use in different offshore applications is the most feasible proof of success in bulk-power transmission [3]. Currently, the available trademarks of the VSC-HVdc technology are HVDC-Plus developed by Siemens [30], Light-HVDC developed by ABB [31] and HVDC Maxsine developed by ALSTOM [32].

The power converters of this technology are based on the use of insulate-gate bipolar transistors (IGBTs); and because of their characteristics they are an excellent alternative for offshore applications. One of the most significant benefits of using this technology is their important role in the stability of the system. This is due to the fact that the VSC-HVdc rectifier is capable to provide offshore grid voltage and reactive power control [33][34].

Recent developments carried out by ABB in the DolWin1 link have shown that the Light-HVDC is a proven technology capable of transmit up to 800MW at 320kV. In addition, the configurations based on converters connected in series and multiterminal topologies [32][3][31] show the continuos interest to enhance this technology for very-high-power transmission. But, the reality is that VSC-HVdc converters exhibit higher losses than their LCC-HVdc counterpart [1]. Besides, although it is clear that there are several advantages in VSC-HVdc transmission, at present the technological limitations in terms of power and voltage rating are still the main drawback of this technology.

Figure 1.2 shows the power ranges and distances for the feasibility of the three transmission technologies commented before. Furthermore, their main advantages and shortcomings are summarized in table 1.2.

As a conclusion, the VSC-HVdc technology shows clear advantages related with offshore grid stability; furthermore, is economically suitable to transmit power on relative long distances. However, for larger and more distant offshore wind farms, LCC-HVdc are still the best technical alternative for power transmission.

Table 1.2: Comparison of the HVac and HVdc transmission technologies [1][2][3]

	HVac	LCC-HVdc	VSC-HVdc
Maximun Available Capacity per System	800 MW at 400 kV 380 MW at 220 kV 220 MW at 132 kV	Up to 2000 MW In submarine transmission	Up to 400 MW Installed 800 MW Announced
Voltage Level	132 kV Installed 220 kV and 400 kV under development	Up to ± 500 kV	Up to ± 150 kV ±320 kV Announced
Black-Start Capability	- Yes -	- No -	- Yes -
Technical Capability for Network Support	- No - SVC are required to supply reactive power	- No - Capacitor banks or STATCOMS are required to supply reactive power to the valves	- Yes - Reactive power can be generated or absorbed by the VSC devices
Decoupling of Connected Networks	- No -	- Yes -	- Yes -
Space Requirements for Offshore Substation	Smallest size	Biggest size	Medium size
Total System Losses	Distance dependent	2% - 3% [1] Plus requirements for ancillary services offshore	4% - 6% [1]
Instalation Cost	Small for station (only transformer) High cost for cable	High cost for station (transformers, filters, capacitors banks, thyristor valves,...) Low cost for cable	High cost for station 30% - 40% more expensive than LCC solution due to power electronic components Cable more expensive than LCC

1.2.3 Technical feasibility of diode based HVdc transmission

Several researchers have proposed the use of diode based HVdc rectifiers for links with unidirectional power flow [35][4][5]. On one hand, the advantages are related to less conduction losses, less installation cost and higher reliability. But, on the other hand, drawbacks such as the lack of control in both sides of the diode rectifiers and the absence of protection systems have been important deterrents to the use of this technology.

The reported proposals designed to solve the drawbacks of this technology can be summarized in the following three aspects [5][35]. Firstly, an standalone generator unit adequately regulated to compensate the lack of control caused by the diode-based rectifiers. Secondly, a protection strategy based on limit the maximum current delivered to the HVdc link with the transient inductance of the generator. Lastly, the regulation of the dc-link voltage by means of a current control loop in the onshore inverter.

Currently, these proposals are not sufficient to accomplish successfully the grid codes. This is due to the slow recovery time of the system (around 1.5 s) in presence of dc-line faults [35]. In addition, the continuous use of the onshore inverter to regulate of the dc-link voltage can lead on lower efficiency and moreover increases the probability of commutation failure.

Nonetheless, the proposal of using diode based HVdc rectifiers becomes more attractive if the total costs of the HVdc and HVac transmission systems are compared [1]. The trade-off analysis shows that since the installation and the maintenance costs are much higher in offshore installations and therefore, any reduction in aspects such as equipment weight, maintenance requirements or transmission losses, will have a more evident impact over the transmission costs.

According to the latest development, the multi-MW wind turbines are capable of perform the grid support according to the most stringent grid codes. Therefore, the solution proposed initially can be replaced by the possibility of considering the following scenario: An offshore wind farm with unidirectional power flow (diode based HVdc link) and wind turbines with a wide range of control possibilities.

Notice that in this scenario the wind turbines can be used not only to set the grid parameters but also to limit the delivered power to the onshore station. Accordingly, the use of the transformer tap changer can be avoided, and the recovery time of the system in presence of faults will be defined by the wind turbine response. Additionally, the system does not have to supply reactive power to the rectifier valves. Hence, some ancillary services such as the STATCOM can be eliminated.

1.3 Research Approach

High Voltage dc-transmission systems based on line commutated converters (LCC-HVdc) are probably, the best technological solution to connect large offshore wind farms, from 1 GW upwards and located at more than 100km in the sea. However, based on the technical feasibility of the diode-based HVdc transmission system [35][4][5], it is possible to suggest the following changes: First, replacing the LCC-HVdc offshore rectifier by a non-controlled diode-based rectifier. Second, eliminating the static compensator (STATCOM). Last, eliminating the transformer tap changer in the HVdc rectifier. Notice that these changes can lead to a significant reduction of the installation, but as a counterpart the offshore ac-grid control is lost.

The aforementioned state of the art suggests that there is strong scientific evidence to think that the lack of control can be solved by using the control flexibility of the wind turbine. However, due to the coupled nature of the proposal, the new system cannot be analyzed isolatedly. Therefore, any control strategy, should be focused not only on the mere control of the wind turbine; but also, on the offshore grid and the HVdc dynamics as a whole.

According to the current technologies available for offshore power generation, the wind turbines based on permanent magnet synchronous generators (PMSG) and fully rated back-to-back voltage source converters (VSC), can be considered as an outstanding technology with regards to the control flexibility. But, as a consequence of these changes, the system to be controlled becomes more complex, non-linear, of a high order and is not control-affine.

1.3.1 Thesis goal and objectives

The goal of the thesis is the development of advanced strategies to control not only the grid parameters, but also the power generation of a large offshore wind farm. The offshore wind farm will be conformed by wind turbines with permanent magnet synchronous generators (PMSG) and Back-to-Back two level voltage source converters (VSC). Besides, all generated power will be delivered through an LCC-HVdc link with an uncontrolled rectifier (diode based).
In order to achieve the thesis goal, the objectives can be summarized as follows:

- Development of a control system in order to replace the controlled HVdc rectifier for an uncontrolled rectifier (diode based).
- Development of a control system in order to eliminate the offshore voltage and reactive power control systems (STATCOM).
- Development of a control system in order to eliminate the transformer tap changer in the HVdc Rectifier.
- Development of a distributed control strategy in order to achieve an adequate performance of the offshore wind farm.

1.4 Thesis Outline

In this chapter the state of the art and trends related to offshore wind energy technology have been described. In addition, a diode based HVdc rectifier was presented as an alternative for offshore wind power transmission. Nonetheless, its technical feasibility has to be proved. Therefore, according to the proposed objectives, the following chapters will describe the tasks carried out to achieve them.
Chapter two describes the mathematical models used to define the control strategies. Although, the aerodynamic model of the wind turbine is defined, the chapter will be focused on the electrical behavior of the wind turbine, the offshore grid and the HVdc system used to deliver the produced power to the onshore grid.

In chapter three the constraints imposed by different modes of operation are analyzed. According to these constraints the control strategy will be divided on wind turbine aerodynamic control, wind turbine generator control and power inverter control for grid integration. The strategy will be defined for both, connected and islanded operation mode.

The control system for the aggregated model of an offshore wind farm will be carried out in chapter four. By using the models defined in chapter two, some control loops will be performed in order to integrate adequately the whole wind farm to the offshore grid. The stability of the control loops will be analyzed, as well as several tests in order to validate the control performance.

Similarly, chapter five will describe the control of the distributed model of an offshore wind farm. Assuming the same strategy, the goal will be to guarantee the stability and the performance of the whole wind farm when multiple wind turbines are connected to the grid.

Finally, chapter six defines the conclusions as a summary of the important aspects of this work. Future works are also mentioned in order to state possible tasks to be developed in the same research line.

CHAPTER 2

System Modelling

2.1 Introduction

Dynamic models of offshore wind farms are essential for power system studies and for the development of new control strategies. The criteria to select the complexity of the model will depend on the significant impact of the variables on the phenomena being studied.

A typical offshore wind farm consists of a number of wind turbines, connected to a point of common coupling (PCC), and this in turn, connected to a power transmission system to deliver the power to the onshore grid. Figure 2.1 shows the proposed offshore wind farm, where (n) PMSG-based wind turbines with fully rated converters are connected to the offshore ac-grid. Moreover, a non-controlled rectifier (i.e. a 12-pulse diode-based HVdc-rectifier) is connected to the offshore ac-grid by means of a transformer (T_R) without tap changer. The reactive power compensation for both, the non-controlled HVdc-rectifier and the transformer (T_R) is carried out by the capacitor and filter bank (Z_{FR}). Finally, a dc transmission line (submarine cable) will connect the offshore rectifier with the onshore LCC-HVdc inverter. The onshore inverter is a standard 12-pulse thyristor-based converter [2].

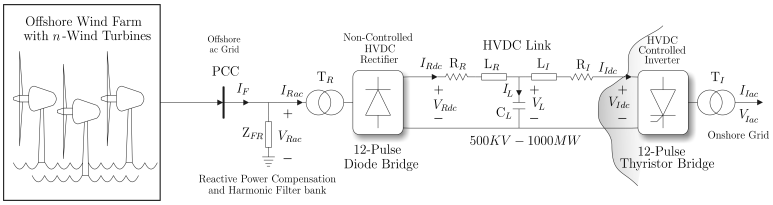

Figure 2.1: Proposed offshore wind farm

In the following sections the models of different components, and the notation used in figure 2.1 will be specified. First of all, the wind turbine dynamics will be described according to their aerodynamic model, mechanical model and electrical model. Then, the aggregated model, distributed model and clustered model of an offshore wind farm will be presented. Lastly, the model of a HVdc link with a diode-based-rectifier will be defined.

2.2 Wind Turbine Modelling

The proposed offshore wind farm shown in figure 2.1 consists of (n) wind turbines based on PMSGs. Mechanical and electrical parameters of the wind turbine components are extrapolated from [19]. Wherein, the generator is scaled in [pu] to deliver 5MW and the rotor diameter is augmented according to the necessary aerodynamic torque to produce this power. A simplified block diagram of the wind turbine components is presented in figure 2.2; as shown in this scheme, the elements of the wind turbine have been classified as aerodynamics, mechanical and electrical components. Additionally, the wind resource will be considered as a mean wind speed applied uniformly to the rotor blades.

The aerodynamic model uses the wind speed to compute the aerodynamic torque produced by the wind turbine rotor (T_a). Then, this torque is transmitted to the generator by means of the drive train. The direct-drive drive train links the wind turbine rotor with the generator and can be modelled as two rigid bodies coupled by a shaft. A PMSG model is used to perform the conversion of the mechanical power

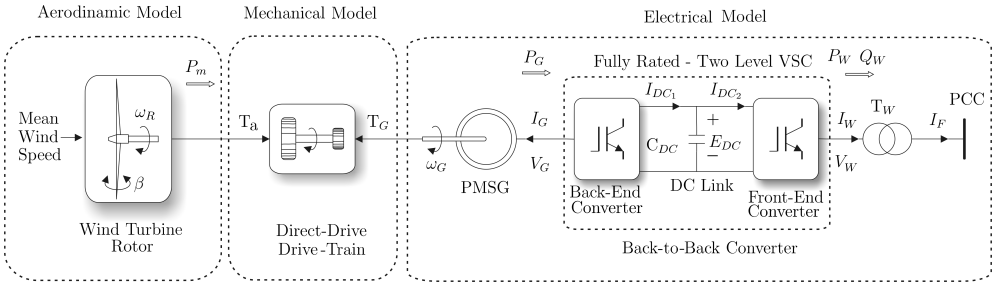

Figure 2.2: Wind turbine components

(P_m) into the electrical power (P_G) delivered by the wind turbine generator. The electrical ac/ac transformation is carried out by a three-phase fully-rated converter. Finally, the output voltage of the front-end converter is stepped up by the wind turbine transformer (T_W).

2.2.1 Aerodynamic model

The wind turbine rotor converts the kinetic wind power into mechanical-rotational power. The relationship between wind speed (V_{wind}) in [m/ s] and the mechanical power (P_m) produced by the wind turbine rotor in [N m/ s], is defined as follows [14]:

$$P_m = \frac{1}{2}\rho\ A\ C_P(\lambda, \beta)\ V_{wind}^3 \tag{2.1}$$

where (ρ) is the air density in [kg/ m^3] and (A) is the area in [m^2] covered by the wind turbine rotor of radius (R) defined in [m]. The power coefficient (C_P) is a non-dimensional term specific for each wind turbine. It depends on the wind rotor characteristics and its value is defined according to the blade pitch angle (β) and the tip-speed ratio (λ). The tip-speed ratio is a non-dimensional parameter defined by:

$$\lambda = \frac{\omega_R\ R}{V_{wind}} \tag{2.2}$$

where (ω_R) is the angular speed of the wind turbine rotor in [rad/ s].
The block diagram of the aerodynamic model defined in the equation (2.1) is shown in figure 2.3.

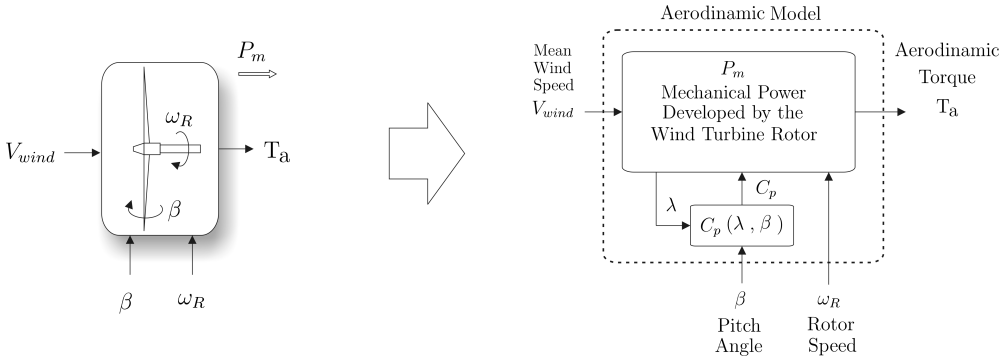

Figure 2.3: Wind turbine aerodynamic model

The value of (C_P) represents the ability of a wind turbine to capture wind energy and it has a maximum achievable theoretical limit ($C_{P\,\max} = 0.593$) known as Betz limit [14]. A mathematical approximation of the (C_P) expression can be defined as follows:

$$C_P = 0.5176\left(\frac{116}{\lambda_0} - 0.4\beta - 5\right)\cdot e^{\frac{-21}{\lambda_0}} + 0.0068\lambda \tag{2.3}$$

This expression was proposed initially by Heier [36], but its values have been changed slightly in order to match better with the data provided by the wind turbine manufacturers. According to Heier [36], the (λ_0) value can be obtained from:

$$\frac{1}{\lambda_0} = \frac{1}{\lambda + 0.08\beta} - \frac{0.035}{\beta^3 + 1} \tag{2.4}$$

Neglecting mechanical and electrical losses, the aerodynamic torque (T_a) developed by the wind turbine rotor can be defined in [N m] as follows:

$$T_a = \frac{P_m}{\omega_R} \tag{2.5}$$

2.2.2 Mechanical model

The mechanical model of the direct-drive drive train is described by the moments of inertia of the wind turbine rotor (J_R) and the wind turbine generator (J_G). Both are defined in [kg m^2] and are coupled by a rigid shaft as shown in figure 2.4.

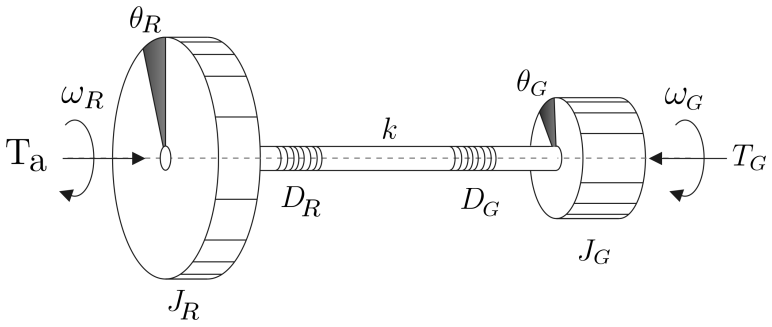

Figure 2.4: Two-masses model of the drive train

Defining the damping of the wind turbine rotor and generator as (D_R) and (D_G) respectively, the drive train dynamics can be described as follows:

$$T_a - D_R \frac{d\theta_R}{dt} - k\,(\theta_R - \theta_G) = J_R \frac{d^2\theta_R}{dt^2} \tag{2.6}$$

$$T_G - D_G \frac{d\theta_G}{dt} + k\,(\theta_R - \theta_G) = J_G \frac{d^2\theta_G}{dt^2} \tag{2.7}$$

Notice that mechanical losses are neglected, (D_R) and (D_G) are defined in [N m/ rad/ s], and (k) represents the shaft stiffness in [N m/ rad]. Moreover, (θ_R) and (θ_G) are the rotational angle of the rotor and the generator defined in [rad]. Hence, the angular speeds of the rotor and the generator in [rad/ s] are:

$$\omega_R = \frac{d\theta_R}{dt} \tag{2.8}$$

$$\omega_G = \frac{d\theta_G}{dt} \tag{2.9}$$

2.2.3 Electrical model

Permanent magnet synchronous generator

A permanent magnet synchronous generator (PMSG) is used to convert the mechanical-rotational power into electrical power. The equivalent circuit of the generator is shown in figure 2.5.

The dynamics of the generator can be written as relations of the d and q components of generator voltage (V_G) in [V] and current (I_G) in [A]. The generator in a synchronous-

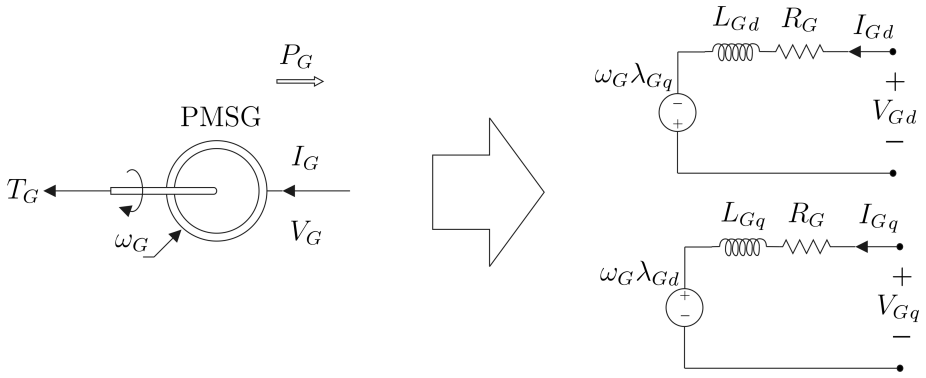

Figure 2.5: PMSG model

frame (d-q axis) rotating at (ω_G) can be described as:

$$V_{Gd} = R_G I_{Gd} + L_{Gd}\frac{dI_{Gd}}{dt} - \omega_G \lambda_{Gq} \tag{2.10}$$

$$V_{Gq} = R_G I_{Gq} + L_{Gq}\frac{dI_{Gq}}{dt} + \omega_G \lambda_{Gd} \tag{2.11}$$

where (R_G) is the stator resistance in [Ω]; (L_{Gd}) and (L_{Gq}) correspond to the d and q components of the stator leakage inductances in [H]. The flux linkages (λ_{Gd}) and (λ_{Gq}) can be defined in [Wb] by the following equations:

$$\lambda_{Gd} = L_{Gd}\ I_{Gd} + \lambda_m \tag{2.12}$$

$$\lambda_{Gq} = L_{Gq}\ I_{Gq} \tag{2.13}$$

where (λ_m) is the flux linkage in [Wb] due to the permanent magnets of the rotor. Neglecting losses, the electrical torque developed by the generator (T_G) in [N m] is:

$$T_G = 3p\ \ (\lambda_{Gd} I_{Gq} - \lambda_{Gq} I_{Gd}) \tag{2.14}$$

where (p) is the number of poles pairs of the generator. In addition, the electric power (P_G) would be:

$$P_G = \omega_G\ T_G = -3\,(V_{Gd} I_{Gd} + V_{Gq} I_{Gq}) \tag{2.15}$$

Back-to-back converter

The fully rated back-to-back converter extracts the energy from the generator and delivers it to the offshore ac-grid. In order to analyze the back-to-back converter, it could be divided onto back-end converter, dc-link and front-end converter as shown in figure 2.6.

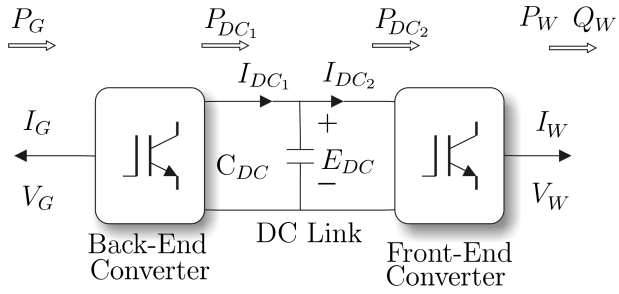

Figure 2.6: Fully-Rated back-to-back converter

Notice that (V_G) is the voltage at the terminals of the generator and (I_G) the current produced by the generator; while (V_W) and (I_W) correspond to the grid voltage and the current delivered to the grid respectively. Neglecting losses in the back-end converter, the following power balance equation can be obtained from the generator side:

$$P_G = P_{DC1} \Longrightarrow -3\left(V_{Gd}I_{Gd} + V_{Gq}I_{Gq}\right) = E_{DC}I_{DC1} \tag{2.16}$$

Likewise, the power balance equation from the grid side could be written as follows:

$$P_{DC2} = P_W \Longrightarrow E_{DC}I_{DC2} = 3\left(V_{Wd}I_{Fd} + V_{Wq}I_{Fq}\right) \tag{2.17}$$

The voltage (E_{DC}) dynamics is defined by the equation of the dc-link capacitance (C_{DC}) and it can be expressed as:

$$I_{DC1} - I_{DC2} = C_{DC}\frac{dE_{DC}}{dt} \tag{2.18}$$

Transformer and offshore grid model

The front-end converter voltage is stepped up by the wind turbine transformer (T_W) which is modelled neglecting its shunt branches. This is due to the fact that shunt

impedances are considered much larger than series impedances and therefore its influence on the power dynamic can be neglected [2]. Figure 2.7 shows the electrical diagram of the wind turbine inverter connected to the offshore ac-grid through transformer (T_W). Notice that the transformer is represented by their equivalent impedance, where (R_{T_W}) and (L_{T_W}) represent the resistive and the inductive component respectively.

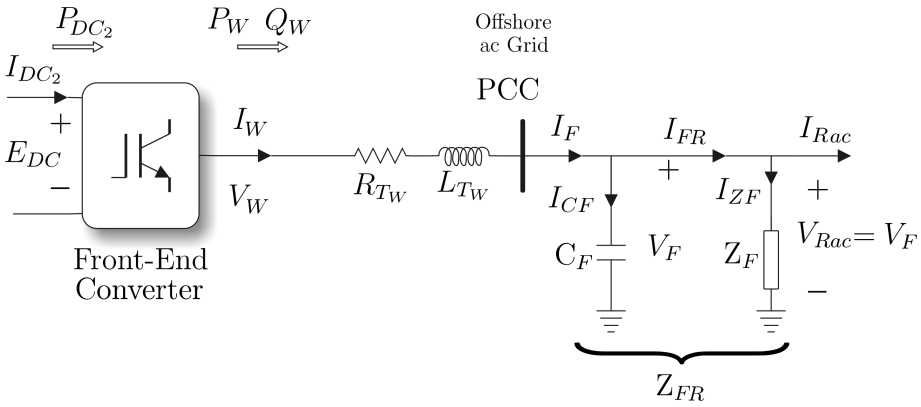

Figure 2.7: Wind turbine grid integration

The dynamics of this simplified model can be written in synchronous dq coordinates as follows:

$$V_{Wd} = R_{T_W} I_{Fd} + L_{T_W} \frac{dI_{Fd}}{dt} - L_{T_W} I_{Fq} \omega_{dq} + V_{Fd} \tag{2.19}$$

$$V_{Wq} = R_{T_W} I_{Fq} + L_{T_W} \frac{dI_{Fq}}{dt} + L_{T_W} I_{Fd} \omega_{dq} + V_{Fq} \tag{2.20}$$

where (ω_{dq}) is the frequency in [rad/s] of the rotational synchronous-frame, (V_W) and (V_F) are the grid voltages expressed in [V] and (I_G) is the current delivered by the wind turbine expressed in [A]. Notice that frequency (ω_{dq}) is not defined in figure 2.7, therefore, it could represent any synchronous reference frame. The dynamics of the grid voltage (V_F) will be defined in the following sections.

2.3 Offshore Wind Farm Modelling

Once obtained the wind turbine single model, it is possible to develop an equivalent model for the whole offshore wind farm. In order to reduce the model complexity, the aggregation techniques are used by several authors [37][14][38] to obtain valid models for a wide operation range during steady state and transient functioning. However, in order to analyze the mutual interaction between wind turbines, a multi-machine model of the wind farm is required; hence, the distributed and the clustered model of the wind farm will be developed.

In the following sections, the aggregated, distributed and clustered model of an offshore wind farm will be presented. The models have been carried out under the following simplifying assumptions: First, offshore line impedances are negligible in comparison to the wind turbine transformer leakage reactance. Second, the wind turbine transformer shunt branches are not considered. Third, losses in power converters are not considered. Last, the point of common coupling (PCC) of the offshore ac-grid, will be modeled by the capacitor (C_F) which represents the reactive power compensation of the wind turbines transformers and the capacitive part of the filter bank (Z_{FR}).

2.3.1 Aggregated model of an offshore wind farm

The proposed aggregated model consists of a single wind turbine model equivalent to the whole offshore wind farm. The power delivered by the aggregated model must be equivalent to the sum of the (n) wind turbines of the offshore wind farm.

The following relationship for the total power produced by the offshore wind farm can be obtained from the power balance defined in equation 2.17.

$$\text{Total power produced by the offshore wind farm} \qquad P_{Wn} = \sum_{i=1}^{n} P_{DC2i} = \sum_{i=1}^{n} E_{DCi} I_{DC2i} \tag{2.21}$$

where (P_{Wn}) is the total power of the offshore wind farm and the subscript (i) represents the (i-th) wind turbine with $i = 1, \ldots, n \in \mathbb{N}$. Considering identical wind turbine parameters and the same wind speed affecting all wind turbines, the total

power of the offshore wind farm (P_{Wn}) can be represented as the aggregation of (n) wind turbines as follows:

$$P_{Wn} = n\,(I_{DC2})\,E_{DC} \tag{2.22}$$

Note the following two aspects. First, the (E_{DC}) value should correspond to the wind turbine dc-link voltage assuming an adequate control, i.e. ($E_{DC} = E_{DCrat}$); the rated value of the dc-link voltage is 5.4 kV. Second, the current (I_{DC2}) has to be scaled to be (n) times in concordance with the wind turbines included in the aggregation procedure.

For the proposed aggregated model, both aerodynamics and mechanical parameters will be the same as in the individual wind turbines. Hence, the dynamics equations will be the same as previously mentioned in section (2.2.1) and (2.2.2). Regarding to the electrical dynamics, only the rated power of the front-end converter is modified to be (n) times larger. Using the equation (2.17), with (V_W) and (V_F) as the grid voltages, and (I_F) as the current delivered by the aggregated wind turbine, the power balance of the aggregated front-end converter can be defined as follows:

$$P_{Wn} = 3\,(V_{Wd}I_{Fd} + V_{Wq}I_{Fq}) \tag{2.23}$$

The electrical dynamics of the PMSG, the back-end converter and the dc-link will be the same defined in section (2.2.3). Figure 2.8 shows the aggregated model equivalent of an offshore wind farm with (n) wind turbines.

Notice that the aggregated wind turbine transformer (T_{Wn}) is scaled in (pu) and it will be represented by ($R_{T_{Wn}}$) and ($L_{T_{Wn}}$). The rated voltage of the transformer (T_W) will be considered as voltage-base, while the power-base will be the total power of the offshore wind farm (i.e. (n) times the rated power of the wind turbine).

Summarizing, the following equations represent the aggregated model of a wind farm with (n) wind turbines connected to the offshore grid.

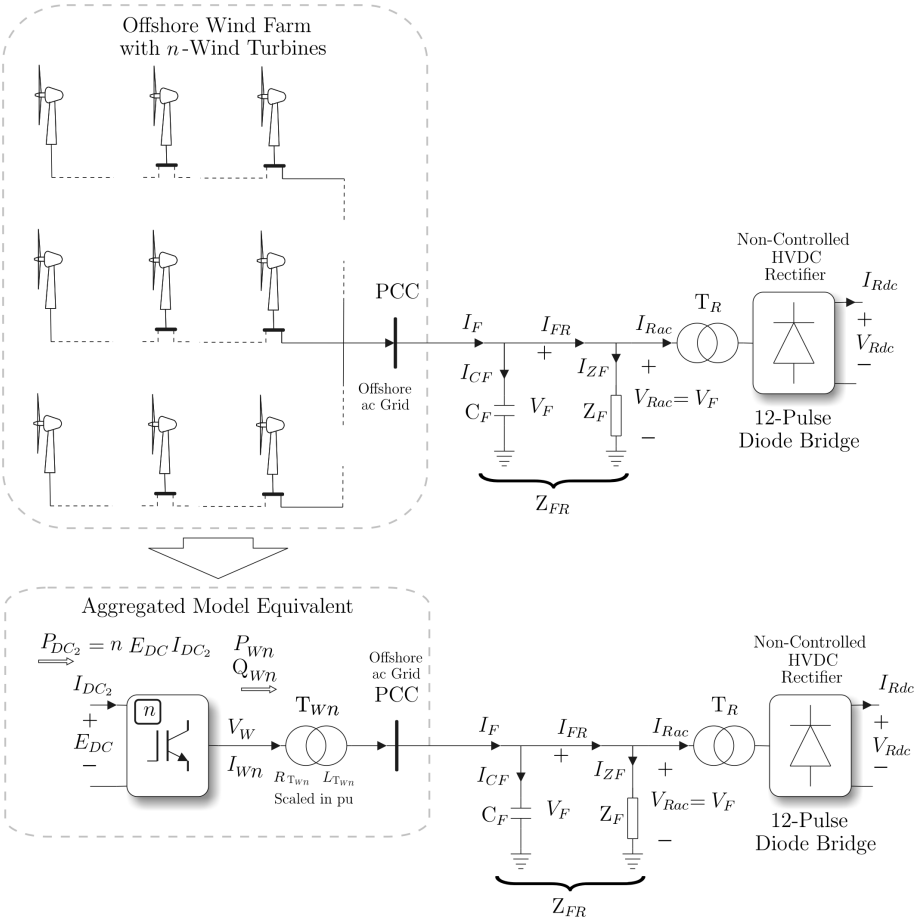

Figure 2.8: Aggregated model of (n) wind turbines

PMSG dynamic in a synchronous-frame rotating at (ω_G)

$$\frac{dI_{Gd}}{dt} = -\frac{R_G}{L_{Gd}} I_{Gd} + \frac{L_{Gq}}{L_{Gd}} \omega_G I_{Gq} + \frac{1}{L_{Gd}} V_{Gd} \tag{2.24}$$

$$\frac{dI_{Gq}}{dt} = -\frac{L_{Gd}}{L_{Gq}} \omega_G I_{Gd} - \frac{R_G}{L_{Gq}} I_{Gq} + \frac{1}{L_{Gq}} V_{Gq} - \frac{1}{L_{Gq}} \omega_G \lambda_m \tag{2.25}$$

Power balance at back-end converter

$$P_G = -3\left(V_{Gd} I_{Gi} + V_{Gi} I_{Gi}\right) \tag{2.26}$$

$$P_{DC1} = E_{DC} I_{DC1} \tag{2.27}$$

Back-to-back dc-link dynamic

$$\frac{dE_{DC}}{dt} = \frac{1}{C_{DC}} \left(I_{DC1} - I_{DC2}\right) \tag{2.28}$$

Power balance at front-end converter

$$P_{DC2} = n\left(E_{DC} I_{DC2}\right) \tag{2.29}$$

$$P_{DC2} = P_{Wn} \tag{2.30}$$

$$P_{Wn} = 3\left(V_{Wd} I_{Fd} + V_{Wq} I_{Fq}\right) \tag{2.31}$$

Dynamics of the front-end grid integration in a synchronous-frame rotating at (ω_{dq})

$$\frac{d}{dt} I_{Fd} = -\frac{R_{T_{Wn}}}{L_{T_{Wn}}} I_{Fd} + \omega_{dq} I_{Fq} + \frac{1}{L_{T_W}} V_{Wd} - \frac{1}{L_{T_W}} V_{Fd} \tag{2.32}$$

$$\frac{d}{dt} I_{Fq} = -\omega_{dq} I_{Fd} - \frac{R_{T_{Wn}}}{L_{T_{Wn}}} I_{Fq} + \frac{1}{L_{T_W}} V_{Wq} - \frac{1}{L_{T_W}} V_{Fq} \tag{2.33}$$

Dynamics of the offshore grid voltage in a synchronous-frame rotating at (ω_{dq})

$$\frac{d}{dt} V_{Fd} = \frac{1}{C_F} I_{Fd} - \frac{1}{C_F} I_{FRd} + \omega_{dq} V_{Fq} \tag{2.34}$$

$$\frac{d}{dt} V_{Fq} = \frac{1}{C_F} I_{Fq} - \frac{1}{C_F} I_{FRq} - \omega_{dq} V_{Fd} \tag{2.35}$$

2.3.2 Distributed model of an offshore wind farm

The aggregated model defined in section (2.3.1), is not sufficient to analyze the mutual interaction between wind turbines and the phenomena related with their transient functioning; hence, a more complex system description is required. Figure 2.9 shows the distributed model of an offshore wind farm with (n) wind turbines.

Aerodynamic and mechanical parameters will be the same as in the individual wind turbines. Hence, their equations will be the same above mentioned in section (2.2.1) and (2.2.2). Figure 2.9 shows the corresponding electrical diagram for the distributed model of an offshore wind farm.

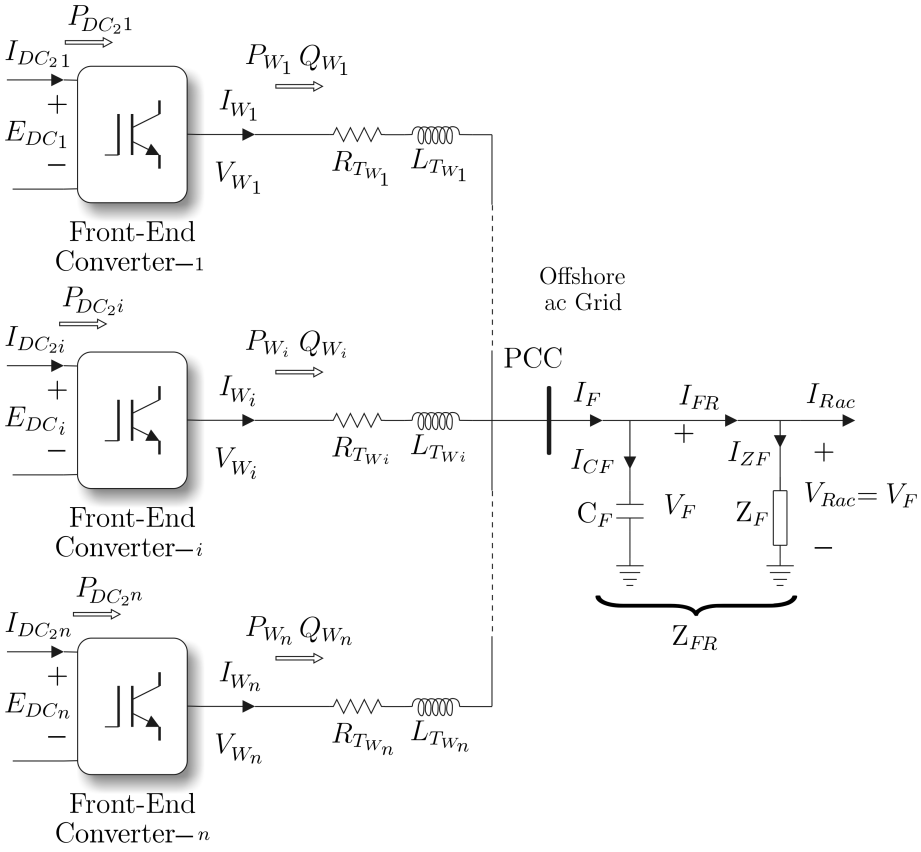

Figure 2.9: Distributed model of (n) wind turbines

The following equations represent the electrical model of the $(i\text{-}th)$ wind turbine

connected to the point of common coupling (PCC) of the offshore ac-grid.

PMSG dynamic in a synchronous-frame rotating at (ω_{Gi})

$$\frac{dI_{Gid}}{dt} = -\frac{R_{Gi}}{L_{Gid}} I_{Gid} + \frac{L_{Gqi}}{L_{Gdi}} \omega_{Gi} I_{Giq} + \frac{1}{L_{Gid}} V_{Gid} \tag{2.36}$$

$$\frac{dI_{Giq}}{dt} = -\frac{L_{Gid}}{L_{Giq}} \omega_{Gi} I_{Gid} - \frac{R_{Gi}}{L_{Giq}} I_{Giq} + \frac{1}{L_{Giq}} V_{Giq} - \frac{1}{L_{Giq}} \omega_{Gi} \lambda_{mi} \tag{2.37}$$

Power balance at back-end converter

$$P_{Gi} = -3\left(V_{Gid} I_{Gid} + V_{Giq} I_{Giq}\right) \tag{2.38}$$

$$P_{DC1i} = E_{DCi} I_{DC1i} \tag{2.39}$$

Back-to-back dc-link dynamic

$$I_{DC1i} - I_{DC2i} = C_{DCi} \frac{dE_{DCi}}{dt} \tag{2.40}$$

Power balance at front-end converter

$$P_{DC2i} = E_{DCi} I_{DC2i} \tag{2.41}$$

$$P_{Wi} = 3\left(V_{Wdi} I_{Wdi} + V_{Wqi} I_{Wqi}\right) \tag{2.42}$$

Dynamics of the front-end grid integration in a synchronous-frame rotating at (ω_{dq})

$$\frac{d}{dt} I_{Wdi} = -\frac{R_{T_{Wi}}}{L_{T_{W}i}} I_{Wdi} + \omega_{dq} I_{Wqi} + \frac{1}{L_{T_{Wi}}} V_{Wdi} - \frac{1}{L_{T_{Wi}}} V_{Fd} \tag{2.43}$$

$$\frac{d}{dt} I_{Wqi} = -\omega_{dq} I_{Wdi} - \frac{R_{T_{W}i}}{L_{T_{Wi}}} I_{Wqi} + \frac{1}{L_{T_{Wi}}} V_{Wqi} - \frac{1}{L_{T_{Wi}}} V_{Fq} \tag{2.44}$$

Dynamics of the offshore grid voltage in a synchronous-frame rotating at (ω_{dq})

$$\frac{d}{dt} V_{Fd} = \frac{1}{C_F} \sum_{k=1}^{n} I_{Wdk} - \frac{1}{C_F} I_{FRd} + \omega_{dq} V_{Fq} \tag{2.45}$$

$$\frac{d}{dt} V_{Fq} = \frac{1}{C_F} \sum_{k=1}^{n} I_{Wqk} - \frac{1}{C_F} I_{FRq} - \omega_{dq} V_{Fd} \tag{2.46}$$

2.3.3 Clustered model of an offshore wind farm

For large offshore wind farm, there exist an intermediate solution to reduce the distributed model. Considering similar parameters in some wind turbines, it is possible to group them as a cluster. In a cluster representation, a group of wind turbines in the wind farm could be lumped into one cluster. Then, each cluster can be replaced by a single aggregated equivalent unit with the power rating equivalent to the sum of the individual wind turbines power rating. The number of clusters in the aggregated model depends on the accuracy required and the phenomena being studied.

The aggregation technique explained in section (2.3.1) can be used to develop the clustered model of an offshore wind farm with (n) wind turbines. Furthermore, the offshore wind farm cluster representation, is itself a distributed model, hence, both have the same dynamic but with different power rating and quantity of wind turbines. Figure 2.10 shows the clustered model of an offshore wind farm with (n) wind turbines lumped into (m) clusters.

The following equations represent the electrical model of the j^{th} cluster of wind turbines connected to the point of common coupling (PCC) of the offshore ac-grid. Note that there are (n_j) wind turbines lumped into the j^{th} cluster, and the total wind turbines belonging to the wind farm are $n = \sum_{j=1}^{m}(n_j)$.

PMSG dynamic in a synchronous-frame rotating at (ω_{Gi})

$$\frac{dI_{Gjd}}{dt} = -\frac{R_{Gj}}{L_{Gjd}} I_{Gjd} + \frac{L_{Gqj}}{L_{Gdj}} \omega_{Gj} I_{Gjq} + \frac{1}{L_{Gjd}} V_{Gjd} \tag{2.47}$$

$$\frac{dI_{Gjq}}{dt} = -\frac{L_{Gjd}}{L_{Gjq}} \omega_{Gj} I_{Gjd} - \frac{R_{Gj}}{L_{Gjq}} I_{Gjq} + \frac{1}{L_{Gjq}} V_{Gjq} - \frac{1}{L_{Gjq}} \omega_{Gj} \lambda_{mj} \tag{2.48}$$

Power balance at back-end converter

$$P_{Gj} = -3\left(V_{Gjd} I_{Gjd} + V_{Gjq} I_{Gjq}\right) \tag{2.49}$$

$$P_{DC1j} = E_{DCj} I_{DC1j} \tag{2.50}$$

Back-to-back dc-link dynamic

$$I_{DC1j} - I_{DC2j} = C_{DCj} \frac{dE_{DCj}}{dt} \tag{2.51}$$

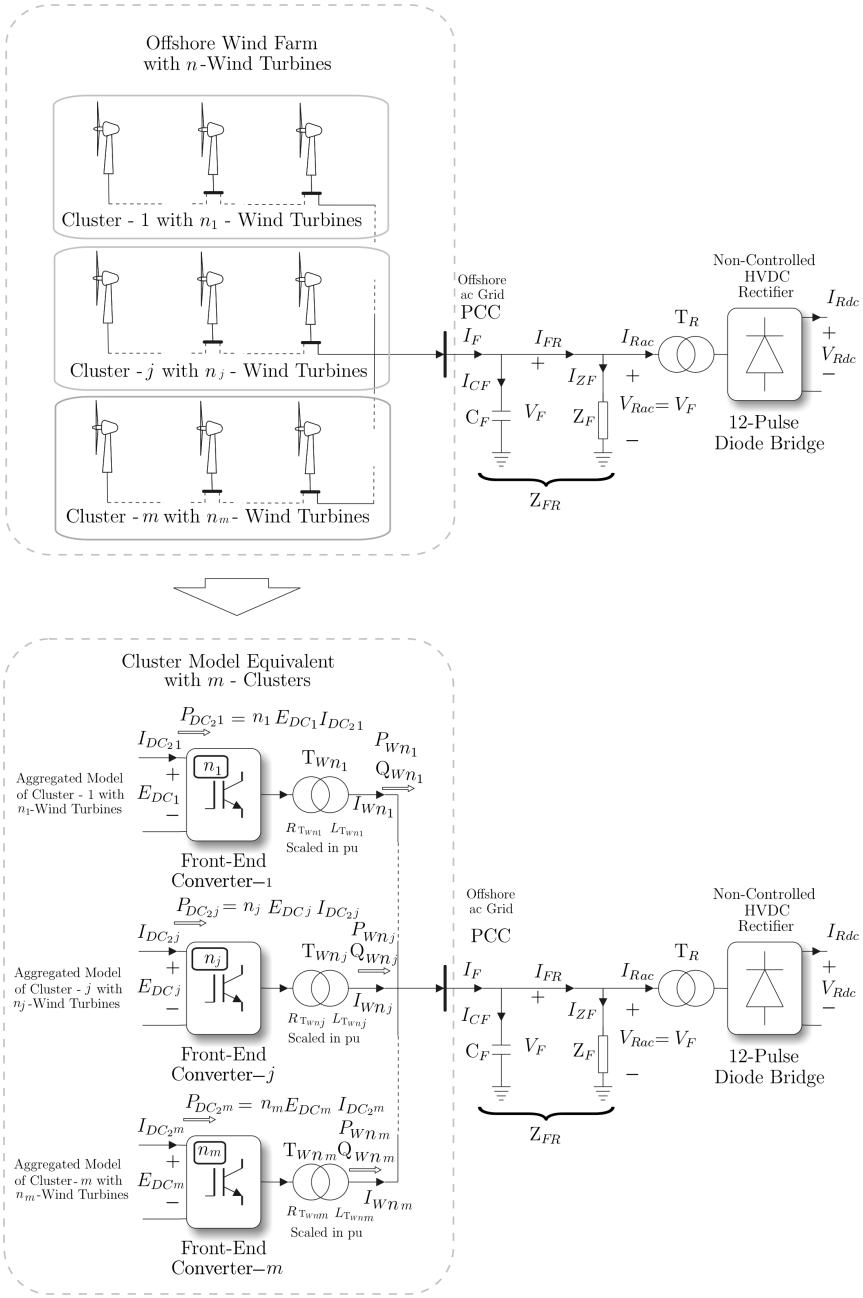

Figure 2.10: Clustered model of (n) wind turbines lumped into (m) clusters

Power balance at front-end converter

$$P_{DC2j} = E_{DCj}\left(I_{DC2j}\right) n_j \tag{2.52}$$

$$P_{Wj} = 3\left(V_{Wdj} I_{Wdj} + V_{Wqj} I_{Wqj}\right) \tag{2.53}$$

Dynamics of the front-end grid integration in a synchronous-frame rotating at (ω_{dq})

$$\frac{d}{dt} I_{Wdj} = -\frac{R_{T_{Wnj}}}{L_{T_{Wnj}}} I_{Wdj} + \omega_{dq} I_{Wqj} + \frac{1}{L_{T_{Wnj}}} V_{Wdj} - \frac{1}{L_{T_{Wnj}}} V_{Fd} \tag{2.54}$$

$$\frac{d}{dt} I_{Wqj} = -\omega_{dq} I_{Wdj} - \frac{R_{T_{Wnj}}}{L_{T_{Wnj}}} I_{Wqj} + \frac{1}{L_{T_{Wnj}}} V_{Wqj} - \frac{1}{L_{T_{Wnj}}} V_{Fq} \tag{2.55}$$

Dynamics of the offshore grid voltage in a synchronous-frame rotating at (ω_{dq})

$$\frac{d}{dt} V_{Fd} = \frac{1}{C_F} \sum_{k=1}^{m} I_{Wdk} - \frac{1}{C_F} I_{FRd} + \omega_{dq} V_{Fq} \tag{2.56}$$

$$\frac{d}{dt} V_{Fq} = \frac{1}{C_F} \sum_{k=1}^{m} I_{Wqk} - \frac{1}{C_F} I_{FRq} - \omega_{dq} V_{Fd} \tag{2.57}$$

2.4 Diode Based HVdc-Link Modelling

Diode-based HVdc rectifiers for links with unidirectional power flow have been proposed previously by several researchers [35][4][5]. The main components of the proposed HVdc transmission system are shown in figure 2.11.

It is worth noting that the system configuration and several of the employed parameters have been taken from the CIGRE benchmark model for HVdc system studies [39]. However, the offshore rectifier harmonic and reactive power compensation bank has been modified with respect to the original CIGRE benchmark model in order to supply the required reactive power at the offshore ac-grid voltage level (193.6 kV L-N rms). The new filter parameters are shown in table 2.1.

In the following sections the dynamic of the reactive compensation bank (Z_{FR}), the diode-based rectifier, the dc transmission cable and the onshore inverter will be described.

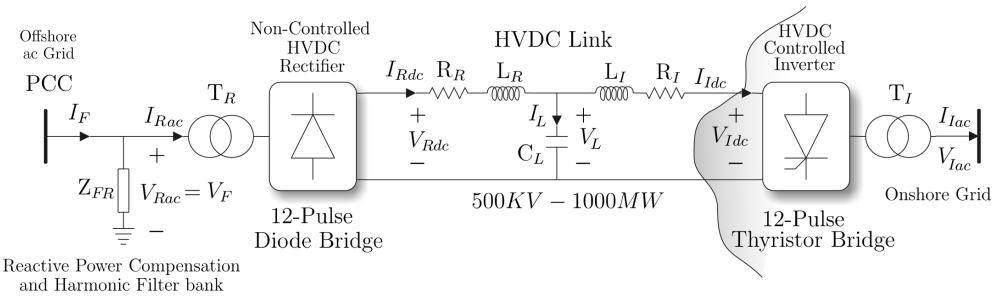

Figure 2.11: Diode-Based HVdc link

2.4.1 Offshore capacitor and filter bank

The reactive power compensation for both, the non-controlled HVdc-rectifier and the transformer (T_R) is carried out by the capacitor and the filter bank (Z_{FR}). Figure 2.12 shows the electrical diagram of the the filter bank (Z_{FR}) proposed by CIGRE [39] as a benchmark model for HVdc system studies.

The electrical dynamics of the capacitors and the filter bank (Z_{FR}) shown in figure 2.12, can be defined as follows:

$$\frac{d}{dt}V_F = \frac{1}{C_F}I_F - \frac{1}{C_F}I_{FR} \tag{2.58}$$

$$\frac{d}{dt}V_{Ca1} = \frac{1}{R_{a2}C_{a1}}V_F - \frac{1}{R_{a2}C_{a1}}V_{Ca1} + \frac{1}{C_{a1}}I_{La} \tag{2.59}$$

$$\frac{d}{dt}V_{Ca2} = \frac{1}{C_{a2}}I_{La} \tag{2.60}$$

$$\frac{d}{dt}I_{La} = \frac{1}{L_a}V_F - \frac{1}{L_a}V_{Ca1} - \frac{1}{L_a}V_{Ca2} - \frac{R_{a1}}{L_a}I_{La} \tag{2.61}$$

$$\frac{d}{dt}V_{Cb} = \frac{1}{R_bC_b}V_F - \frac{1}{R_bC_b}V_{Cb} + \frac{1}{C_b}I_{Lb} \tag{2.62}$$

$$\frac{d}{dt}I_{Lb} = \frac{1}{L_b}V_F - \frac{1}{L_b}V_{Cb} \tag{2.63}$$

The dynamics of (Z_{FR}) can be written in synchronous dq coordinates rotating at (ω_{dq}) as follows:

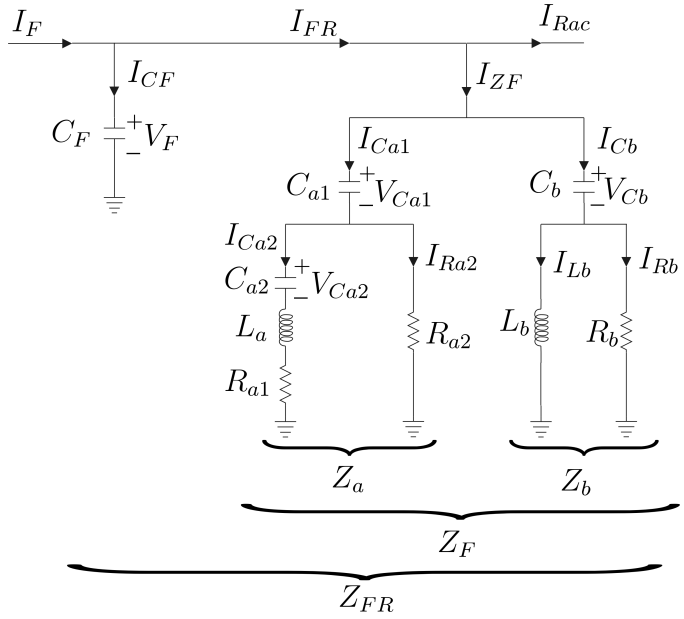

Figure 2.12: Offshore capacitor and filter bank (Z_{FR})

$$\frac{d}{dt}V_{Fd} = \frac{1}{C_F}I_{Fd} - \frac{1}{C_F}I_{FRd} + \omega_{dq}V_{Fq} \tag{2.64}$$

$$\frac{d}{dt}V_{Fq} = \frac{1}{C_F}I_{Fq} - \frac{1}{C_F}I_{FRq} - \omega_{dq}V_{Fd} \tag{2.65}$$

$$\frac{d}{dt}V_{Ca1d} = -\tfrac{1}{R_{a2}C_{a1}}V_{Ca1d} + \omega_{dq}V_{Ca1q} + \tfrac{1}{C_{a1}}I_{Lad} + \tfrac{1}{R_{a2}C_{a1}}V_{Fd} \tag{2.66}$$

$$\frac{d}{dt}V_{Ca1q} = -\omega_{dq}V_{Ca1d} - \tfrac{1}{R_{a2}C_{a1}}V_{Ca1q} + \tfrac{1}{C_{a1}}I_{Laq} + \tfrac{1}{R_{a2}C_{a1}}V_{Fq} \tag{2.67}$$

$$\frac{d}{dt}V_{Ca2d} = \omega_{dq}V_{Ca2q} + \tfrac{1}{C_{a2}}I_{Lad} \tag{2.68}$$

$$\frac{d}{dt}V_{Ca2q} = -\omega_{dq}V_{Ca2d} + \tfrac{1}{C_{a2}}I_{Laq} \tag{2.69}$$

$$\frac{d}{dt}I_{Lad} = -\tfrac{1}{L_a}V_{Ca1d} - \tfrac{1}{L_a}V_{Ca2d} - \tfrac{R_{a1}}{L_a}I_{Lad} + \omega_{dq}I_{Laq} + \tfrac{1}{L_a}V_{Fd} \tag{2.70}$$

$$\frac{d}{dt}I_{Laq} = -\tfrac{1}{L_a}V_{Ca1q} - \tfrac{1}{L_a}V_{Ca2q} - \omega_{dq}I_{Lad} - \tfrac{R_{a1}}{L_a}I_{Laq} + \tfrac{1}{L_a}V_{Fq} \tag{2.71}$$

$$\frac{d}{dt}V_{Cbd} = -\tfrac{1}{R_bC_b}V_{Cbd} + \omega_{dq}V_{Cbq} + \tfrac{1}{C_b}I_{Lbd} + \tfrac{1}{R_bC_b}V_{Fd} \tag{2.72}$$

$$\frac{d}{dt}V_{Cbq} = -\omega_{dq}V_{Cbd} - \tfrac{1}{R_bC_b}V_{Cbq} + \tfrac{1}{C_b}I_{Lbq} + \tfrac{1}{R_bC_b}V_{Fq} \tag{2.73}$$

$$\frac{d}{dt}I_{Lbd} = -\frac{1}{L_b}V_{Cbd} + \omega_{dq}I_{Lbq} + \frac{1}{L_b}V_{Fd} \quad (2.74)$$

$$\frac{d}{dt}I_{Lbq} = -\frac{1}{L_b}V_{Cbq} - \omega_{dq}I_{Lbd} + \frac{1}{L_b}V_{Fq} \quad (2.75)$$

The new value set for the reactive power compensation and harmonic filter bank (Z_{FR}) is shown in table 2.1.

Table 2.1: Parameters of the offshore rectifier filter bank

Component	Units	Original Value	New Value
C_F	(μF)	3.342	2.856
C_{a1}	(μF)	6.685	5.714
C_{a2}	(μF)	74.28	63.49
R_{a1}	(Ω)	29.76	34.82
R_{a2}	(Ω)	261.87	306.4
L_a	(mH)	136.4	159.6
C_b	(μF)	6.685	5.714
R_b	(Ω)	83.32	97.49
L_b	(mH)	13.6	15.91

2.4.2 Offshore diode-based rectifier

Offshore rectifier is composed by a 12^{th}-pulse diode-based rectifier as can be seen in figure 2.13. The bridges are two three-phase diode bridges in series on the dc-side and parallel on the ac-side. Two banks of transformers, one connected $Y-Y$ and the other $Y-\Delta$, are used to supply the bridges with a three-phase voltage displacement of 30° between them.

If the voltages from ac-side are balanced and the HVdc diode rectifier is conducting, then, the relationship between the HVdc rectifier dc voltage (V_{Rdc}) and the offshore grid voltage (V_{Fd}) can be defined as [2]:

$$V_{Rdc} = \frac{3B\sqrt{6}}{\pi}NV_{Fd} - \frac{3B}{\pi}\omega_F L_{T_R} I_{Rdc} \quad (2.76)$$

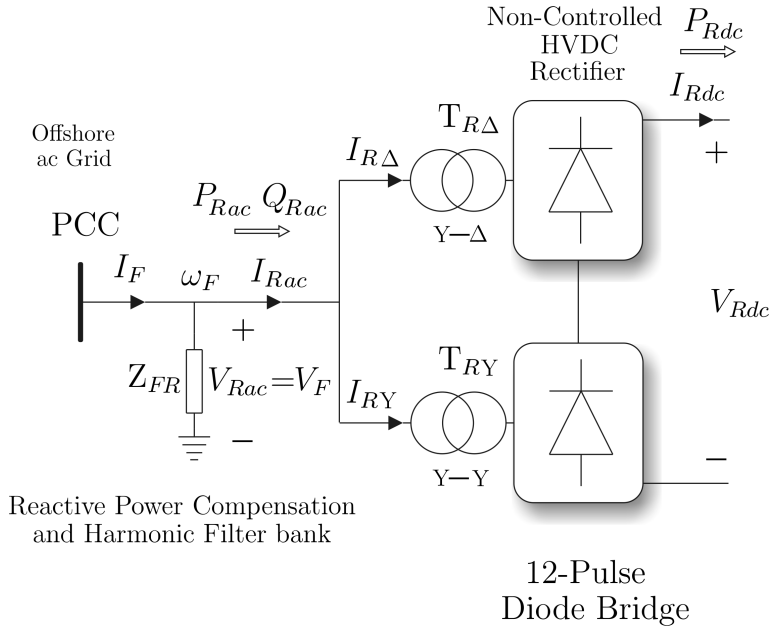

Figure 2.13: Offshore diode rectifier

where, (B) is the number of bridges in series (for 12-pulse diode bridge $B = 2$), (N) is the turns ratio of the rectifier transformer, (L_{T_R}) is the leakage inductance of the rectifier transformer, and (V_{Fd}) represents line to neutral voltage values in [rms] and oriented in a synchronous-frame rotating at (ω_F). The effects of commutation overlap are included within the term $(\frac{3B}{\pi}\omega_F L_{T_R} I_{Rdc})$ in equation (2.76) and (ω_F) is the frequency of the PCC.

2.4.3 HVdc link reactance and cable model

The HVdc link can be modelled using a T-equivalent of the dc transmission line [2]. Figure 2.14 shows equivalent circuit of the dc transmission system, where the mean voltages at dc terminals of the rectifier and inverters are denoted by (V_{Rdc}) and (V_{Idc}) respectively.

On the rectifier side, the resistance of the dc transmission line is represented by (R_R) while (L_R) is the series of the line inductance and the smoothing reactor. Likewise, on

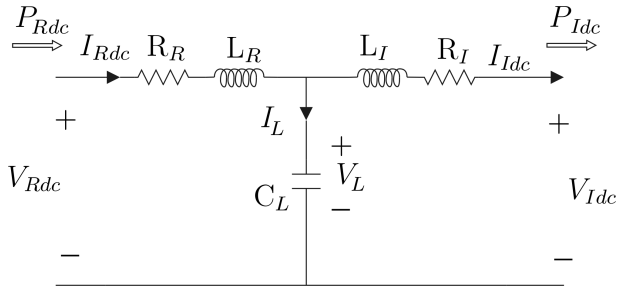

Figure 2.14: Model of the submarine cable

the inverter side, (R_I) represents the line resistance and (L_I) is the series of the line inductance and the smoothing reactor. The total capacitance of the dc transmission line is represented by (C_L). The dc currents are represented as (I_{Rdc}) and (I_{Idc}) in the rectifier and inverter side respectively, while (V_L) represents the non-measurable voltage of the line capacitance (C_L).

According to the dc line model shown in figure 2.14, the dynamics equations can be written as:

$$\frac{d}{dt}I_{Rdc} = -\frac{R_R}{L_R}I_{Rdc} + \frac{1}{L_R}V_{Rdc} - \frac{1}{L_R}V_L \tag{2.77}$$

$$\frac{d}{dt}I_{Idc} = -\frac{R_I}{L_I}I_{Rdc} - \frac{1}{L_I}V_{Idc} + \frac{1}{L_I}V_L \tag{2.78}$$

$$\frac{d}{dt}V_L = \frac{1}{C_L}I_{Rdc} - \frac{1}{C_L}I_{Idc} \tag{2.79}$$

2.4.4 Onshore LCC-HVdc inverter

Onshore rectifier is composed of two three-phase thyristor bridges as shown in figure 2.15. The bridges are in series on the dc-side and parallel on the ac-side. Two banks of transformers, one connected $Y - Y$ and the other $Y - \Delta$, are used to supply the bridges with a three-phase voltage displacement of 30° between them.

If the voltages from onshore ac-side are balanced and the HVdc inverter is conducting, then, the relationship between the HVdc inverter dc voltage (V_{Idc}) and the on shore

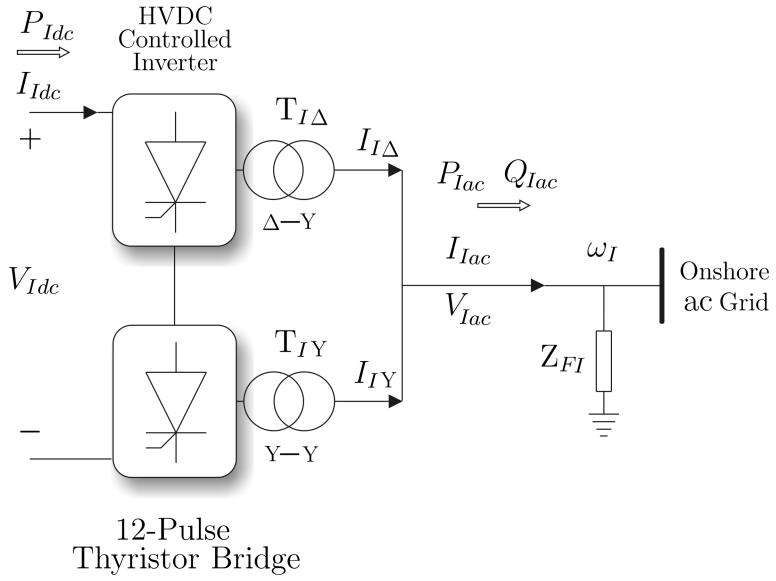

Figure 2.15: Onshore HVdc inverter

grid voltage (V_{Iacd}) can be defined as [2]:

$$V_{Idc} = \frac{3B\sqrt{6}}{\pi} N V_{Iacd} \cos(\gamma) - \frac{3B}{\pi} \omega_I L_{T_I} I_{Idc} \tag{2.80}$$

where, (γ) is the extinction angle, (B) is the number of bridges in series (for 12-pulse thyristor bridge $B = 2$), (N) is the turns ratio of the inverter transformer, (L_{T_I}) is the leakage inductance of the inverter transformer, and (V_{Iacd}) represents line to neutral voltage values in [rms] and oriented in a synchronous-frame rotating at (ω_I). The effects of overlap commutation are included within the term ($\frac{3B}{\pi}\omega_I L_{T_I} I_{Idc}$) in equation (3.1) and (ω_I) is the frequency of the onshore ac-grid.

Nonetheless, assuming an adequate control of the voltage (V_{Idc}) by means of a minimum-γ strategy [2], the onshore inverter can be replaced by a variable voltage dc source [40, 41]. Moreover, if the voltage drop caused by the overlap angle of the onshore inverter and the leakage inductance of the transformer (T_I) is not neglected, then, it is possible to lump them into the line resistance (R_I) shown in figure 2.14.

2.5 Summary

This chapter has described the mathematical model of an offshore wind farm and its transmission system. The model has been divided in three functional blocks, namely the wind turbine, the offshore wind farm and the HVdc link.

The first functional block describes the wind turbine according to the latest trends reported for multi-Megawatts offshore wind turbines, i.e. PMSG and fully-rated converter. This component has been analyzed as a single element considering its aerodynamic, mechanical and electrical characteristics. In this description only the basic aspects of the aerodynamics and the mechanical phenomena have been considered. Nonetheless, the electrical aspects are complex enough to describe more accurately the power dynamics and the grid integration of the wind turbine.

The second functional block describes the model of the offshore wind farm. In this block the entire set of wind turbines and the offshore ac-grid are represented according to three approaches. The first approach includes all the wind turbines connected to the point of common coupling. This representation is called the distributed model of the offshore wind farm which is not only the most complete representation but also the most complex. This model complexity can be reduced by lumping all the wind turbines in an aggregated model. On one hand, this model can represent the entire wind farm as a single model equivalent. But, on the other hand, some dynamics related to the interaction between wind turbines are lost. Finally, the intermediate solution to reduce the complexity of the distributed model is the clustered model representation. This representation is itself a distributed model wherein the wind farm is divided into sets of wind turbines, and these subsequently are lumped in aggregated models.

The third functional block describes the HVdc link. It has been modeled according to the CIGRE Benchmark model for HVdc studies. This model includes a modified version of the rectifier station and its ancillary services. Firstly, the thyristor-based rectifier has been replaced by a diode-based rectifier. Then, a transformer without tap changer has been contemplated for the HVdc rectifier. Lastly, the filter bank has been modified to produce the necessary reactive power to compensate the non-controlled

rectifier and the transformer.

Summing up, the above mentioned models have been described in this chapter. Additionally, according to these models it is possible to formulate more than one representation for the offshore wind farm. However, it is worth noticing that the criteria to use these models shall depend on the accuracy required and the phenomena to be studied.

CHAPTER 3

Overview of the Offshore Wind Farm Control Strategy

3.1 Introduction

The advantages of using a non-controlled HVdc rectifier have been mentioned before. However, the use of a diode-based rectifier places important restrictions in both, the control of the HVdc link and the control of the offshore ac-grid. These imposed restrictions not only have to be overcome by an adequate control strategy, but also all the different control tasks have to be carried out by the wind turbines.

The following control strategy proposes the coordinated control of the wind farm and the diode based HVdc link. The behavior of the overall system should be comparable to the standard fully controlled LCC-HVdc rectifiers, both in voltage control mode and current control mode. In addition, a similar response in presence to onshore and offshore fault events must be also provided.

The overall control strategy consists of two main tasks that will have to be carried out individually by each wind turbine. On one hand, the wind turbine control strategy has to be able to perform an optimal wind power tracking and an adequate fault protection. Hence, the first task will enclose the wind turbine torque and speed control, the converter dc-link voltage (E_{DC}) control, and the back-end converter control. On the other hand, the wind turbine grid integration strategy should provide

not only an adequate offshore ac-grid voltage and frequency control, but also an adequate limitation of the power delivered to the HVdc link. Therefore, the second task will include the control objectives related with the front-end converter control.
A detailed description of the aforementioned control strategies will be defined in the following sections.

3.2 Wind Turbine Control Tasks

The proposed wind turbine control tasks consist on two main control loops. Namely an speed control loop to prevent the wind turbine from over speeding and a generator side converter control to achieve back-to-back dc-link voltage (E_{DC}) regulation.

3.2.1 Speed control

A typical wind turbine speed control strategy involves basically the manipulation of pitch angle references and either the power references or torque references [18]. These strategies are widely used in commercial wind turbines. However, depending on the wind turbine characteristics, the strategies can involve complex algorithms to alleviate loads, avoid resonances and to perform an optimal energy capture.
The proposed control objective is to prevent the wind turbine over speeding when long grid faults occur. Therefore, the strategy will be based on a mere standard pitch control, and do not attempt to achieve the loads alleviation objectives defined in more complex strategies [18, 42, 43].
The proposed strategy will be programmed to operate according to figures 3.1 to 3.3 , where, the optimal curves in steady state of the wind turbine define the desired behavior of the generator speed, the blade pitch angle and the delivered electrical power as function of the mean wind speed. The optimal curves are obtained with the maximum value of the power coefficient $Cp(\lambda, \beta)$ regarding to the wind speed operational range[14].
Moreover, figures 3.1 to 3.3 also show four operation zones namely non-connected zone, low wind speed zone, transition zone and high wind speed zone. The zones

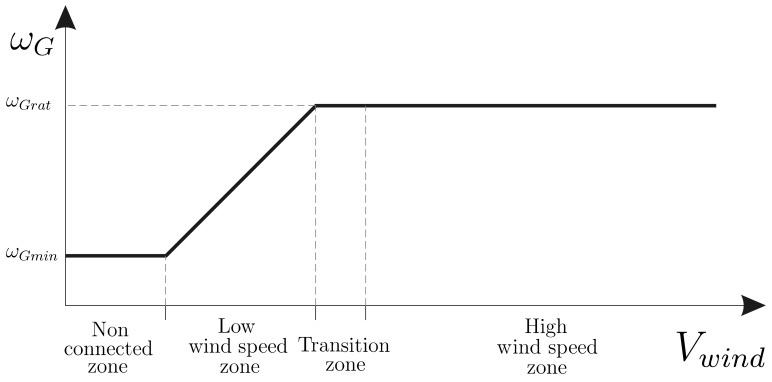

Figure 3.1: Generator speed steady state operation

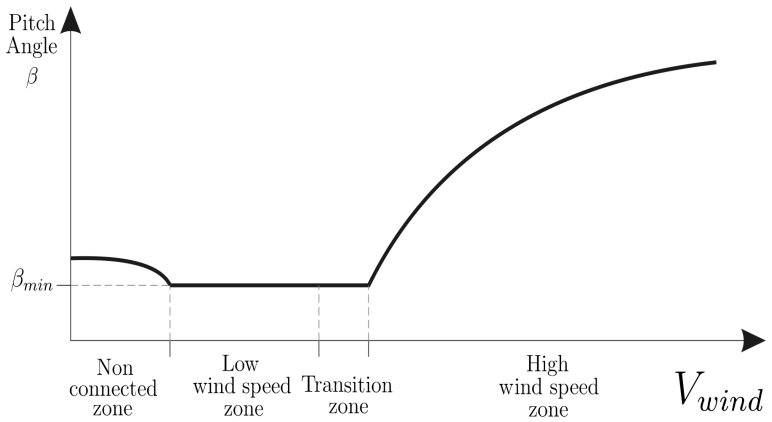

Figure 3.2: Blade pitch angle steady state operation

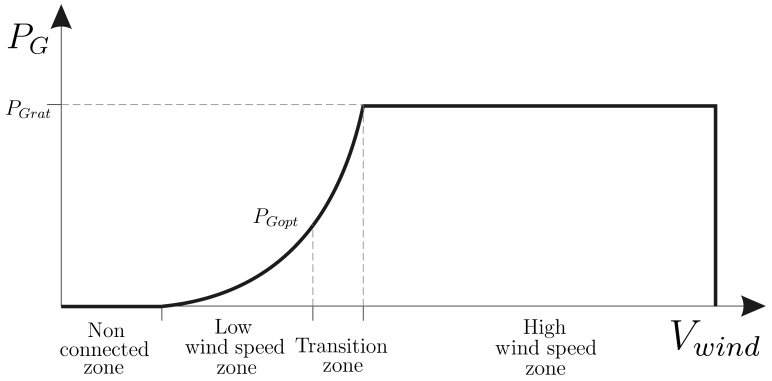

Figure 3.3: Generator power steady state operation

are defined depending on the values of the wind speed, the generator speed and the delivered power.

The control strategy for non-connected zone is defined by an open loop control of the generator speed, where the blade pitch angle is commanded by the optimal pitch angle curve defined in figure 3.2. In this operational zone the delivered power is zero and the main objective is to set the generator speed to a constant value ($\omega_G = \omega_{G\,\min}$).

The control strategy for low wind speed zone sets the blade pitch angle to a minimal angle reference ($\beta_{\min}$) in order to capture maximum energy. The generator speed will be defined according the optimal nonlinear relationship with respect to the demanded electric power; i.e. ($P_{Gopt} = K_{opt}\ \omega_G^3$) [44]. This zone is also called quadratic zone (quadratic regarding to the torque) and the value of (K_{opt}) can be calculated with the maximum value of the power coefficient $Cp(\lambda, \beta)$. The nonlinear relationship with reference to electric power will be used later to define the current limits of the front-end converter connected to the grid side.

The control strategy for the transition zone is defined by an open loop control of the generator speed, where the demanded power will be defined according the nonlinear relationship respecting to the demanded electric power; i.e. ($P_{Gopt} = K_{opt}\ \omega_G^3$) [44]. For this zone the demanded electrical power is a suboptimal solution with regard to the delivered power [18].

However by managing the delivered power (and indirectly the generator torque) the

generator speed must be set to rated values ($\omega_G = \omega_{G\text{rat}}$) as can be seen in figure 3.1. The blade pitch angle should remain following the curve defined in figure 3.2, i.e. $\beta = \beta_{\min}$.

The control strategy for the high wind speed zone is defined by a closed loop control of the generator speed. The main objective of this zone is to deliver variable pitch references in order to set the generator speed to rated value, i.e. ($\omega_G = \omega_{G\text{rat}}$). As a consequence the wind turbine will keep both rated speed and rated power under wind speed fluctuations at high wind.

Figure 3.4 shows the block diagram of the proposed wind turbine speed control.

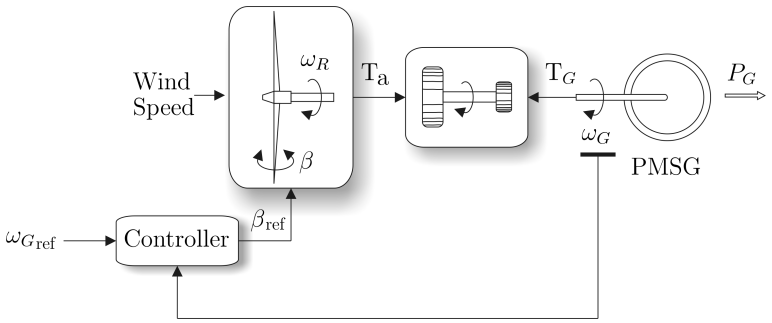

Figure 3.4: Proposed strategy for wind turbine speed control

3.2.2 Back-to-back dc-link voltage control

Usually, the front-end active current (I_{Wd}) is used to control the dc-link voltage (E_{DC}), whereas the synchronous generator torque current (I_{sq}) is used to achieve an optimum power tracking. However, the dc-link voltage (E_{DC}) can be set to a reference value by means of an adequate control of the synchronous generator torque current (I_{sq}) [45]. This approach allows the control of (E_{DC}) without relying on the offshore ac-grid. Therefore, in presence of an offshore ac-grid blackout, this wind turbine capability could be used in order to contribute to the black-start.

Ideally, the entire power produced by the generator has to be delivered to the grid in order to maintain a balanced power flow through the power converter. Additionally, the adequate control of the (E_{DC}) voltage could guarantee that not only the power

generated is delivered to the grid, but also the torsional oscillations in the drive train are alleviated [9]. Nonetheless, in presence of grid faults it is inevitable that a dc-link power imbalance occurs. This imbalance can cause the overcharging of the dc-link capacitor (C_{DC}) and as a consequence an over voltage in (E_{DC}), i. e. an abrupt increasing of the voltage at the terminals of the capacitor (C_{DC}). In order to avoid the (E_{DC}) over voltages a dc-link chopper resistance is proposed. This strategy is also called dynamic braking and is used mainly for protection reasons. Similar approaches has been proposed before [9][46] to enhance the fault ride-through capability of PMSG based wind turbines in case of severe grid faults.

Figure 3.5 shows the diagram of the proposed back-to-back dc-link voltage control strategy.

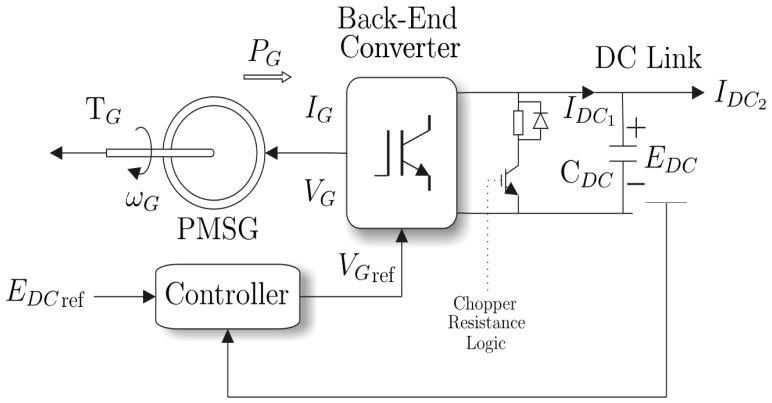

Figure 3.5: Proposed strategy for back-to-back dc-link voltage control

3.3 Wind Turbine Grid Integration Tasks

As previously mentioned, the use of wind turbines with fully rated converters [47][21] offers the possibility of tight control of the offshore ac-grid voltage and frequency. Several alternatives for the control of inverter-based islanded grids have been proposed for distributed generation and microgrids [48, 49, 50, 51, 52, 53], generally using standard (P/f) and (Q/V) droop control.

The present strategy is based on the assumption that the characteristics of the offshore ac-grid are known to a great extent. Therefore, from the analysis of the network dynamics, a (P/V) and (Q/f) control strategy is proposed. A similar technique has been used before for power control in microgrids [52], where, multiple voltage source converters have been considered to operate in parallel. The electrical parameters of this converter fed microgrid are controlled by using droops of voltage-power and a frequency-reactive power boost. The strategies explained in [52] lead to a relatively straight forward decoupling of (P) and (Q) dynamics during the grid frequency and voltage regulation. However, an offshore ac-grid connected to a HVdc system is quite different than the microgrid considered in [52]. Hence, the analysis must be performed with different considerations.

Due to the nature of the proposed offshore ac-grid, the control strategy has to contemplate different modes of operation in order to perform the grid forming capability when it has been required. The modes of operation are:

- Islanded operation - Mode A (rectifier voltage control and inverter voltage control).
- Connected operation - Mode B (rectifier voltage control and inverter voltage control).
- Connected operation - Mode C (rectifier current control and inverter voltage control).

Figure 3.6 shows how the front-end converter could be used to control the offshore ac-grid voltage and frequency. The control strategy is applied to the i^{th}-wind turbine belonging to the wind farm.

3.3.1 Modes of operation

When the HVdc diode rectifier is conducting the relationship between the HVdc rectifier dc voltage (V_{Rdc}) and the grid voltage (V_{Fd}) was defined before by equation 2.76.

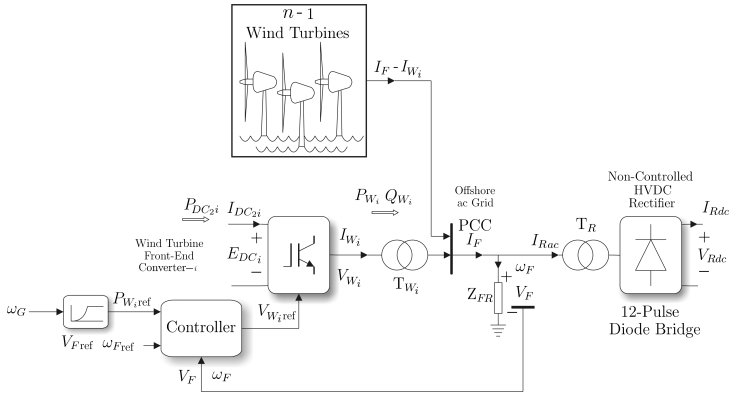

Figure 3.6: Proposed strategy for wind turbine grid integration

Usually, there will exist a saturation limit on the overall active current delivered by the wind turbines, i.e. $I_{Fd} = \sum_{i=1}^{n} I_{Wdi}$. Assuming no losses on the offshore ac-grid, i.e. $I_{Fd\,\max} = I_{Rd\,\max}$ in steady state; the relationship between $I_{Fd\,\max}$ and $I_{Rd\,\max}$ can be defined as:

$$I_{Rdc\,\max} = \frac{\sqrt{6}\pi V_{Rdc}}{12NV_{Rdc} - 6\sqrt{6}\omega_F L_{T_R} I_{Fd\,\max}} I_{Fd\,\max} \tag{3.1}$$

Equations 2.76 and 3.1 define the steady state operation characteristic of the HVdc rectifier (figures 3.7 to 3.9). Clearly, this characteristic can be modified by changing the set point of the off-shore ac-grid voltage (V_{Fd}) and/or by modifying the wind farm overall active current limit ($I_{Fd\,\max}$).

The intersection between the HVdc diode rectifier curve and the HVdc inverter curve will define the HVdc link steady state operating point. Figures 3.7 to 3.9 show the three possible operating points with regard to the offshore ac-grid voltage value (V_{Fd}). These figures depict the HVdc rectifier steady state characteristic, as per equations 2.76 and 3.1.

It is assumed that the inverter would be operating in voltage or in minimum-γ control [2]. The inverter steady state characteristic is represented by an almost horizontal line. Clearly, the slope of this line would be slightly positive for inverter voltage control and slightly negative for minimum-γ control.

Islanded operation - Mode A ($I_{Rdc} = 0$ and $V_{Rdc_0} < V_{Rdc}$)

When the wind farm is operating in islanding mode, the offshore ac-grid dynamics is well known and dominated mainly by the HVdc rectifier capacitor and filter bank (Z_{FR}). However, as the rectifier is not conducting ($I_{Rdc} = 0$), then the rectifier voltage (V_{Rdc}) will be equal to the HVdc inverter voltage (V_{Idc}). Therefore, the expression defined before in equation 2.76 is no longer valid to represent the dynamics of (V_{Rdc}). The solution to overcome the conducting condition is strongly related to the control of the offshore ac-grid voltage (V_{Fd}). By using equation 2.76 with $I_{Rdc} = 0$, it is possible to define the relation $V_{Rdc_0} = \frac{3B\sqrt{6}}{\pi} N V_{Fd}$, where (V_{Rdc_0}) is defined by the offshore ac-grid voltage (V_{Fd}), and moreover its value establishes the non-conducting condition of the HVdc rectifier as $V_{Rdc_0} < V_{Rdc}$ (operation mode A). Hence, if the value of (V_{Rdc_0}) does not increase sufficiently to overcome the value of (V_{Rdc}) imposed by the inverter, then the wind farm will remain operating in islanding mode. Figure 3.7 shows the operational curves of this mode of operation.
Based on the technique proposed by [52], a (P/V) control strategy will be used to deliver the necessary active power to set the offshore ac-grid voltage; while, the (Q/f) control strategy will be used to deliver the necessary reactive power to set the offshore ac- frequency. The strategy will be carried out by the front-end converter of the wind turbine.

Connected operation - Mode B ($0 < I_{Rdc} < I_{Rdc\,\max}$ and $V_{Rdc_0} > V_{Rdc}$)

In this operational mode, the offshore ac-grid voltage is large enough to overcome the conduction condition defined before. Once the HVdc link is conducting, the wind farm will be operating in connected mode and the HVdc diode rectifier will act as a voltage clamp on the offshore ac-grid voltage. However, the active current delivered by the front-end converters has not reached its limit ($I_{Fd\,\max}$) yet. This fact implies that the wind turbines can still keep control of the offshore ac-grid voltage. Therefore, the proposed strategy for this operational mode will consist of the smooth transition between the voltage defined in the islanded operation mode and the voltage imposed by the HVdc diode rectifier.

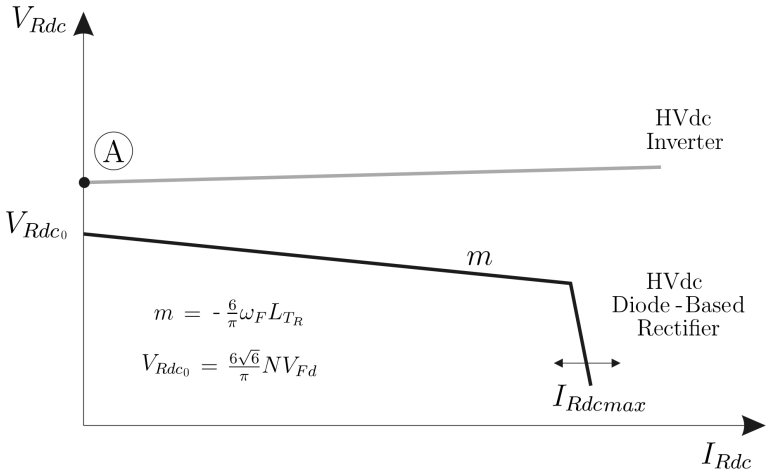

Figure 3.7: HVdc link steady state operation characteristic (operation mode A)

Figure 3.8 shows the operation of the HVdc link with an intermediate value of (V_{Fd}), $I_{Rdc} < I_{Rdc\,\max}$, and both rectifier and inverter in voltage mode of operation (operation mode B).

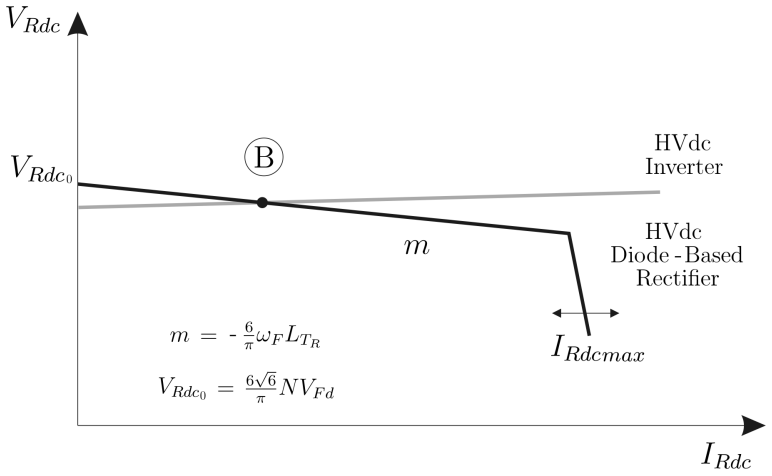

Figure 3.8: HVdc link steady state operation characteristic (operation mode B)

Connected operation - Mode C ($I_{Rdc} = I_{Rdc\,\max}$ and $V_{Rdc_0} > V_{Rdc}$)

If the offshore ac-grid voltage reference (V_{Fd}) is increased beyond a certain point (figure 3.9), then the current limit of each wind turbine is saturated (operation mode C). This saturation limit is defined according to the rated inverter current and the maximum power that the wind turbine can deliver with the available wind speed. At this point, the HVdc link current will be determined by equation (3.1). Additionally, the steady state offshore ac-grid voltage magnitude will be determined by the inverter side dc voltage (V_{Idc}) and the HVdc link current (I_{Rdc}) as follows:

$$V_{Fd} = \frac{\sqrt{6}}{36}\frac{\pi}{N}\left(V_{Idc} + \left(R_R + R_I + \frac{6}{\pi}L_{T_R}\omega_F\right)I_{Rdc}\right) \tag{3.2}$$

Therefore, the offshore ac-grid voltage will be indirectly controlled by the onshore inverter. As shown in figures 3.8 and 3.9, the transition from operation mode B to operation mode C can be achieved by either rising (V_{Fd}) or by decreasing the front-end converter active current limits ($I_{W\,d_i\,\max}$), which in turn, determines the value of ($I_{Rdc\,\max}$). At this stage, the active current limit on each front-end converter ($I_{W\,d_i\,\max}$) can be set to follow the optimal power tracking according to the wind turbine characteristic [44].

The HVdc rectifier current control mode strategy will be based on setting the individual wind turbine currents according to the optimal power tracking. However, in presence of faults the proposed currents are not longer valid. Hence, a Voltage Dependant Current Order Limit (VDCOL) similar to the employed in a LCC-HVdc link [2] have to be carried out.

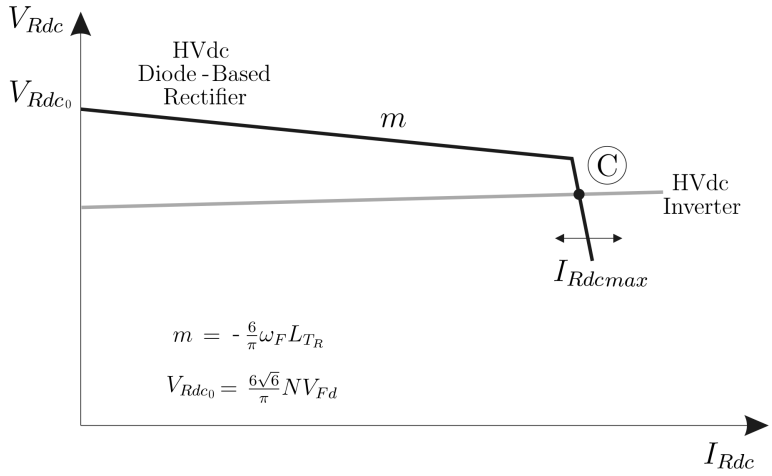

Figure 3.9: HVdc link steady state operation characteristic (operation mode C)

3.4 Summary

This chapter has described the proposed wind turbine control strategies. These strategies have been designed to contribute to the grid support in offshore wind farms with HVdc Links and diode-based rectifiers. According to the control objectives, the strategies have been divided in strategies to control the wind turbine and strategies to perform the wind turbine grid integration and grid support.

The strategies to control the wind turbine are based in control loops to set mainly the rotor speed and the dc-link voltage at the power converter. The First strategy is addressed to protect the wind turbine against over speeding when large grid faults occur. Whereas, the second strategy is aimed to avoid overvoltage in the dc-link of the power converter during grid disconnections or voltage dips.

Moreover, the strategies for grid integration and grid support are based on the knowledge of the offshore wind farm characteristics. These characteristics show that the power dynamics imposed by the diode-based HVdc link is mainly dominated by the value of the current passing through the rectifier. As a consequence, three operational modes have been defined according to the conduction constraints imposed by the diode rectifier. The first mode is the islanded operation; in this mode the rectifier is not conducting and the offshore ac-grid dynamics is dominated mainly by the

capacitor and filter bank of the HVdc rectifier. However, in islanded operation the offshore ac-voltage is set by the wind turbines and the conduction condition can be overcome.

Consequently, there is a smooth transition called connected operation mode (B). In this mode the offshore ac-voltage is defined according to the wind turbines and the HVdc diode rectifier. The last operation mode or connected operation mode (C) occurs when the current passing through the rectifier achieves its maximum value. In this mode the HVdc diode rectifier acts as a clamp and the offshore ac-voltage is imposed by the HVdc inverter.

In the following chapters the above mentioned strategies will be implemented. Additionally, the aggregated and the clustered model of the offshore wind farm will be employed. Finally, considering islanded and connected modes of operation and transient conditions, the strategies will be validated.

CHAPTER 4

Control of the Aggregated Offshore Wind Farm

4.1 Introduction

The control of an offshore wind farm is carried out in this chapter. According to section 2.3.1, all the wind turbines have been aggregated into a single equivalent machine. This aggregation has been carried out in order to reduce the complexity of the overall model. Consequently, the steady state and the transient functioning of the whole wind farm can be evaluated more easily.

Figure 4.1 shows the proposed aggregated model of the offshore wind farm with n-wind turbines. Besides, their dynamics have been explained in section 2.3.1. In this model, all the components included into the generator side of the converter retains the same aerodynamics, mechanical and electrical parameters than in individual wind turbine model. But, the components included into the grid side of the converter have been scaled to produce the equivalent power of the entire wind farm.

The power transmission of the entire offshore wind farm is carried out by HVdc link. This transmission system is based on the diode-based HVdc link explained in section 2.4. But, the shortcoming of using a diode-based rectifier is the fact that it can not contribute to control the offshore ac-grid. Therefore, this chapter introduces a new alternative to set the grid voltage and frequency at the point of common coupling

(PCC). This alternative is based on using the wind turbine back-end converter to set the converter dc-link voltage, whereas the front-end converter performs the grid integration.

In the following sections several control loops will be developed and evaluated. As explained in chapter 3, the overall strategy will be divided into rotor side control strategy and grid side control strategy. Finally, this chapter also includes the stability analysis of the proposed control loops and its validation by means of PSCAD^{TM} simulations.

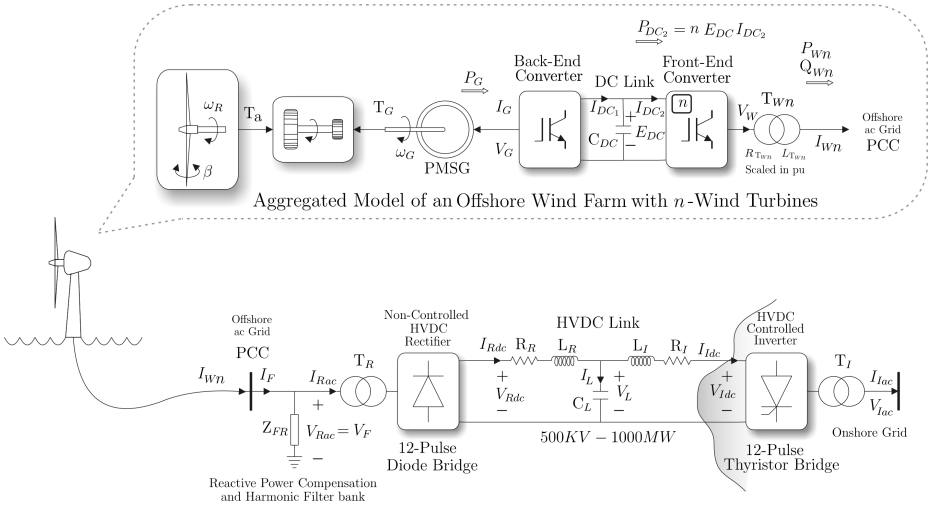

Figure 4.1: Aggregated model of an offshore wind farm with n-wind turbines

4.2 Wind Turbine Control

As mentioned in section 3.2, the proposed wind turbine control strategy will consist of two tasks. The first task will be the speed control to prevent the wind turbine from overspeeding, and the second task will correspond to the (E_{DC}) voltage regulation of the back-to-back dc-link. In the following sections, the aforementioned control strategies will be carried out considering the aggregated model equivalent of an offshore wind farm.

4.2.1 Wind turbine speed control

Modern techniques to achieve the speed control of the multi-megawatt wind turbines are based on multi-objective approaches. These techniques try to regulate not only the wind turbine speed, but also other variables such as power, noise or loads. However, the proposed approach will be only focused on the control of the wind turbine speed. Hence it will be based on a mere standard pitch control [9], according to the closed loop strategy defined before in section 3.2.1.

Wind turbine speed will be controlled via variations of the pitch angle. However, according to figure 3.2, the blade pitch angle (β) must be held almost constant at ($\beta_{\min}$) for power below (P_{Grat}), while, the generator speed is set according to the optimal non linear relationship ($P_{Gopt} = K_{opt}\ \omega_G^3$) [44]. For this reason, only high wind speed zone will be considered, and the blade pitching will be used to both, regulate the maximum extracted wind power, and prevent overspeeding when the wind turbine cannot deliver all the available wind power to the grid (i.e. when the HVdc link is disconnected or during faults).

Considering the model of the mechanical drive train described in (18.6) and (18.7), and only for control purposes, it is possible to simplify the analysis assuming a rigid shaft, i.e. $\theta_R = \theta_G$, thus, $\omega_R = \omega_G$. The simplified model of the drive-train will be equivalent to one-mass model and can be written as follows:

$$T_a + T_G - (D_R + D_G)\,\frac{d\theta_R}{dt} = (J_R + J_G)\,\frac{d^2\theta_R}{dt^2} \tag{4.1}$$

The mechanical parameters considered for the drive train model are shown in table 4.1.

Defining a decoupling input $U_R = T_a + T_G$, a moment of inertia $J = J_R + J_G$ and damping constant as $D = D_R + D_G$, the equation 4.1 could be defined as:

$$J\frac{d\omega_R}{dt} + D\omega_R = U_R \tag{4.2}$$

It is worth noting that (T_G) will be set indirectly by the (E_{DC}) control strategy covered in the following section, hence, it cannot be used for speed control. Additionally, as the (E_{DC}) control loop will be sufficiently faster than the wind turbine dynamics,

Table 4.1: Mechanical parameters

Parameter	Units	Value
Wind turbine rotor inertia (J_R)	(kg.m^2)	10x10^6
Generator inertia (J_G)	(kg.m^2)	100x10^3
Wind turbine rotor damping (D_R)	(N.m/rad/s)	20
Generator damping (D_G)	(N.m/rad/s)	100
Shaft stiffness (k)	(N.m/rad)	1.6x10^9

Parameters exptrapolated from [19]

it is possible to consider (T_G) as a constant perturbation. Hence, the decoupling input (U_R) could be defined in frequency domain as $U_R(s) = T_a(s)$.

According to equation 4.2 , the wind turbine speed (ω_R) can be controlled to follow desired speed references with a simple PI Controller. The proposed (ω_R) control loop is depicted in figure 4.2, where the equation 4.2 is used to obtain the following transfer function:

$$\omega_R(s) = \frac{1}{(Js + D)} T_a(s) \tag{4.3}$$

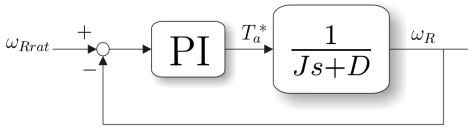

Figure 4.2: Wind turbine angular speed (ω_R) control loop

The parameters of the resulting controller for the first order systems have been calculated to accomplish with a settling time less than 5s ($ST < 5\,\mathrm{s}$) and a damping ratio greater than 0.707 ($DR > 0.707$). The values of the necessary proportional gain (K_P) and the integral time constant (T_I) are shown in table 4.2.

The success of the (ω_R) control loop will depend on the ability to set the proposed aerodynamic torque (T_a), according to the PI output references (T_a^*).

The aforementioned equations 2.1 to 2.5, define (T_a) as the non-linear relationship

Table 4.2: Wind turbine speed (ω_R) controller parameters

Parameter	Value
K_P	16.5139x10^6
T_I	78.7216x$10^{-9}s$

between the wind speed (V_{wind}), the wind turbine angular speed (ω_R), and the blade pitch angle (β), i.e. $T_a = f(V_{wind}, \omega_R, \beta)$. Therefore, in order to obtain an angular speed at rated values, the value of (T_a) must be set according to the PI controller output (T_a^*). As a consecuense, the blade pitch angle (β) should vary according to wind speed fluctuations (V_{wind}) to prevent the wind turbine from overspeeding.

Gain scheduling control is a typical approach to carry out the control of non-linear systems whose behavior can be adequately described using a selection of local linearized models. Hence, in broad terms, the design procedure of a gain scheduled controller can be used to define the adequate relationship between the demanded aerodynamic torque (T_a^*) and its corresponding blade pitch angle reference (β^*).

Firstly, the dynamics of (T_a) will be defined assuming wind turbine operation within high wind speeds zone; hence, the wind turbine speed should be set to rated value, i.e. $\omega_R = \omega_{Rrat}$. Then, using a subset of wind speed values, a family of non-linear equations for the aerodynamic torque will be defined. Each equation will only depend on the blade pitch angle, and they will be associated to their corresponding wind speed value.

Assuming rated speed operation, figure 4.3 shows the family of non-linear expression for (T_a) with regards to different wind speed values (for this case the values go from 9 m/ s to 25 m/ s). Note that rated aerodynamic torque value (T_{arat}) has been depicted by a horizontal line, which defines the set of the necessary blade pitch angle ($\beta_o = [\beta_1, \ldots, \beta_k]$) in order to maintain $T_a = T_{arat}$.

Next, by using equations 2.1 to 2.5, a family of linearized expression of (T_a) will be defined. Note that the set of linearization points (po) will be defined according to the set of wind speed values (V_{wind}), and their corresponding set of blade pitch angle values (β_o), when $T_a = T_{arat}$. The linearized expression of (T_a) can be defined as

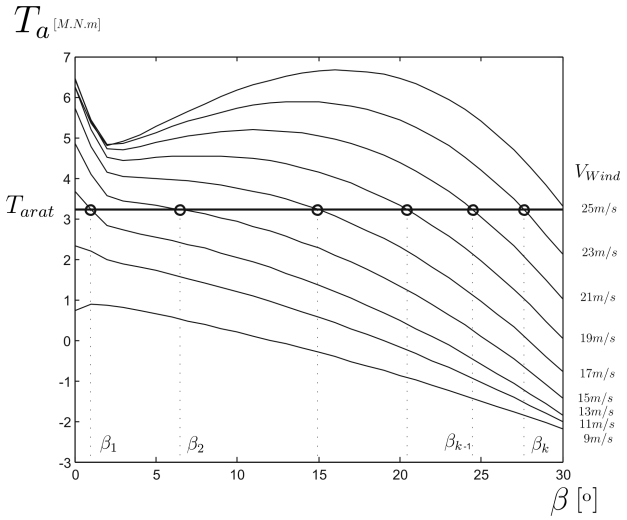

Figure 4.3: Non-linear expression for (T_a) Vs. blade pitch angle (β) for differents wind speed values

follows:

$$\Delta T_a = \frac{\partial}{\partial \beta}\left(T_a\right)\Big|_{po} \Delta\beta \tag{4.4}$$

where $\Delta T_a = T_a - T_{arat}$ and $\Delta\beta = \beta - \beta_o$. In addition, the expression $\frac{\partial}{\partial \beta}\left(T_a\right)\Big|_{po}$ defines, a gain-scheduled parameter also called aerodynamic torque sensitivity in relation to blade pitch angle. Using the equation 4.4, and defining $K_\beta = \frac{\partial}{\partial \beta}\left(T_a\right)\Big|_{po}$ as a gain-scheduled parameter which varies according to the set of blade pitch angle values (β_o); then, it is possible to obtain the following transfer function:

$$T_{a(s)} = K_\beta \; \beta_{(s)} \tag{4.5}$$

Figure 4.4 shows the values of the expression $K_\beta = \frac{\partial}{\partial \beta}\left(T_a\right)\Big|_{po}$ with regards to the set of blade pitch angle values (β_o).

Last, in order to get a realistic response regarding to the pitch angle actuator, the limits on the pitch angle range (0 to 30 deg) and its maximum rate of change (14 deg/s) have to be included in the model. The implementation of the proposed (ω_R)

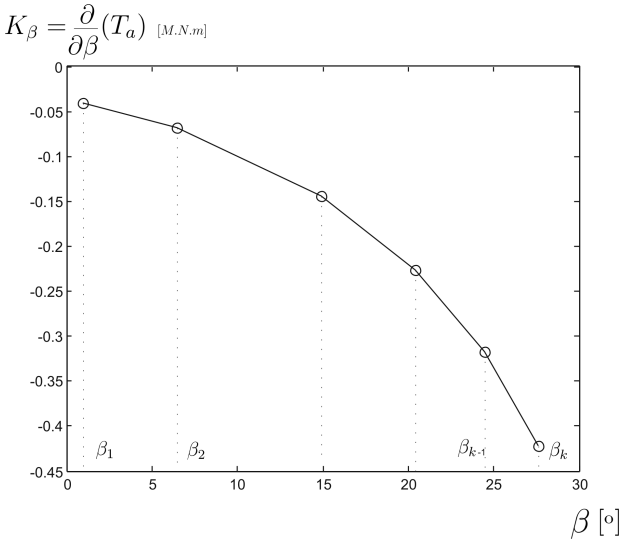

Figure 4.4: Gain-scheduling value (K_β) Vs. Set of blade pitch angle (β_o)

control loop is shown in figure 4.5. Notice that, the imposed limitations on the blade pitch angle reference (β^*) are particularly relevant during grid faults because they will determine the wind turbine maximum transient speed. However, as can be seen in figure 4.5, an anti-windup strategy has been implemented in order to avoid the unnecessary functioning of the integral part of the controller.

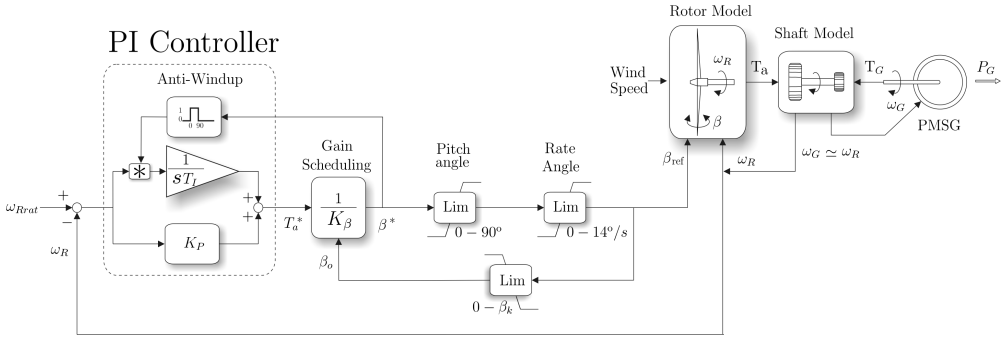

Figure 4.5: Proposed (ω_R) control loop

4.2.2 PMSG current control

The aggregated model of the wind farm was defined before by equations 2.24 to 2.35. Particularly, the equations 2.24 and 2.25 define the dynamics of the PMSG in a synchronous-frame rotating at (ω_G). However, in order to perform a dynamic decoupling, two new control inputs namely (U_d) and (U_q) are defined in the model as follows:

$$U_d = \frac{L_{Gq}}{L_{Gd}}\omega_G \; I_{Gq} + \frac{1}{L_{Gd}}V_{Gd} \tag{4.6}$$

$$U_q = -\frac{L_{Gd}}{L_{Gq}}\omega_G I_{Gd} + \frac{1}{L_{Gq}}V_{Gq} - \frac{1}{L_{Gq}}\omega_G \lambda_m \tag{4.7}$$

Therefore, the generator dynamics defined by equations 2.24 and 2.25, can be represented as the following expressions:

$$\frac{dI_{Gd}}{dt} = -\frac{R_G}{L_{Gd}}I_{Gd} + U_d \tag{4.8}$$

$$\frac{dI_{Gq}}{dt} = -\frac{R_G}{L_{Gq}}I_{Gq} + U_q \tag{4.9}$$

By applying the Laplace transform with (U_d) and (U_q) as system inputs and (I_{Gd}) and (I_{Gq}) as system outputs, the decoupled transfer functions of the generator dynamics can be defined as follows:

$$I_{Gd}(s) = \frac{1}{\left(s + \frac{R_G}{L_{Gd}}\right)}U_d(s) \tag{4.10}$$

$$I_{Gq}(s) = \frac{1}{\left(s + \frac{R_G}{L_{Gq}}\right)}U_q(s) \tag{4.11}$$

As a result, the expression defined in equations 4.10 and 4.11 describes two independent first order systems. Moreover, they can be used to control the (I_{Gd}) and (I_{Gq}) currents by means of two independent PI control loops. Figure 4.6 shows the proposed PI control loops.

The electrical characteristics of the PMSG are shown in table 4.3. The resulting parameters of the PI controllers are defined in table 4.4. The values have been obtained

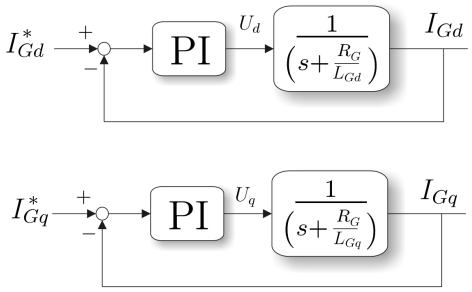

Figure 4.6: (I_{Gd}) and (I_{Gq}) current control loops

assuming as constraints a damping ration greater than 0.707 ($DR > 0.707$) and a settling time less than 5ms ($ST < 5\text{x}10^{-3}$ s).

Table 4.3: PMSG characteristics

Generator parameters	Units	Value
Rated Power	(MVA)	5
Base L-L voltage	(kV)	2
Rated frequency	(Hz)	20
Stator resistance (R_G)	(mΩ)	13.6
Stator leakage inductance (L_{Gd})	(mH)	5.09
Stator leakage inductance (L_{Fq})	(mH)	6.37
Rotor flux linkage (λ_m)	(Wb)	9.31
Poles of the generator (p)	Pairs	80

Parameters extrapolated from [19]

The implementation of the proposed current control loops of (I_{Gd}) and (I_{Gq}) is shown in figure 4.7. Notice that there exists a compensation expression defined for each loop. These terms are decoupling expressions that are used to determinate the required value of (V^*_{Gd}) and (V^*_{Gq}) while the currents (I_{Gd}) and (I_{Gq}) follow their references (I^*_{Gd}) and (I^*_{Gq}).

Table 4.4: PMSG current controller parameters

Parameter	Value
K_{Pd}	16.0771
T_{Id}	8.086x10^{-3}s
K_{Pq}	16.0771
T_{Iq}	8.086x10^{-3}s

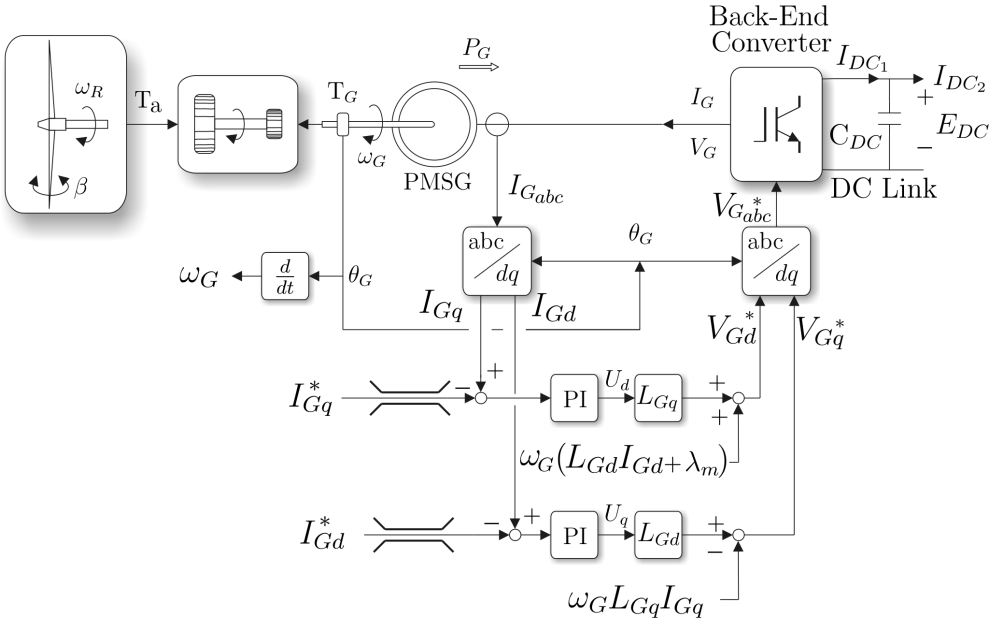

Figure 4.7: Generator current control loops implementation

4.2.3 Back to back converter dc-link voltage control

The relationship between the ac and the dc-sides of the wind turbine back-end converter was defined before by equations 2.26 and 2.27. Neglecting losses in power conversion, its is possible to define $P_G = P_{DC_1}$ according to figure 2.6 . Hence, the following equation can define the power balance between the ac-side and the dc-side of the back-end converter.

$$-3\left(V_{Gd}I_{Gd} + V_{Gq}I_{Gq}\right) = E_{DC}I_{DC1} \tag{4.12}$$

Assuming that the field current reference is set to zero i.e. $I^*_{Gd} = 0$, it is possible to define a proportional relationship between the generator torque (T_G) and (I_{Gq}), i.e. $T_G = 3p\ (\lambda_m I_{Gq})$. Moreover, the equation 4.12 can be written as follows:

$$-3V_{Gq}I_{Gq} = E_{DC}I_{DC1} \tag{4.13}$$

Substituting the dc-link capacitor dynamic $I_{DC1} = C_{DC}\frac{dE_{DC}}{dt} + I_{DC2}$ (defined before in equation 2.28), equation 4.13 can be defined as:

$$-3V_{Gq}I_{Gq} = C_{DC}E_{DC}\frac{dE_{DC}}{dt} + E_{DC}I_{DC2} \tag{4.14}$$

defining the expression $\frac{d\left(E^2_{DC}\right)}{dt} = 2E_{DC}\frac{dE_{DC}}{dt}$ as a mathematical artifice, and replacing in equation 4.14, the following expression can be defined:

$$\frac{d\left(E^2_{DC}\right)}{dt} = -\frac{1}{C_{DC}}\left(6V_{Gq}I_{Gq} + 2E_{DC}I_{DC2}\right) \tag{4.15}$$

In order to perform a dynamic decoupling the following expression is defined for $(U_{E_{DC}})$:

$$U_{E_{DC}} = -\frac{1}{C_{DC}}\left(6V_{Gq}I_{Gq} + 2E_{DC}I_{DC2}\right) \tag{4.16}$$

Therefore, the dynamics of (E^2_{DC}) is reduced to the following expression:

$$\frac{d\left(E^2_{DC}\right)}{dt} = U_{E_{DC}} \tag{4.17}$$

while its corresponding transfer function can be defined as follows:

$$E_{DC}^2(s) = \frac{1}{s} U_{E_{DC}}(s) \tag{4.18}$$

The plant to be controlled becomes a simple integrator and (E_{DC}^2) can be easily controlled by a PI control loop.

According to equation 4.16, it is possible to set (E_{DC}^2) at the desired values by using the PMSG current reference (I_{Gq}) as follows:

$$I_{Gq} = -\frac{C_{DC}}{6V_{Gq}} U_{E_{DC}} - \frac{E_{DC} I_{DC2}}{3V_{Gq}} = -\frac{C_{DC}}{6V_{Gq}} \left(U_{E_{DC}} + \frac{2E_{DC} I_{DC2}}{C_{DC}} \right) \tag{4.19}$$

where $(U_{E_{DC}})$ is the output of the PI controller used in the (E_{DC}^2) control loop. Additionally, the generator torque current reference (I_{Gq}) has been limited, so the generator never will operate in the motoring region. The proposed (E_{DC}^2) control loop is depicted in figure 4.8.

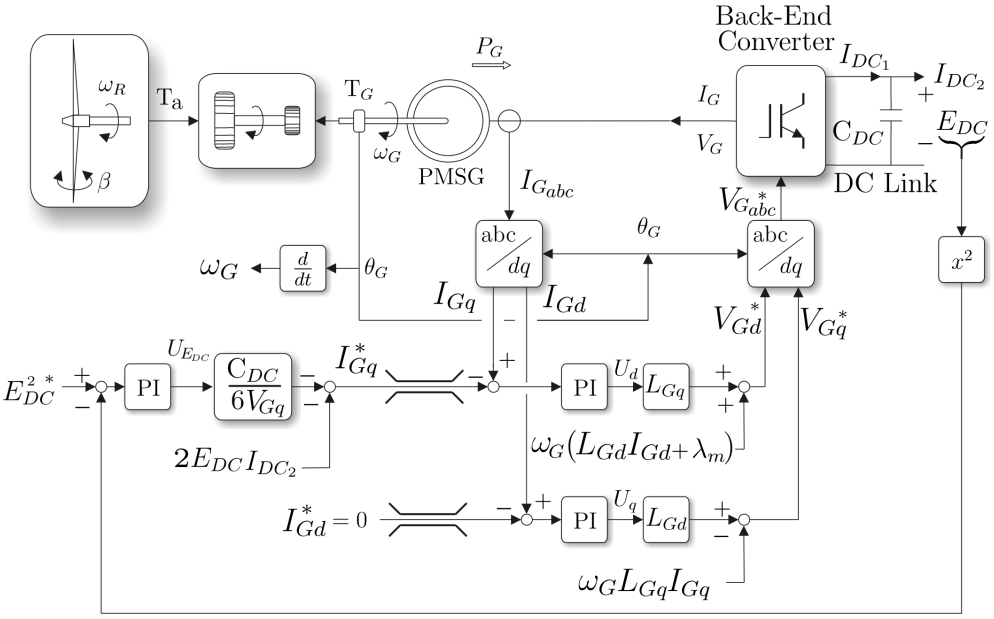

Figure 4.8: (E_{DC}^2) control loop

In order to perform the (E_{DC}^2) regulation, the rated value of E_{DC} correspond to 5.4 kV and the dc-link capacitance C_{DC} is set to store 115 kJ at rated voltage (i.e. 8000 μF

for 5 MVA of rated power). Moreover, the values of the (E_{DC}^2) PI controller have been obtained assuming as constraints a damping ration greater than 0.707 ($DR > 0.707$) and a settling time of 50ms ($ST = 50\text{x}10^{-3}$ s). The resulting parameters are shown in table 4.5

Table 4.5: Wind turbine dc-link voltage (E_{DC}) controller parameters

Parameter	Value
K_P	16.0771
T_I	$8.086\text{x}10^{-3}s$

4.2.4 Wind turbine control performance

Figure 4.9 shows the performance of the wind turbine speed (ω_R) and the back-to-back converter dc-link control against large load variations. Initially, the system is operated at rated wind and power. At ($t = 0.1s$), the load is suddenly disconnected. After disconnection, the PMSG torque current (I_{Gq}) is rapidly reduced and the wind turbine speed (ω_R) steadily increases. At this point, pitch control will act to bring the turbine back to rated speed. At ($t = 5.1s$), rated power operation is restored, leading to decreased turbine speed, as the pitch angle returns to zero. The maximum speed excursion clearly depends on the maximum pitch angle rate. Note the generator oscillations due to the direct-drive relatively low damping. It is worth stressing that the wind turbine dc-link voltage (E_{DC}) remains within acceptable limits in spite of the large load transients applied to the system. Therefore, in the following sections, a constant dc-link value (E_{DC}) is assumed.

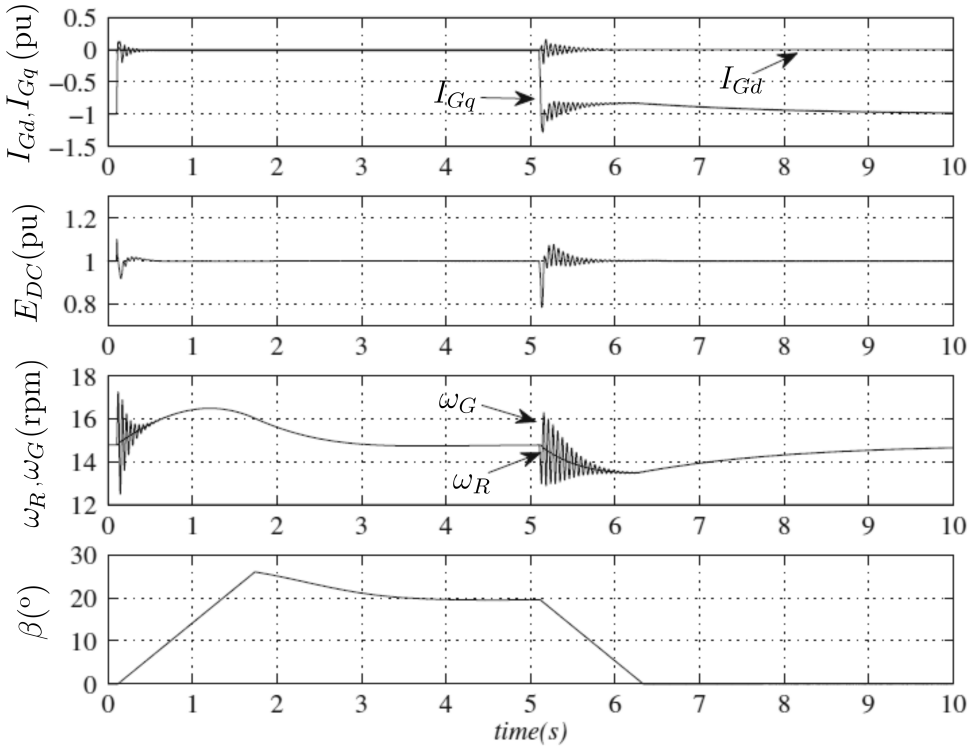

Figure 4.9: Wind turbine control performance for large loads variations

4.3 Wind Turbine Grid Integration

Assuming an adequate control of the dc-link voltage, the analysis of the offshore ac-grid will be carried out under the following simplifying assumptions:

- The dc-link voltage has been set to a constant value (E_{DC}).
- Offshore ac-line impedance can be negligible compared with wind turbine transformer leakage impedance.
- Transformer shunt branches are not considered.

Considering these assumptions, a simplified model of the aggregated wind farm is shown in figure 4.10.
Moreover, the ac-grid dynamics can be expressed by using equations 2.32 to 2.35 in a synchronous-frame oriented on (V_F), i.e. $V_{Fq} = 0$ and $\omega_{dq} = \omega_F$. Hence, the wind turbine grid integration dynamics can be defined as follows:

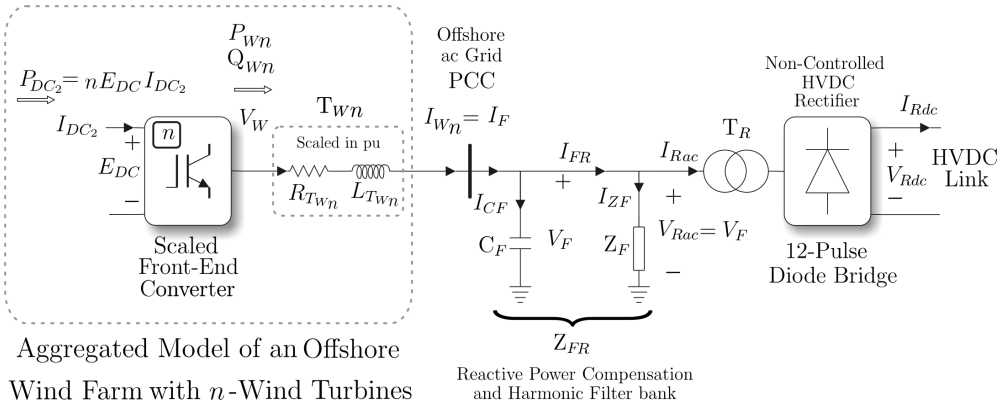

Figure 4.10: Simplified model of the aggregated offshore wind farm

$$\frac{d}{dt}I_{Fd} = -\frac{R_{T_{Wn}}}{L_{T_{Wn}}}I_{Fd} + \omega_F I_{Fq} + \frac{1}{L_{T_W}}V_{Wd} - \frac{1}{L_{T_W}}V_{Fd} \tag{4.20}$$

$$\frac{d}{dt}I_{Fq} = -\omega_F I_{Fd} - \frac{R_{T_{Wn}}}{L_{T_{Wn}}}I_{Fq} + \frac{1}{L_{T_W}}V_{Wq} \tag{4.21}$$

$$\frac{d}{dt}V_{Fd} = \frac{1}{C_F}I_{Fd} - \frac{1}{C_F}I_{FRd} \tag{4.22}$$

$$\omega_F V_{Fd} = \frac{1}{C_F}I_{Fq} - \frac{1}{C_F}I_{FRq} \tag{4.23}$$

Where all the variables are referred to the secondary side of the transformer (T_W) and (ω_F) is the instantaneous frequency of the voltage (V_F). In the following sections, a cascade control strategy will be defined to control the offshore voltage and frequency. The strategy will be performed by means of two phases. Firstly, the design of two inner control loops to set the currents (I_{Fd}) and (I_{Fq}) to a reference (I^*_{Fd}) and (I^*_{Fq}). Second, the design of the outer strategy to control the offshore ac-voltage (V_{Fd}) and the frequency (ω_F). The outer loop response should be slower than the inner control loops, and should provide them with their references (I^*_{Fd}) and (I^*_{Fq}) respectively.

4.3.1 Front-end converter current control

The dynamics of the front-end converter are defined by equations 4.20 and 4.21. However, in order to perform a dynamic decoupling, two new inputs namely (U_{Fd}) and (U_{Fq}) will be defined as follows:

$$U_{Fd} = L_{T_W}\omega_F I_{Fq} + V_{Wd} - V_{Fd} \tag{4.24}$$

$$U_{Fq} = -L_{T_W}\omega_F I_{Fd} + V_{Wq} \tag{4.25}$$

Therefore, the (I_{Fd}) and (I_{Fq}) dynamics becomes in the following expressions:

$$\frac{d}{dt}I_{Fd} = -\frac{R_{T_{Wn}}}{L_{T_{Wn}}}I_{Fd} + \frac{1}{L_{T_{Wn}}}U_{Fd} \tag{4.26}$$

$$\frac{d}{dt}I_{Fq} = -\frac{R_{T_{Wn}}}{L_{T_{Wn}}}I_{Fq} + \frac{1}{L_{T_{Wn}}}U_{Fq} \tag{4.27}$$

while, their corresponding transfer functions can be defined as follows:

$$I_{Fd}(s) = \frac{\frac{1}{L_{T_{Wn}}}}{\left(s + \frac{R_{T_{Wn}}}{L_{T_{Wn}}}\right)} U_{Fd}(s) \tag{4.28}$$

$$I_{Fq}(s) = \frac{\frac{1}{L_{T_{Wn}}}}{\left(s + \frac{R_{T_{Wn}}}{L_{T_{Wn}}}\right)} U_{Fq}(s) \tag{4.29}$$

As a result, the expressions defined in equations 4.28 and 4.29 describes two independent first order systems. Moreover, they can be used to control the (I_{Fd}) and (I_{Fq}) currents by means of two independent PI control loops. A similar procedure has been carried out for the PMSG control. Figure 4.11 shows the implementation of the proposed PI control loops.

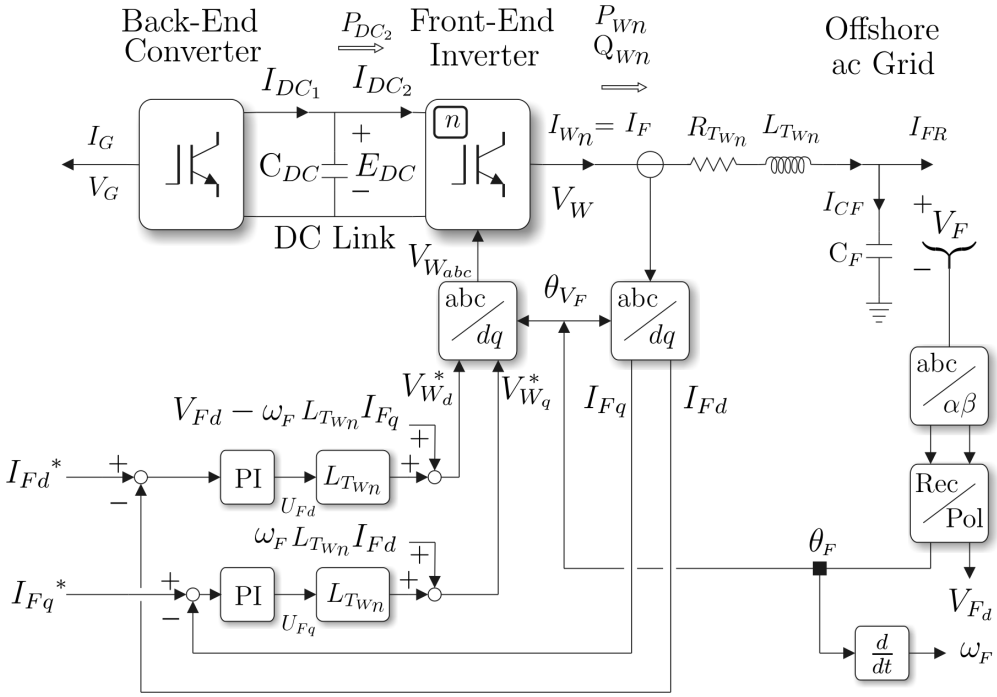

Figure 4.11: Implementation of the (I_{Fd}) and (I_{Fq}) current control loops

The characteristics of the transformer (T_W) are shown in table 4.6. Moreover, the resulting parameters of the PI controllers are defined in table 4.7. The values have

been obtained assuming as constraints a damping ration greater than 0.707 ($DR > 0.707$) and a settling time less than 2ms ($ST < 2\text{x}10^{-3}$ s).

Table 4.6: Transformer (T_W) characteristics

Transformer (T_W) parameters	Units	Value
Rated Power	(MVA)	1000
Rated frequency	(Hz)	50
Winding 1	(kV L-L rms)	20
Winding 2	(kV L-L rms)	13.6
$R_{T_{Wn}}$ (0.005 pu)	(mΩ)	595.125
$L_{T_{Wn}}$ (0.06 pu)	(mH)	22.7321

Table 4.7: Front-end (I_{Fd}) and (I_{Fq}) current controller parameters

Parameter	Value
K_{Pccd}	33.83
T_{Iccd}	$3.5476\text{x}10^{-5}s$
K_{Iccq}	33.83
T_{Iccq}	$3.5476\text{x}10^{-5}s$

Assuming sufficien fast dynamics in the aforementioned current control loops, the front-end converter currents will follow their references, i.e. $I_{Fd} = I^*_{Fd}$ and $I_{Fq} = I^*_{Fq}$. Therefore, the system dynamic defined in equations 4.22 and 4.23 will be reduced to:

$$\frac{d}{dt}V_{Fd} = \frac{1}{C_F}I^*_{Fd} - \frac{1}{C_F}I_{FRd} \tag{4.30}$$

$$\omega_F V_{Fd} = \frac{1}{C_F}I^*_{Fq} - \frac{1}{C_F}I_{FRq} \tag{4.31}$$

It is important to remark that these expressions are only valid if the current loops are significantly faster than the voltage dynamics defined in equations 4.30 and 4.31. Therefore, (I^*_{Fd}) can be used to control the offshore ac-grid voltage (V_{Fd}), whereas, (I^*_{Fq}) can be used as a control action for the offshore grid frequency (ω_F). Note this is

the opposite to the typical procedures performed in power systems, where the active power is used to control the frequency and the reactive power to control the voltage. However, in most general cases, the ac-grid characteristics are difficult to obtain, but, in the case of an offshore wind farm, the offshore ac-grid characteristics are largely determined by the transformer leakage reactance and the capacitance of the combined filter and capacitor bank. Hence, the offshore grid dynamics (dominated by the capacitor bank C_F) determine the coupling between the active and reactive power with regards to the offshore ac-voltage (V_{Fd}) and the frequency (ω_F).

4.3.2 Offshore ac-grid voltage control

The voltage controller can be calculated according to the dynamics described by equation 4.30. However, as mentioned before in section 3.3.1, the offshore wind farm will have to be analyzed during islanded operation and connected operation.

During islanding operation mode or operation mode A, the (V_{Fd}) value will be set by the wind farm. But in connected operation mode, the system can function according to two different modes of operation. On one hand, during connected operation mode B, the (V_{Fd}) value will be set partially by the onshore inverter. However, the wind farm will continue keeping certain control on the offshore ac-voltage (V_{Fd}). Hence, the same voltage control loop will keep being valid.

On the other hand, during connected operation mode C, the (V_{Fd}) value will be totally set by the onshore inverter, while the wind farm will be working in current control mode according to a desired value of ($I_{Rdc\,\max}$) e.g. maximum current to fulfill the optimal power tracking.

Operation in islanded mode

According to equation 4.30, it is possible to define $U_{V_{Fd}} = \frac{(I_{Fd} - I_{FRd})}{C_F}$ to perform a dynamic decoupling. Therefore, the dynamics of (V_{Fd}) are reduced to the following expression:

$$\frac{d}{dt} V_{Fd} = U_{V_{Fd}} \tag{4.32}$$

the corresponding transfer function can be defined as follows:

$$V_{Fd}(s) = \frac{1}{s} U_{V_{Fd}}(s) \tag{4.33}$$

The plant to be controlled becomes a simple integrator. Hence, (V_{Fd}) can be easily controlled by a PI control loop.

Figure 4.12 shows the offshore ac-voltage (V_{Fd}) control loop. Notice that while the value of (I_{Fd}) has not been saturated, the voltage PI controller will ensure that the offshore ac-voltage follows its reference by using the current control loop shown in figure 4.11. Besides, the required remote measurement of (I_{FRd}) can be avoided either by not using the feedforward term, with the corresponding performance degradation, or by estimating (I_{FRd}) from local variables.

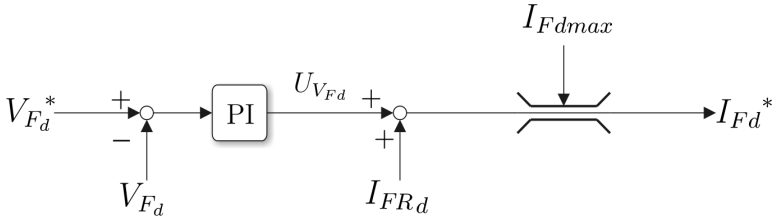

Figure 4.12: (V_{Fd}) Voltage control loop

Clearly, when the aggregated wind farm is operating in voltage control mode, it is not possible to limit the wind turbine speed by acting on the wind farm power set-point. Therefore, pitch control is used in order to prevent the wind turbine from overspeeding in both, when the wind farm is operated in voltage control mode, as well as when the wind speed is relatively high. The parameters of the PI controllers are defined in table 4.8. These values have been obtained assuming as constraints a damping ratio greater than 0.707 ($DR > 0.707$) and a settling time less than 50ms ($ST < 50\text{x}10^{-3}$ s).

Wind farm self-start capability

The aforementioned control in islanded mode presents an additional characteristic to improve the overall behavior of the offshore wind farm. If the wind farm is operated

Table 4.8: Parameters of the (V_{Fd}) voltage controller

Parameter	Value
K_{Pvc}	20.83333
T_{Ivc}	583.8x10^{-6}s

in islanded mode, the HVdc diode rectifier would not able to start the offshore ac-grid by itself; even if the HVdc link is energized. Therefore, the wind farm should perform this operation by itself taking into account two aspects. Firstly, the HVdc link must be energized. Secondly, the aggregated wind farm back-end converter should be controlled in accordance with the strategy presented in section 3.2.2.

The HVdc link should be initially energized by means of some sort of ancillary equipment, to ensure initial conduction of the inverter station. Moreover, once the wind resource is enough to rotate the wind turbine and compensate the system losses, the strategy proposed in section 3.2.2 can set the dc-link voltage (E_{DC}) to his rated value. Afterwards, the front-end inverter could start its operation at reduced voltage (V_{Fd}) (operation mode A) as a previous stage to operate in connected mode. Finally, the connected mode (operation mode B and C) can be reached when the voltage (V_{Fd}) is slowly increased until it overcomes the conduction condition imposed by the diode rectifier.

Definitely, at this point it is considered that the aggregated wind farm has grid forming capability. Additionally, the system complies with the self-start requirement which is frequently cited as an important drawback of the LCC-HVdc technology. This additional characteristic will be validated on the last section of this chapter by means of PSCAD^{TM} simulations.

Operation in connected mode

Section 3.3.1 has defined the operational mode B and the operational mode C to describe the conducting condition of the HVdc diode rectifier. The conduction condition is defined by equation 2.76 [2] and represents the relationship between the ac and dc voltages on both sides of the rectifier. Figures 3.8 an 3.9 shows the operational curves

of connected operation mode B and connected operation mode C respectively.
As mentioned before, during operation mode B, the (V_{Fd}) control loop defined for islanded operation will continue being valid. Nonetheless, the main objective of this operation mode corresponds to the smooth transition between islanded and connected mode. In operation mode C, the offshore ac-grid voltage (V_{Fd}) will be set indirectly by the onshore inverter according equation 3.2.
If the onshore inverter is operating in current control mode, the voltage control loop in figure 4.12 will ensure that (V_{Fd}) follows its reference and, hence, the rectifier side HVdc voltage (V_{Rdc}) will be determined by equation 2.76. This mode of operation is similar to the one already reported in [4], and therefore it shares two important drawbacks. Firstly, the rectifier must be operated only in voltage control mode. Hence. the current passing through the diode-based rectifier depends on the conduction condition imposed by 2.76. Secondly, the current demand must be set by the onshore inverter, and as a consequence, the offshore ac-grid will be indirectly controlled by the onshore inverter. Moreover, the inverter will be operating with large extinction angles, leading to large reactive power requirements and decreased efficiency.
Therefore, it is preferred that the onshore station is operated in minimum gamma or in voltage control mode. When the onshore inverter is operating in minimum-γ (Voltage control mode), the voltages (V_{Rdc}) and (V_{Idc}) will be approximately the same (neglecting HVdc line voltage drop). Therefore, according to equation 2.76, the diode rectifier will act as a voltage clamp on (V_{Fd}). At this point, the voltage control loop shown in figure 4.12 will be saturated and both, the offshore wind farm and the diode rectifier, will be operating indirectly in current control mode. Figure 3.9 shows the saturation limit ($I_{Rdc\,\max}$) imposed when the value of (V_{Fd}) is kept to rated values.

4.3.3 Offshore ac-grid frequency control

Offshore ac-grid frequency control will be performed according to the dynamics described by equation 4.31. As can be seen, the equation represents a constraint imposed on (ω_F) according to the (V_{Fd}) and (I_{FRq}) values. Figure 4.13 shows the basic frequency control algorithm, based directly on equation 4.31 with some filtering on (V_{Fd}). Nonetheless, the open loop control based on equation 4.31 is extremely sensitive to

C_F estimation errors and moreover, it does require the use of a remote measurement of (I_{FRq}).

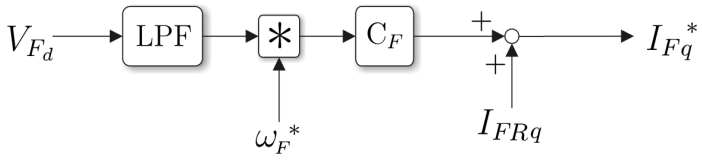

Figure 4.13: Open loop offshore ac grid frequency control

A possible solution consists on estimating the value of (I_{FRq}) by using local measurements. The (I_{FRq}) estimated has been obtained by using the active and reactive power delivered by the front-end converter. The expressions used to define (P_{Wn}) and (Q_{Wn}) are shown in the following equations.

$$P_{Wn} = 3\left(V_{Wd}I_{Fd} + V_{Wq}I_{Fq}\right) \tag{4.34}$$

$$Q_{Wn} = 3\left(V_{Wd}I_{Fq} - V_{Wq}I_{Fd}\right) \tag{4.35}$$

Therefore, by using 4.31 and the relations of (P_{Wn}) and (Q_{Wn}), the estimated value of (I_{FRq}) is represented by $(\hat{I}_{FRq})$ and it can be defined as follows:

$$\hat{I}_{FRq} = \frac{1}{3}\frac{P_{Wn}V_{Wq} - Q_{Wn}V_{Wd}}{V_{Wd}^2 + V_{Wq}^2} - C_F\omega_F V_{Fd} \tag{4.36}$$

Substituting 4.36 in 4.31, we have:

$$I_{Fq}^* = C_F V_{Fd}\left(\omega_F^* - \omega_F\right) + \frac{1}{3}\frac{P_{Wn}V_{Wq} - Q_{Wn}V_{Wd}}{V_{Wd}^2 + V_{Wq}^2} \tag{4.37}$$

According to equation 4.37 , its corresponding block diagram is shown in figure 4.14. The modified frequency control loop corresponds to a simple proportional control with a feedforward compensation term. Moreover, it is clear that the frequency control system is more robust to C_F estimation errors. This is due to the fact that C_F is icluded in the control loop and it can be considered as a loop gain, rather than a plant parameter. Note that equation 4.31 represents an algebraic relationship between (ω_F) and the front-end inverter reactive current (I_{Fq}). Therefore, the proportional

controller in figure 4.14 could, theoretically, drive (ω_F) to its reference instantaneously (the loop gain having only an influence on the steady state error). In this case, the dynamics of the current loop can be no longer neglected and hence the closed loop (ω_F) dynamics are the same as those of the (I_{Fd}) loop. Moreover, the filtered value of (V_{Fd}) introduces additional dynamics in the frequency control loop, although such effects can be easily minimized with adequate filter design.

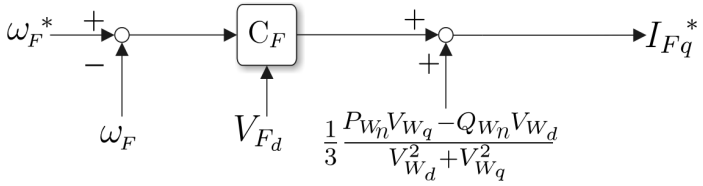

Figure 4.14: Modified frequency control loop

4.3.4 Protection Strategy and Fault Ride Through Capability

Wind farms of the considered size should be able to remain connected to the grid in spite of severe grid disturbances [54]. Therefore, a protection strategy, based on a voltage dependent current order limit (VDCOL) for each wind turbine is proposed. Figure 4.15 shows the characteristic response of the proposed VDCOL. Wherein, the protection will be carried out by imposing a limit on $|I_F|_{\max}$ according to the measured grid voltage (V_{Fd}). Besides, a rate limit of $|I_F|_{\max}$ will operate continuously during fault occurrences. It is worth noticing that, the proposed rate limits are consistent with standard practice to reduce oscillations and possible instability during fault recovery [2].

Based on the $|I_F|_{\max}$ limitation, the front-end converter currents (I_{Fd}) and (I_{Fq}) have to be also limited according to the following relationship:

$$I_{Fq\max} = |I_F|_{\max} \tag{4.38}$$

$$I_{Fd\max} = \min\left(\sqrt{|I_F|_{\max}^2 - I_{Fq}^2}\ ,\ I_{Fdopt}\right) \tag{4.39}$$

Therefore, the limit on (I_{Fq}) has to be obtained from the VDCOL characteristic, whereas, the limit on (I_{Fd}) will have the smaller of the following two quantities.

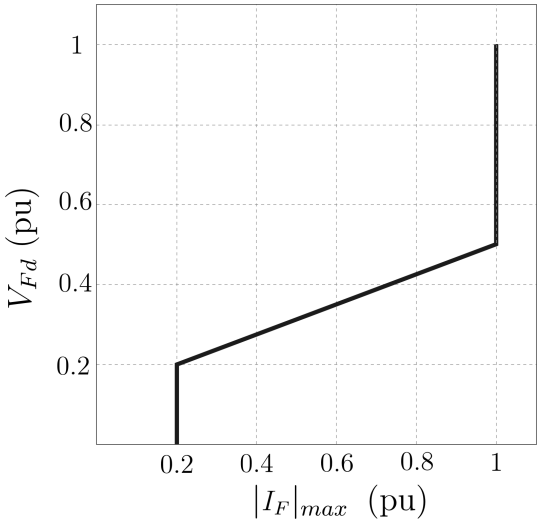

Figure 4.15: VDCOL protection characteristic

First, the expression $\sqrt{|I_F|^2_{\max} - I^2_{Fq}}$,which will be obtained from the VDCOL characteristic. Second, the optimal value (I_{Fdopt}), which represents the maximum power that can be extracted for a particular wind speed[44].

Figure 4.16 shows the protection strategy implemented on the (V_{Fd}) and (ω_F) control loops. Alternative protection schemes are possible, however, the proposed VDCOL has been chosen to show that the wind farm together with the diode rectifier can be operated in a similar way as traditional thyristor based HVdc rectifier.

Dynamic Braking

When a grid fault occurs and the generator is producing power that cannot be immediately delivered to the grid; is not able to reduce the generator speed quickly due to the slow dynamics of the speed control loop. As a consequence, the capacitor (C_{DC}) is overcharged producing an overvoltage on the dc-link voltage (E_{DC}). Although small variations are allowed in order to damp torsional oscillations in the drive train, the dc-link voltage should not exceed certain levels. Therefore, a resistive load in parallel with the dc-link capacitor (C_{DC}) is connected in order to discharge the capacitor

when its voltage rises above a certain level.

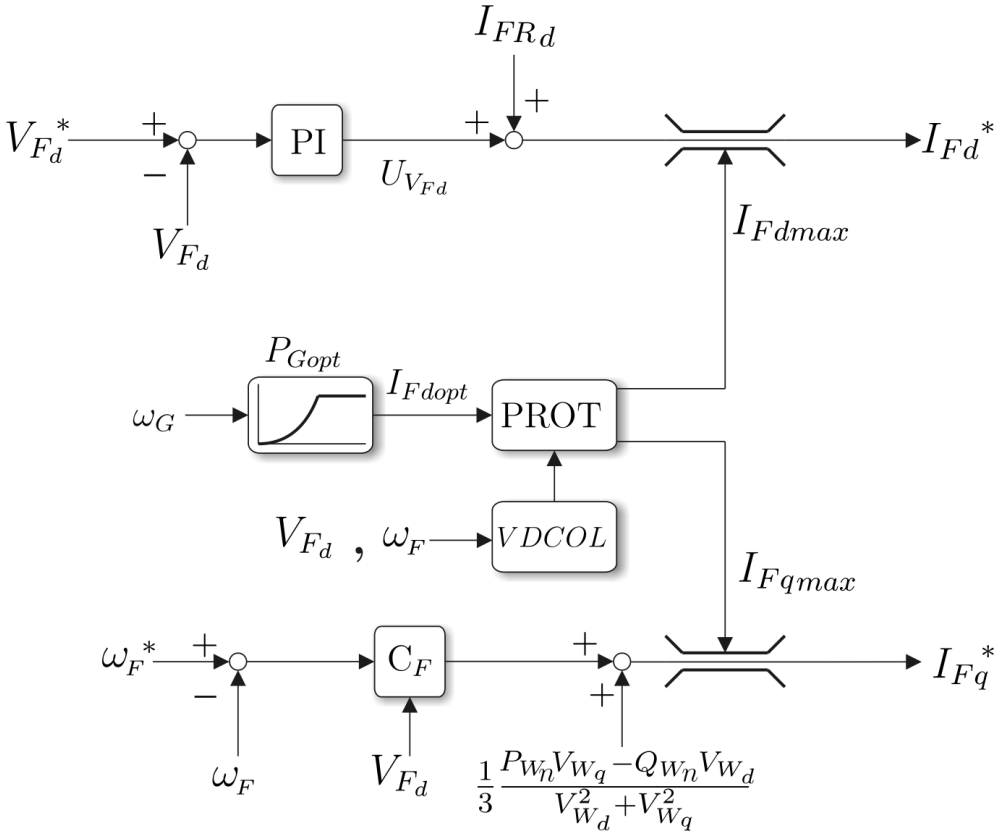

Figure 4.16: Limitations on the references of (I_{Fd}) and (I_{Fq})

4.4 Stability Analysis

The stability analysis will be carried out by analyzing the system eigenvalues. These characteristic values will be obtained from the small signal linearization of the system. Hence, a space state model of the complete offshore wind farm will have to be defined. Additionally, the presented analysis considers both, the connected operation mode and the islanded operation mode. Notice that, islanded operation mode can be obtained by assuming a no conduction condition in the HVdc rectifier, i.e. ($I_{Rdc} = 0$). Hence, in order to simplify the analysis, the connected operation mode will be the first one to be considered.

4.4.1 Stability analysis in connected operation mode

When offshore ac-grid overcomes the conduction condition, the aggregated model of the wind farm connected to the HVdc link can be represented by the diagram shown in figure 4.17.

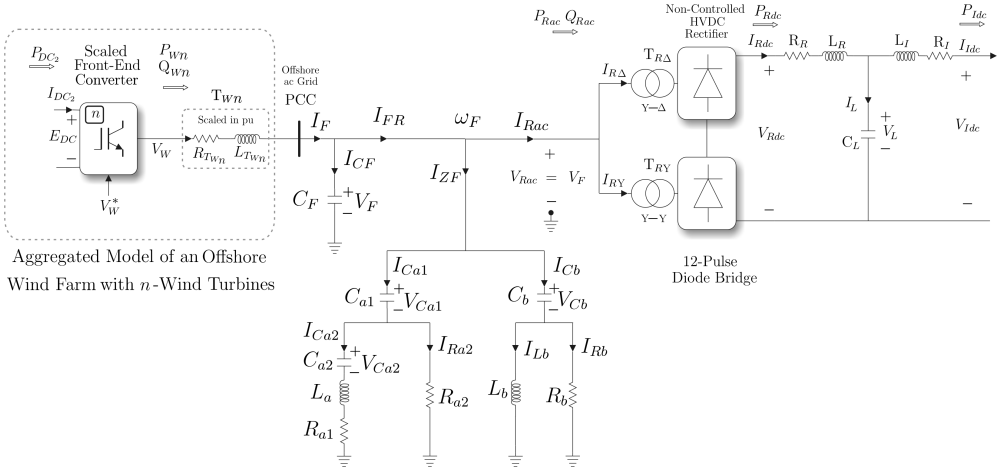

Figure 4.17: Offshore wind farm

This system has been modeled before in chapter 2 according to a generic synchronous frame rotating at frequency (ω_{dq}). But, by using equations 2.32, 2.33, 2.64 to 2.75, and placing the rotating frame on (V_F) i.e. ($\omega_{dq} = \omega_F$) and ($V_{Fq} = 0$). It is possible to define, the dynamics of the system shown in figure 4.17 as follows:

Dynamics of the front-end converter connected to the PCC

$$\frac{d}{dt}I_{Fd} = \frac{R_{T_{Wn}}}{L_{T_{Wn}}}I_{Fd} + \omega_F I_{Fq} + \frac{1}{L_{T_W}}V_{Wd} - \frac{1}{L_{T_W}}V_{Fd} \tag{4.40}$$

$$\frac{d}{dt}I_{Fq} = -\omega_F I_{Fd} - \frac{R_{T_{Wn}}}{L_{T_{Wn}}}I_{Fq} + \frac{1}{L_{T_W}}V_{Wq} \tag{4.41}$$

Dynamics of the offshore ac-grid voltage (V_{Fd}) and the HVdc filter bank

$$\frac{d}{dt}V_{Fd} = \frac{1}{C_F}I_{Fd} - \frac{1}{C_F}I_{FRd} \tag{4.42}$$

$$\frac{d}{dt}V_{Ca1d} = -\frac{1}{R_{a2}C_{a1}}V_{Ca1d} + \omega_F V_{Ca1q} + \frac{1}{C_{a1}}I_{Lad} + \frac{1}{R_{a2}C_{a1}}V_{Fd} \tag{4.43}$$

$$\frac{d}{dt}V_{Ca1q} = -\omega_F V_{Ca1d} - \frac{1}{R_{a2}C_{a1}}V_{Ca1q} + \frac{1}{C_{a1}}I_{Laq} \tag{4.44}$$

$$\frac{d}{dt}V_{Ca2d} = \omega_F V_{Ca2q} + \frac{1}{C_{a2}}I_{Lad} \tag{4.45}$$

$$\frac{d}{dt}V_{Ca2q} = -\omega_F V_{Ca2d} + \frac{1}{C_{a2}}I_{Laq} \tag{4.46}$$

$$\frac{d}{dt}I_{Lad} = -\frac{1}{L_a}V_{Ca1d} - \frac{1}{L_a}V_{Ca2d} - \frac{R_{a1}}{L_a}I_{Lad} + \omega_F I_{Laq} + \frac{1}{L_a}V_{Fd} \tag{4.47}$$

$$\frac{d}{dt}I_{Laq} = -\frac{1}{L_a}V_{Ca1q} - \frac{1}{L_a}V_{Ca2q} - \omega_F I_{Lad} - \frac{R_{a1}}{L_a}I_{Laq} \tag{4.48}$$

$$\frac{d}{dt}V_{Cbd} = -\frac{1}{R_b C_b}V_{Cbd} + \omega_F V_{Cbq} + \frac{1}{C_b}I_{Lbd} + \frac{1}{R_b C_b}V_{Fd} \tag{4.49}$$

$$\frac{d}{dt}V_{Cbq} = -\omega_F V_{Cbd} - \frac{1}{R_b C_b}V_{Cbq} + \frac{1}{C_b}I_{Lbq} \tag{4.50}$$

$$\frac{d}{dt}I_{Lbd} = -\frac{1}{L_b}V_{Cbd} + \omega_F I_{Lbq} + \frac{1}{L_b}V_{Fd} \tag{4.51}$$

$$\frac{d}{dt}I_{Lbq} = -\frac{1}{L_b}V_{Cbq} - \omega_F I_{Lbd} \tag{4.52}$$

Dynamics of the HVdc link

$$\frac{d}{dt}I_{Rdc} = \left[-\frac{R_R}{L_R} - \frac{3BL_{T_R}}{\pi L_R}\omega_F\right] I_{Rdc} + \frac{3NB\sqrt{6}}{\pi L_R}V_{Fd} - \frac{1}{L_R}V_L \tag{4.53}$$

$$\frac{d}{dt}I_{Idc} = -\frac{R_I}{L_I}I_{Rdc} - \frac{1}{L_I}V_{Idc} + \frac{1}{L_I}V_L \tag{4.54}$$

$$\frac{d}{dt}V_L = \frac{1}{C_L}I_{Rdc} - \frac{1}{C_L}I_{Idc} \tag{4.55}$$

Non linear dynamics

Equations 4.42 and 4.54 include the nonlinearity of the offshore wind farm model. However, in order to linearize the model two steps have to be carried out.
First, by assuming that, the onshore inverter will be controlled adequately by a minimum-γ strategy [2]; it is possible to consider the value of (V_{Idc}) as a constant disturbance. Hence, the linearized expression of equation 4.54 can be written as:

$$\frac{d}{dt}I_{Idc} = -\frac{R_I}{L_I}I_{Rdc} + \frac{1}{L_I}V_L \tag{4.56}$$

Second, regarding to equation 4.42, it is worth noticing that the nonlinearity is included in the (I_{FRd}) value. But, this expression shall be defined according to the dynamics imposed by the HVdc filter and the HVdc rectifier. Hence, according to figure 4.17, the value of (I_{FRd}) can be defined by:

$$I_{FRd} = I_{ZFd} + I_{Racd} \tag{4.57}$$

In order to calculate (I_{ZFd}), it is necessary to calculate the current passing through the HVdc filter as follows:

$$I_{ZF} = I_{Ca1} + I_{Cb} \tag{4.58}$$

the current of each filter branch can be defined by:

$$I_{Ca1} = I_{La} + \frac{V_F - V_{Ca1}}{R_{a2}} \tag{4.59}$$

$$I_{Cb} = I_{Lb} + \frac{V_F - V_{Cb}}{R_b} \tag{4.60}$$

Hence, by using the expressions of (I_{Ca1}) and (I_{Cb}), it is possible to define (I_{ZF}) as follows:

$$I_{ZF} = -\frac{1}{R_{a2}}V_{Ca1} + I_{La} + I_{Lb} - \frac{1}{R_b}V_{Cb} + \frac{R_{a2}+R_b}{R_{a2}R_b}V_F \tag{4.61}$$

by orienting the synchronous rotating frame on (V_F), the expressions for (I_{ZFd}) and (I_{ZFq}) are defined by the following equations:

$$I_{ZFd} = -\frac{1}{R_{a2}}V_{Ca1d} + I_{Lad} - \frac{1}{R_b}V_{Cbd} + I_{Lbd} + \frac{R_{a2}+R_b}{R_{a2}R_b}V_{Fd} \tag{4.62}$$

$$I_{ZFq} = -\frac{1}{R_{a2}}V_{Ca1q} + I_{Laq} - \frac{1}{R_b}V_{Cbq} + I_{Lbq} + \frac{R_{a2}+R_b}{R_{a2}R_b}V_{Fq} \tag{4.63}$$

Once obtained the expression for (I_{ZFd}), the value of (I_{Racd}) can be calculated by using the power relation on both sides of the diode rectifier. According to figure 4.17, the power on the ac-side and the dc-side of the rectifier can be written as:

$$P_{Rac} = 3V_{Fd}I_{Racd} \tag{4.64}$$

$$P_{Rdc} = V_{Rdc}I_{Rdc} \tag{4.65}$$

Moreover, the total power delivered to the HVdc link will be affected by the losses caused by the non-controlled diode bridges. Hence, by assuming (K_{Dloss}) as the diode rectifier losses, it is possible to define the following relationship:

$$P_{Rdc} = K_{Dloss}P_{Rac} \tag{4.66}$$

Therefore, by using equations 4.57, 4.64, 4.65 and 4.66, the expression for (I_{FRd}) can be defined as:

$$I_{FRd} = I_{ZFd} + \frac{V_{Rdc}I_{Rdc}}{3K_{Dloss}V_{Fd}} \tag{4.67}$$

Notice that, the value of (I_{ZFd}) was defined before by equation 4.62. Hence, the expression for (I_{FRd}) will be defined by:

$$I_{FRd} = -\frac{1}{R_{a2}}V_{Ca1d} + I_{Lad} - \frac{1}{R_b}V_{Cbd} + I_{Lbd} + \frac{R_{a2}+R_b}{R_{a2}R_b}V_{Fd} + \frac{V_{Rdc}I_{Rdc}}{3K_{Dloss}V_{Fd}} \tag{4.68}$$

Substituting the (I_{FRd}) expression in equation 4.42 , the dynamics of (V_{Fd}) will be defined as:

$$\begin{aligned}\frac{d}{dt}V_{Fd} &= \tfrac{1}{C_F}I_{Fd} - \frac{1}{C_F}\left(-\tfrac{1}{R_{a2}}V_{Ca1d} + I_{Lad}\right) + \cdots \\ &\cdots - \frac{1}{C_F}\left(-\tfrac{1}{R_b}V_{Cbd}I_{Lbd} + \tfrac{R_{a2}+R_b}{R_{a2}R_b}V_{Fd} + \tfrac{V_{Rdc}I_{Rdc}}{3K_{Dloss}V_{Fd}}\right)\end{aligned} \tag{4.69}$$

rewriting the equation

$$\begin{aligned}\frac{d}{dt}V_{Fd} &= \tfrac{1}{C_F}I_{Fd} + \tfrac{1}{C_F R_{a2}}V_{Ca1d} - \tfrac{1}{C_F}I_{Lad} + \cdots \\ &\cdots + \tfrac{1}{C_F R_b}V_{Cbd} - \tfrac{1}{C_F}I_{Lbd} - \tfrac{R_{a2}+R_b}{C_F R_{a2}R_b}V_{Fd} - \tfrac{V_{Rdc}I_{Rdc}}{3C_F K_{Dloss}V_{Fd}}\end{aligned} \tag{4.70}$$

It is important to remark that, there is a nonlinear term at the end of the equation. In the following, and only to simplify the notation, this nonlinear expression will be treated separately. Hence the following function $f(V_{Rdc}, I_{Rdc}, V_{Fd})$ will be defined:

$$f(V_{Rdc}, I_{Rdc}, V_{Fd}) = \frac{V_{Rdc}I_{Rdc}}{3C_F K_{Dloss}V_{Fd}} \tag{4.71}$$

Replacing (V_{Rdc}) by equation 2.76, the equivalent nonlinear relationship becomes to:

$$f(I_{Rdc}, V_{Fd}) = \tfrac{B\sqrt{6}N}{\pi C_F K_{Dloss}}I_{Rdc} - \tfrac{B\omega_F L_{T_R}}{\pi C_F K_{Dloss}}\frac{I_{Rdc}^2}{V_{Fd}} \tag{4.72}$$

Notice that, this non-linear expression includes the value of (I_{Rdc}); therefore, in islanded operation the conducting condition has not been overcome i.e. ($I_{Rdc} = 0$). Moreover, by using the first order terms of the Taylor expansion, it is possible to linearize the function $f(I_{Rdc}, V_{Fd})$ around the rated operation point $OP_{rat} = (I_{Rdc_0}, V_{Fd_0})$. The obtained expression can be written as follows:

$$\Delta f(\Delta I_{Rdc}, \Delta V_{Fd}) = \left.\frac{\partial f}{\partial I_{Rdc}}\right|_{OP_{rat}} \Delta I_{Rdc} + \left.\frac{\partial f}{\partial V_{F_d}}\right|_{OP_{rat}} \Delta V_{F_d} \tag{4.73}$$

for simplicity the differential notation (Δ) will be omitted. Hence, the linearized expression of $f(I_{Rdc}, V_{Fd})$ can be written as:

$$f(I_{Rdc}, V_{Fd}) = \tfrac{B\sqrt{6}NV_{Fd_0} - 2B\omega_F L_{T_R}I_{Rdc_0}}{\pi C_F K_{Dloss}V_{Fd_0}}I_{Rdc} + \tfrac{B\omega_F L_{T_R}I_{Rdc_0}^2}{\pi C_F K_{Dloss}V_{Fd_0}^2}V_{Fd} \tag{4.74}$$

By including $f(I_{Rdc}, V_{Fd})$ in equation 4.70, the linearized dynamics of (V_{Fd}) can be written as follows:

$$\begin{aligned}\frac{d}{dt}V_{Fd} &= \tfrac{1}{C_F}I_{Fd} + \tfrac{1}{C_F R_{a2}}V_{Ca1d} - \tfrac{1}{C_F}I_{Lad} + \tfrac{1}{C_F R_b}V_{Cbd} - \tfrac{1}{C_F}I_{Lbd} + \cdots \\ &\cdots - \tfrac{B\sqrt{6}NV_{Fd_0} - 2B\omega_F L_{T_R} I_{Rdc_0}}{\pi C_F K_{Dloss} V_{Fd_0}} I_{Rdc} - \left[\tfrac{B\omega_F L_{T_R} I_{Rdc_0}^2}{\pi C_F K_{Dloss} V_{Fd_0}^2} + \tfrac{R_{a2}+R_b}{C_F R_{a2} R_b}\right] V_{Fd}\end{aligned} \tag{4.75}$$

Linearized state space model of the offshore wind farm

The linearized state space model of the offshore wind farm in connected operation mode can be formulated by replacing equations 4.42 and 4.54 by equations 4.75 and 4.56 respectively. This new set of equations will describe the system dynamics around the rated operation point $OP_{rat} = (I_{Rdc_0}, V_{Fd_0})$. The resulting state equation of the linearized system will be denoted in matrix form as follows:

$$\dot{x} = Ax + Bu \tag{4.76}$$

where, (x) represents the state vector defined by:

$$\begin{aligned}x = [&I_{Fd}\ I_{Fq}\ V_{Fd}\ V_{Ca1d}\ V_{Ca1q}\ V_{Ca2d}\ V_{Ca2q}\ \cdots \\ &\ldots I_{Lad}\ I_{Laq}\ V_{Cbd}\ V_{Cbq}\ I_{Lbd}\ I_{Lbq}\ I_{Rdc}\ I_{Idc}\ V_L]^{\mathrm{T}}\end{aligned} \tag{4.77}$$

(u) is the input vector defined by:

$$u = [V_{Wd}\ V_{Wq}]^{\mathrm{T}} \tag{4.78}$$

and the state matrix (A) is a 16x16 matrix defined by the following elements:

$A_{(1,1)} = \frac{R_{T_{Wn}}}{L_{T_{Wn}}}$ $A_{(1,2)} = \omega_F$ $A_{(1,3)} = -\frac{1}{L_{T_{Wn}}}$ $A_{(2,1)} = -\omega_F$ $A_{(2,2)} = -\frac{R_{T_{Wn}}}{L_{T_{Wn}}}$

$A_{(3,1)} = \frac{1}{C_F}$ $A_{(3,3)} = -\frac{R_{a2}+R_b}{C_F R_{a2} R_b} - \frac{B\omega_F L_{T_R} I_{Rdc_0}^2}{\pi C_F K_{Dloss} V_{Fd_0}^2}$ $A_{(3,4)} = \frac{1}{C_F R_{a2}}$

$A_{(3,8)} = -\frac{1}{C_F}$ $A_{(3,10)} = \frac{1}{C_F R_b}$ $A_{(3,12)} = -\frac{1}{C_F}$ $A_{(3,14)} = -\frac{B\sqrt{6}NV_{Fd_0} - 2B\omega_F L_{T_R} I_{Rdc_0}}{\pi C_F K_{Dloss} V_{Fd_0}}$

$A_{(4,3)} = \frac{1}{R_{a2} C_{a1}}$ $A_{(4,4)} = -\frac{1}{R_{a2} C_{a1}}$ $A_{(4,5)} = \omega_F$ $A_{(4,8)} = \frac{1}{C_{a1}}$ $A_{(5,4)} = -\omega_F$

$A_{(5,5)} = -\frac{1}{R_{a2} C_{a1}}$ $A_{(5,9)} = \frac{1}{C_{a1}}$ $A_{(6,7)} = \omega_F$ $A_{(6,8)} = \frac{1}{C_{a2}}$ $A_{(7,6)} = -\omega_F$

$A_{(7,9)} = \frac{1}{C_{a2}}$ $A_{(8,3)} = \frac{1}{L_a}$ $A_{(8,4)} = -\frac{1}{L_a}$ $A_{(8,6)} = -\frac{1}{L_a}$ $A_{(8,8)} = -\frac{R_{a1}}{L_a}$

$A_{(8,9)} = \omega_F \quad A_{(9,5)} = -\frac{1}{L_a} \quad A_{(9,7)} = -\frac{1}{L_a} \quad A_{(9,8)} = -\omega_F \quad A_{(9,9)} = -\frac{R_{a1}}{L_a}$
$A_{(10,3)} = \frac{1}{R_b C_b} \quad A_{(10,10)} = -\frac{1}{R_b C_b} \quad A_{(10,11)} = \omega_F \quad A_{(10,12)} = \frac{1}{C_b}$
$A_{(11,10)} = -\omega_F \quad A_{(11,11)} = -\frac{1}{R_b C_b} \quad A_{(11,13)} = \frac{1}{C_b} \quad A_{(12,3)} = \frac{1}{L_b} \quad A_{(12,10)} = -\frac{1}{L_b}$
$A_{(12,13)} = \omega_F \quad A_{(13,11)} = -\frac{1}{L_b} \quad A_{(13,12)} = -\omega_F \quad A_{(14,3)} = \frac{3NB\sqrt{6}}{\pi L_R}$
$A_{(14,14)} = -\frac{R_R}{L_R} - \frac{3BL_{T_R}}{\pi L_R}\omega_F \quad A_{(14,16)} = -\frac{1}{L_R} \quad A_{(15,14)} = -\frac{R_I}{L_I} \quad A_{(15,16)} = \frac{1}{L_I}$
$A_{(16,14)} = \frac{1}{C_L} \quad A_{(16,15)} = -\frac{1}{C_L}$

and $A_{(i,j)} = 0$ for any other element not defined above.

Last, (B) is the input matrix defined by:

$$B = \begin{bmatrix} \frac{1}{L_{T_W}} & 0 & 0 & 0 & 0 & 0 & 0 & 0 & 0 & 0 & 0 & 0 & 0 & 0 & 0 & 0 \\ 0 & \frac{1}{L_{T_W}} & 0 & 0 & 0 & 0 & 0 & 0 & 0 & 0 & 0 & 0 & 0 & 0 & 0 & 0 \end{bmatrix}^{\mathrm{T}} \tag{4.79}$$

The values of the offshore wind farm components and parameters used to obtain the state equation are shown in tables 4.9 and 4.10.

PI Controller state space model

In order to perform the grid integration of the wind turbine, the electrical parameters of the offshore wind farm have been controlled by PI control loops of voltage and current. Figure 4.18 represents the generic block diagram of a single-input single-output (SISO) PI controller. According to this figure, it is possible to define the following equations :

$$\dot{x}_{PI} = \frac{1}{T_I} u_{PI} \tag{4.80}$$

$$y_{PI} = x_{PI} + K_P u_{PI} \tag{4.81}$$

This state model represents any PI controllers and will be used to close the control loop of the currents (I_{Fd}) and (I_{Fq}).

Inclusion of the (I_{Fd}) and (I_{Fq}) current controller

Two current loops have been implemented to set the (I_{Fd}) and (I_{Fq}) values. By using equations 4.80 and 4.81, the state model of (I_{Fd}) and (I_{Fq}) PI controller can be defined as a two-input two-output model (TITO) as follows:

Table 4.9: Values of the offshore wind farm components

Component	Units	Value
$R_{T_{Wn}}$	(mΩ)	595.125
$L_{T_{Wn}}$	(mH)	22.7321
C_F	(μF)	2.856
C_{a1}	(μF)	5.714
C_{a2}	(μF)	63.49
R_{a1}	(Ω)	34.82
R_{a2}	(Ω)	306.4
L_a	(mH)	159.6
C_b	(μF)	5.714
R_b	(Ω)	97.49
L_b	(mH)	15.91
L_{T_R}	(mH)	50
R_R	(Ω)	2.50
L_R	(mH)	0.5968
C_L	(μF)	26
R_I	(Ω)	2.50
L_I	(mH)	0.5968

Table 4.10: Parameters of the offshore wind farm

Term	Units	Value
K_{Dloss}	-	0.98
B	-	2
N	-	0.61871
$V_{Fd0\ (\text{L-N}rms)}$	(V)	193600
I_{Rdc0}	(A)	2000
ω_F	(rad/s)	314.159

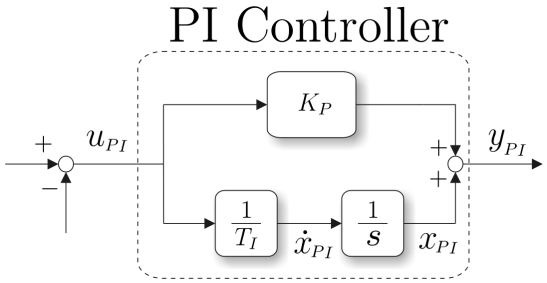

Figure 4.18: Generic PI controller (SISO)

$$\begin{bmatrix} \frac{d}{dt}x_{ccd} \\ \frac{d}{dt}x_{ccq} \end{bmatrix} = \begin{bmatrix} \frac{1}{T_{Iccd}} & 0 \\ 0 & \frac{1}{T_{Iccq}} \end{bmatrix} \begin{bmatrix} u_{ccd} \\ u_{ccq} \end{bmatrix} \tag{4.82}$$

$$\begin{bmatrix} y_{ccd} \\ y_{ccq} \end{bmatrix} = \begin{bmatrix} 1 & 0 \\ 0 & 1 \end{bmatrix} \begin{bmatrix} x_{ccd} \\ x_{ccq} \end{bmatrix} + \begin{bmatrix} K_{Pccd} & 0 \\ 0 & K_{Pccq} \end{bmatrix} \begin{bmatrix} u_{ccd} \\ u_{ccq} \end{bmatrix} \tag{4.83}$$

The values of K_{Pccd}, K_{Pccq}, T_{Iccd} and T_{Iccq} have been defined in table 4.7. Writing the controller expression in compact form, the following equations are defined:

$$\dot{x}_{cc} = B_{cc}u_{cc} \tag{4.84}$$

$$y_{cc} = C_{cc}x_{cc} + D_{cc}u_{cc} \tag{4.85}$$

Once obtained the state space representation of the PI controller, it is possible to close the current control loops. By using the offshore wind farm model, and defining (I_{Fd}) and (I_{Fq}) as system outputs, the output equation can be written in compact form as:

$$y = Cx \tag{4.86}$$

where, the output vector (y) is defined by:

$$y = \begin{bmatrix} I_{Fd} & I_{Fq} \end{bmatrix}^{\mathrm{T}} \tag{4.87}$$

besides, (C) is the output matrix defined by:

$$C = \begin{bmatrix} 1 & 0 & 0 & 0 & 0 & 0 & 0 & 0 & 0 & 0 & 0 & 0 & 0 & 0 & 0 & 0 \\ 0 & 1 & 0 & 0 & 0 & 0 & 0 & 0 & 0 & 0 & 0 & 0 & 0 & 0 & 0 & 0 \end{bmatrix} \tag{4.88}$$

and (x) is the state vector defined before in equation 4.77.

In order to perform the close loop, the following two new inputs will be defined:

$$u_{ref} = \begin{bmatrix} I^*_{Fd} \\ I^*_{Fq} \end{bmatrix} \tag{4.89}$$

As mentioned before it is assumed that the onshore inverter is controlled adequately by a minimum-γ strategy [2]. Therefore, the value of (V_{Idc}) has been not included as system input in equation 4.89 (it has been considered as a constant disturbance).

The control law will be defined by:

$$u_{cc} = u_{ref} - y \tag{4.90}$$

$$y_{cc} = u = C_{cc}x_{cc} + D_{cc}u_{cc} \tag{4.91}$$

therefore

$$y_{cc} = C_{cc}x_{cc} + D_{cc}u_{ref} - D_{cc}y \tag{4.92}$$

but $y = Cx$, then

$$y_{cc} = C_{cc}x_{cc} + D_{cc}u_{ref} - D_{cc}Cx \tag{4.93}$$

as $y_{cc} = u$, the new state equation can be defined as:

$$\dot{x} = Ax + B\left[C_{cc}x_{cc} + D_{cc}u^* - D_{cc}Cx\right] \tag{4.94}$$

rewriting the equation

$$\dot{x} = \left[A - BD_{cc}C\right]x + BC_{cc}x_{cc} + BD_{cc}u^* \tag{4.95}$$

But, the state equation of the controller is:

$$\dot{x}_{cc} = B_{cc} u_{cc} \tag{4.96}$$

as $y = Cx$ and $u_{cc} = u_{ref} - y$, then

$$\dot{x}_{cc} = -B_{cc} C x + B_{cc} u_{ref} \tag{4.97}$$

By using the state equations 4.95 and 4.97, a new system can be conformed by the following augmented state equation:

$$\begin{bmatrix} \dot{x} \\ \dot{x}_{cc} \end{bmatrix} = \begin{bmatrix} A - BD_{cc}C & BC_{cc} \\ -B_{cc}C & 0 \end{bmatrix} \begin{bmatrix} x \\ x_{cc} \end{bmatrix} + \begin{bmatrix} BD_{cc} \\ B_{cc} \end{bmatrix} [u_{ref}] \tag{4.98}$$

This new state space model includes the current controller dynamics and hereafter will be denoted in compact form as:

$$\dot{x}_{cl} = A_{cl} x_{cl} + B_{cl} u_{cl} \tag{4.99}$$

Inclusion of the (V_{Fd}) voltage controller

A voltage control loop has been implemented to set the value of (V_{Fd}). By using equations 4.80 and 4.81, the state model of the PI controller for the voltage control loop can be defined as:

$$\frac{d}{dt} x_{vc} = \frac{1}{T_{Ivc}} u_{vc} \tag{4.100}$$

$$y_{vc} = x_{vc} + K_{Pvc} u_{vc} \tag{4.101}$$

The values of K_{Pvc} and T_{Ivc} have been defined in table 4.8. Writing the controller expression in standard nomenclature, the following equations are defined:

$$\dot{x}_{vc} = B_{vc} u_{vc} \tag{4.102}$$

$$y_{vc} = C_{vc} x_{vcc} + D_{vc} u_{vc} \tag{4.103}$$

Once obtained the state space representation of the PI controller, it is possible to close the voltage control loop. By using equation 4.99, and defining (V_{Fd}) as system

output. The output equation related to the system can be written in compact form as:

$$y_{cl} = C_{cl} x_{cl} \tag{4.104}$$

where, the output vector (y_{cl}) is defined by:

$$y_{cl} = V_{Fd} \tag{4.105}$$

besides, (C_{cl}) is the the output matrix defined by:

$$C_{cl} = \begin{bmatrix} 0 & 0 & 1 & 0 & 0 & 0 & 0 & 0 & 0 & 0 & 0 & 0 & 0 & 0 & 0 & 0 & 0 & 0 \end{bmatrix} \tag{4.106}$$

and (x_{cl}) is the state vector defined by concatenating the state vector of the system with the state vector of the current controller.

$$x_{cl} = \begin{bmatrix} x & x_{cc} \end{bmatrix}^{\mathrm{T}} \tag{4.107}$$

In order to perform the close loop, the new input (V_{Fd}^*) will be defined in conjunction with the following control law:

$$u_{vc} = V_{Fd}^* - y_{cl} \tag{4.108}$$

$$y_{cl} = V_{Fd} = C_{cl} x_{cl} \tag{4.109}$$

therefore

$$y_{vc} = C_{vc} x_{vc} + D_{vc} V_{Fd}^* - D_{vc} V_{Fd} \tag{4.110}$$

substituting the value of (V_{Fd}) by $V_{Fd} = C_{cl} x_{cl}$

$$y_{vc} = C_{vc} x_{vc} + D_{vc} V_{Fd}^* - D_{vc} C_{cl} x_{cl} \tag{4.111}$$

As the voltage control loop will be closed with the system input (I_{Fd}^*), i.e. $y_{vc} = I_{Fd}^*$, the state equation 4.99 shall be rewritten as follows:

$$\dot{x}_{cl} = A_{cl}x_{cl} + B_{cl1}I^*_{Fd} + B_{cl2}I^*_{Fq} \tag{4.112}$$

where, (B_{cl1}) and (B_{cl2}) correspond to the first and second column of the matrix (B_{cl}) respectively. The new state equation will be defined as:

$$\dot{x}_{cl} = A_{cl}x_{cl} + B_{cl1}\left(C_{vc}x_{vc} + D_{vc}V^*_{Fd} - D_{vc}C_{cl}x_{cl}\right) + B_{cl2}I^*_{Fq} \tag{4.113}$$

rewriting the equation

$$\dot{x}_{cl} = \left(A_{cl} - B_{cl1}D_{vc}C_{cl}\right)x_{cl} + B_{cl1}C_{vc}x_{vc} + B_{cl1}D_{vc}V^*_{Fd} + B_{cl2}I^*_{Fq} \tag{4.114}$$

But, the state equation of the controller is:

$$\dot{x}_{vc} = B_{vc}u_{vc} \tag{4.115}$$

replacing (u_{vc}) by $u_{vc} = V^*_{Fd} - y_{cl}$ and then (y_{cl}) by $y_{cl} = C_{cl}x_{cl}$

$$\dot{x}_{vc} = -B_{vc}C_{cl}x_{cl} + B_{vc}V^*_{Fd} \tag{4.116}$$

By using the state equations 4.114 and 4.116, a new system can be conformed by the following augmented state equation:

$$\begin{bmatrix} \dot{x}_{cl} \\ \dot{x}_{vc} \end{bmatrix} = \begin{bmatrix} A_{cl} - B_{cl1}D_{vc}C_{cl} & B_{cl1}C_{vc} \\ -B_{vc}C_{cl} & 0 \end{bmatrix} \begin{bmatrix} x_{cl} \\ x_{vc} \end{bmatrix} + \begin{bmatrix} B_{cl1}D_{vc} & B_{cl2} \\ B_{vc} & 0 \end{bmatrix} \begin{bmatrix} V^*_{Fd} \\ I^*_{Fq} \end{bmatrix} \tag{4.117}$$

This model includes both, the current controller dynamics and the voltage controller dynamics. Hereafter, this new state space model will be denoted in compact form as:

$$\dot{x}_{vl} = A_{vl}x_{vl} + B_{vl}u_{vl} \tag{4.118}$$

Eigenvalues in connected operation mode

Equations 4.99 and 4.118 include not only the dynamics of the offshore wind farm, but also theirs corresponding controllers. Therefore, during connected operation the system stability will be carried out analyzing the location of theirs eigenvalues. In current control mode the eigenvalues are calculated with the state matrix (A_{cl}) (equation 4.99). Likewise, in voltage control mode the eigenvalues are calculated with the state matrix (A_{vl}) (equation 4.118).

Notice that both equations (4.99 and 4.118) represent the linearized model of the offshore wind farm assuming constant values of (C_F) and (ω_F). But, in practice these values are subject to small variations of both (C_F) and (ω_F). Small changes in (C_F) can be due to the reactive power compensation and harmonic filter bank; whereas, small distortions in frequency (ω_F) can be associated to grid transients. In any case, the main aim is to ensure that the eigenvalues remain stable during variations of (C_F) and (ω_F).

According to equation 4.99, figure 4.19 shows the eigenvalues plot when (C_F) varies from $0.856\,\mu$F to $4.856\,\mu$F. In addition, the zoom of the region closer to the inestability area (right-hand plane) is shown in figure 4.20. Notice that poles of (C_F) are located relatively far away as shown in figure 4.19. Hence, according to 4.20 it is possible to say that the system dynamics are weakly influenced in presence variations of (C_F).

Similarly, when (ω_F) varies from $125.66\,\mathrm{rad/s}$ to $628.32\,\mathrm{rad/s}$ figure 4.21 shows the location plot of the system eigenvalues. The zoom of the more relevant poles of this figure can be seen in figure 4.22. In contrast to figure 4.20 the damping of the systems is severely affected in presence of large variations of (ω_F).

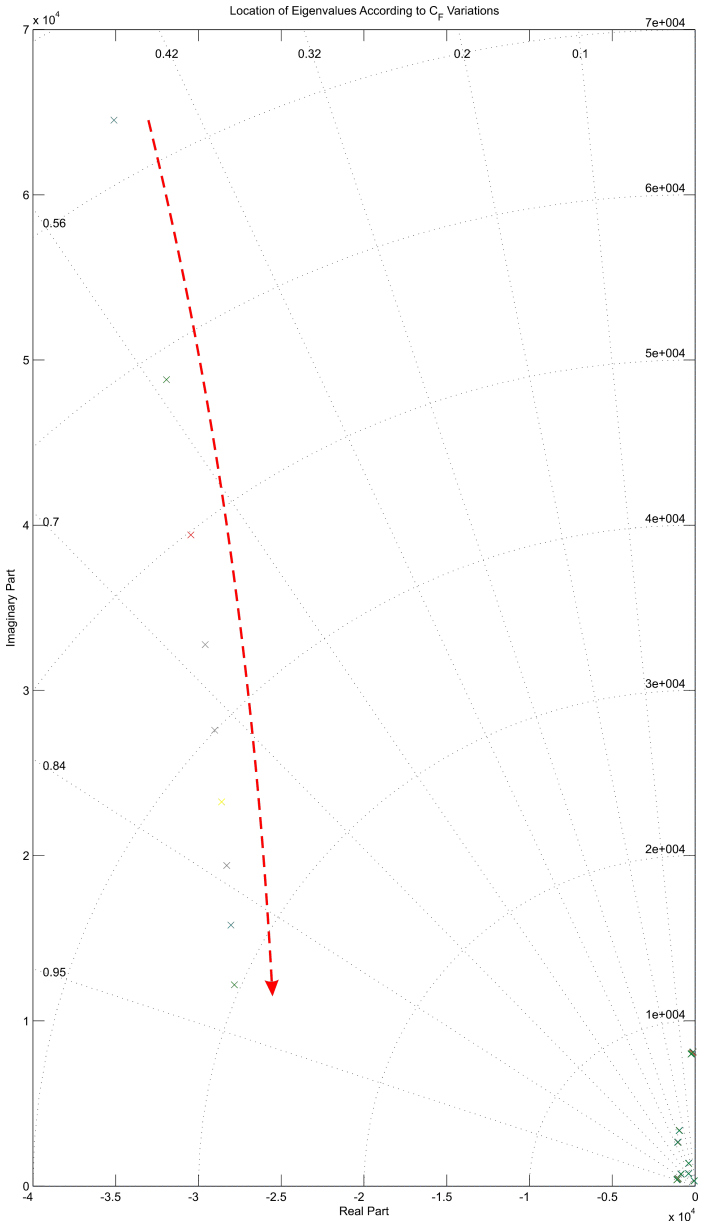

Figure 4.19: Eigenvalues in current control mode and connected operation with (C_F) varying from 0.856 to 4.856 [μF]

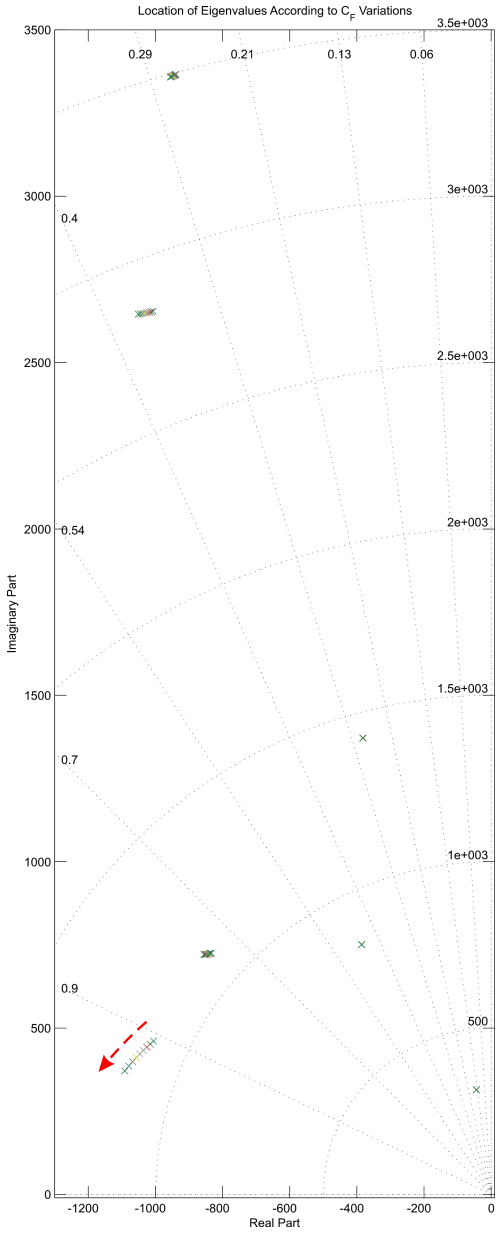

Figure 4.20: Zoom of the eigenvalues in current control mode and connected operation with (C_F) varying from 0.856 to 4.856 [μF]

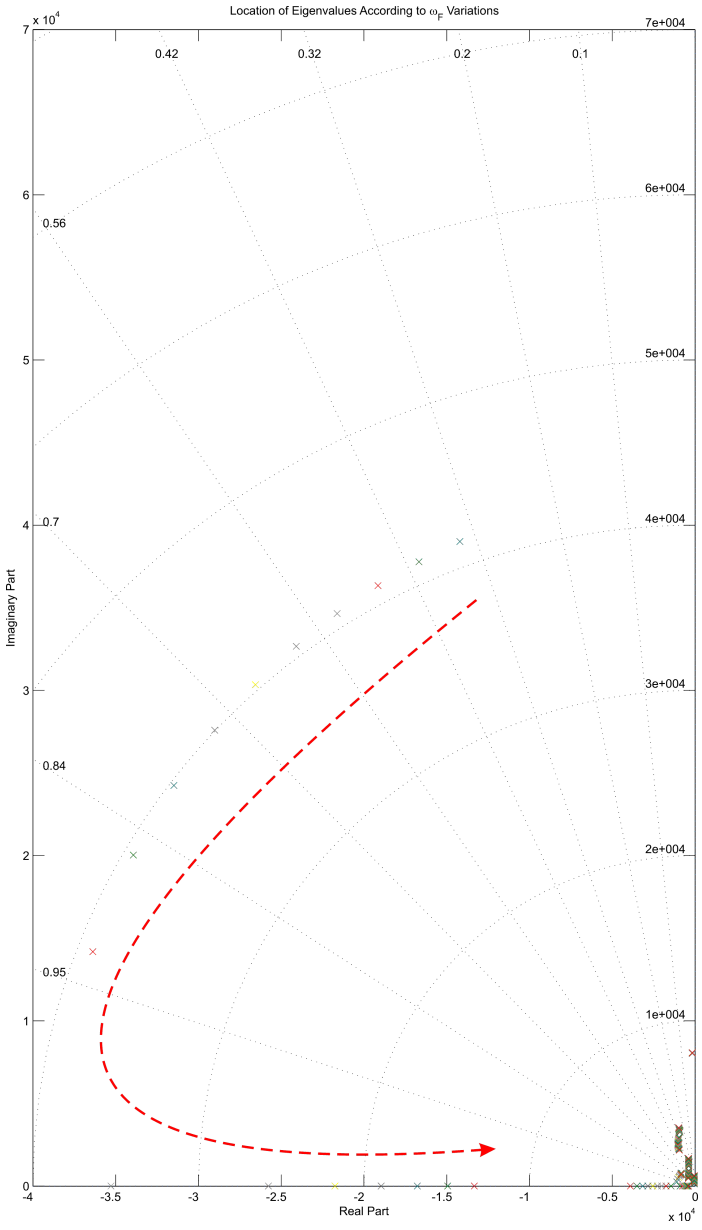

Figure 4.21: Eigenvalues in current control mode and connected operation with (ω_F) varying from 125.6 to 628.32 [rad/s]

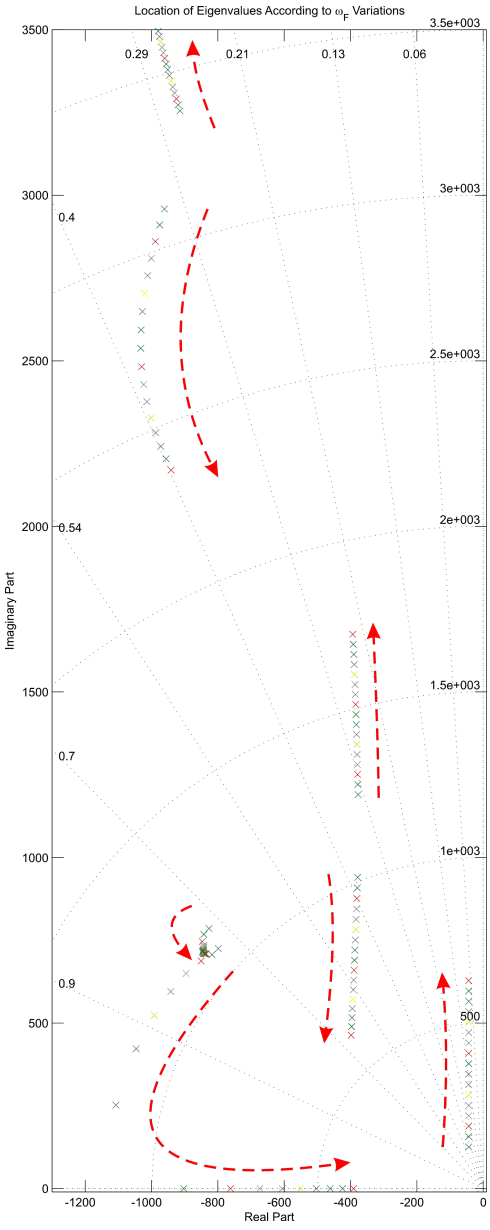

Figure 4.22: Zoom of the eigenvalues in current control mode and connected operation with (ω_F) varying from 125.6 to 628.32 [rad/s]

As can be seen in figures 4.19,4.20,4.21 and 4.22, during current control mode it is possible to define clear trends and bounded zones according to the path defined by the eigenvalues. In addition, when there are variations of (C_F) and (ω_F), it is clear that the system eigenvalues remain in the left-hand plane (stable condition). However, although figure 4.22 shows that the system can remain stable, its damping can be affected negatively in presence of (ω_F) variations.

Once the voltage control loop is closed, the system is defined by equation 4.118. This equation represents the dynamics of the offshore wind farm during voltage control mode. Therefore, the state matrix (A_{vl}) will be used to calculate the eigenvalues for different values of (C_F) and (ω_F). Figure 4.23 shows the eigenvalues plot when (C_F) varies from $0.856\,\mu$F to $4.856\,\mu$F. In addition, the zoom of the region closer to the inestability area (right-hand plane) is shown in figure 4.24. Notice that according to this figure it is possible to see the influence of the voltage controller over the the poles of (C_F). But, as in the current control mode, the system dynamics are also weakly influenced during variations of (C_F).

Moreover, when (ω_F) varies from $125.66\,\mathrm{rad/s}$ to $628.32\,\mathrm{rad/s}$, the system response is quite similar than the one obtained with the current control loop. This due to the fact that during connected operation the offshore ac-voltage is clamped by the HVdc link voltage. Hence, comparing figures 4.21 and 4.22 with figures 4.25 and 4.26 respectively, it is possible to see that the voltage control loop affects weakly the system dynamics.

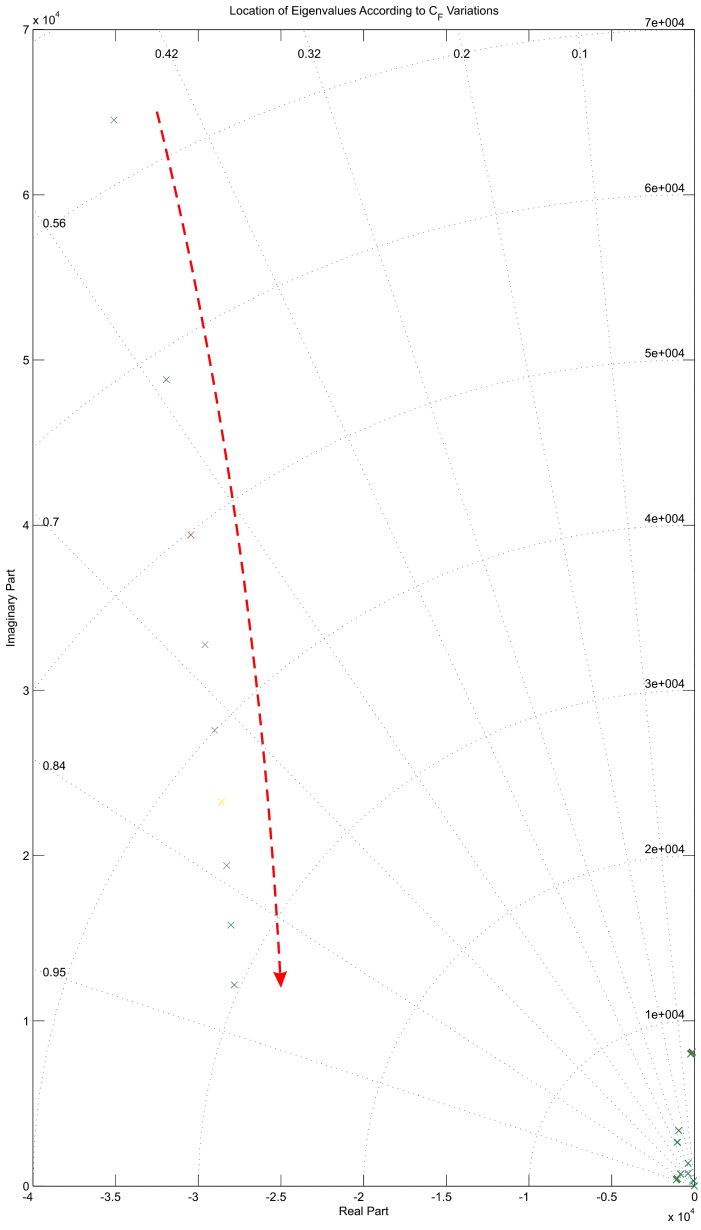

Figure 4.23: Eigenvalues in voltage control mode and connected operation with (C_F) varying from 0.856 to 4.856 [μF]

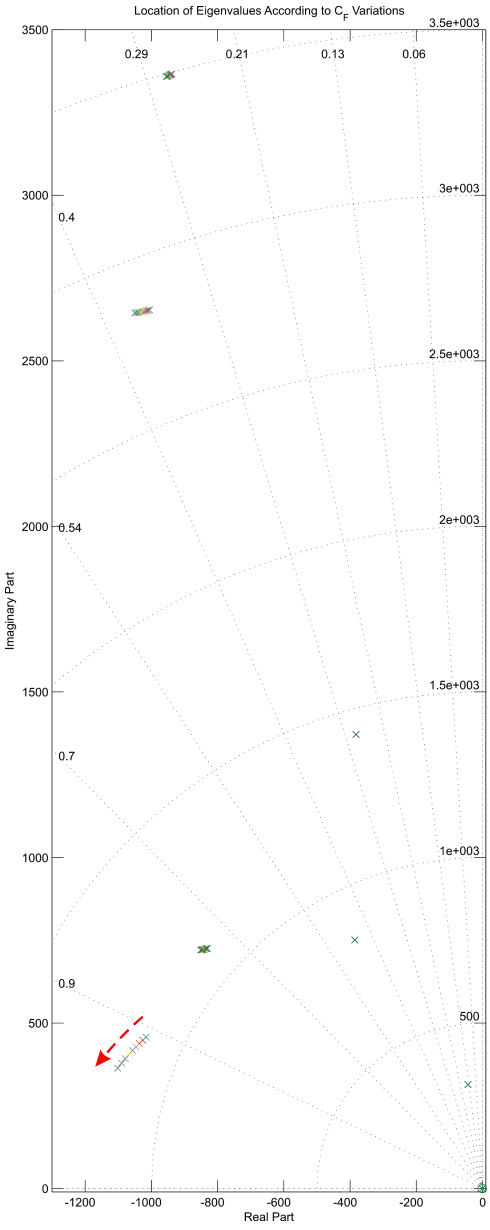

Figure 4.24: Zoom of the eigenvalues in voltage control mode and connected operation with (C_F) varying from 0.856 to 4.856 [μF]

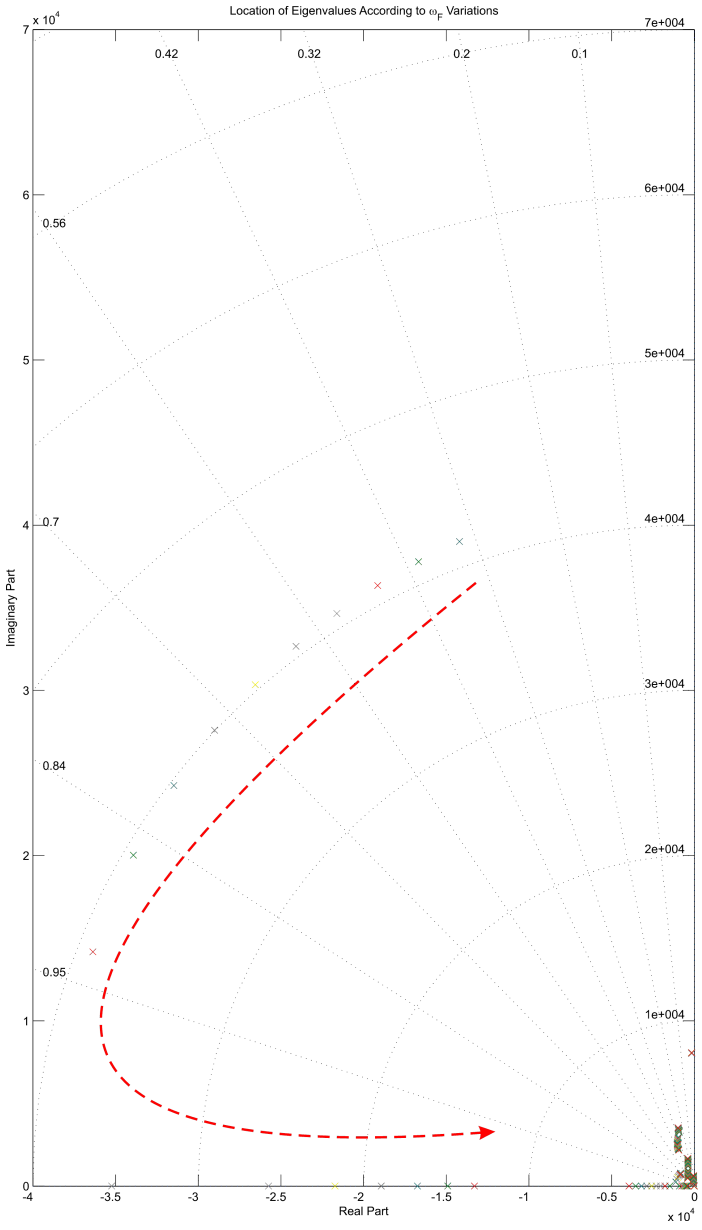

Figure 4.25: Eigenvalues in voltage control mode and connected operation with (ω_F) varying from 125.6 to 628.32 [rad/s]

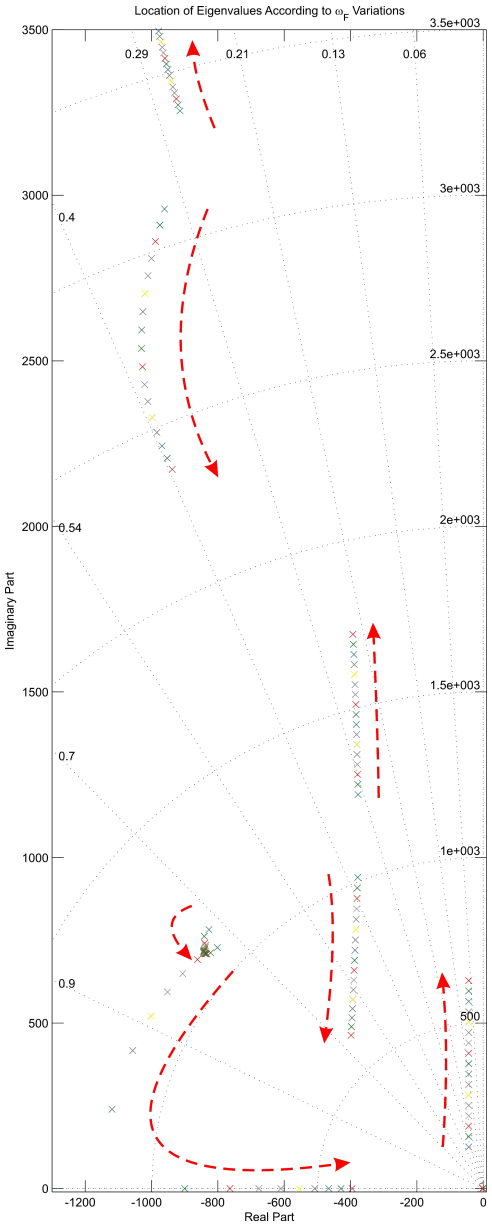

Figure 4.26: Zoom of the eigenvalues in voltage control mode and connected operation with (ω_F) varying from 125.6 to 628.32 [rad/s]

4.4.2 Stability analysis in islanded operation mode

As commented before, the stability analysis in islanded operation can be simplified by using the analysis performed in connected operation mode. In islanded operation it is possible to assume a non conducting condition in the HVdc rectifier. Therefore, the current passing through the diodes can be neglected. Figure 4.27 shows the equivalent circuit assuming that the HVdc rectifier is not conducting.

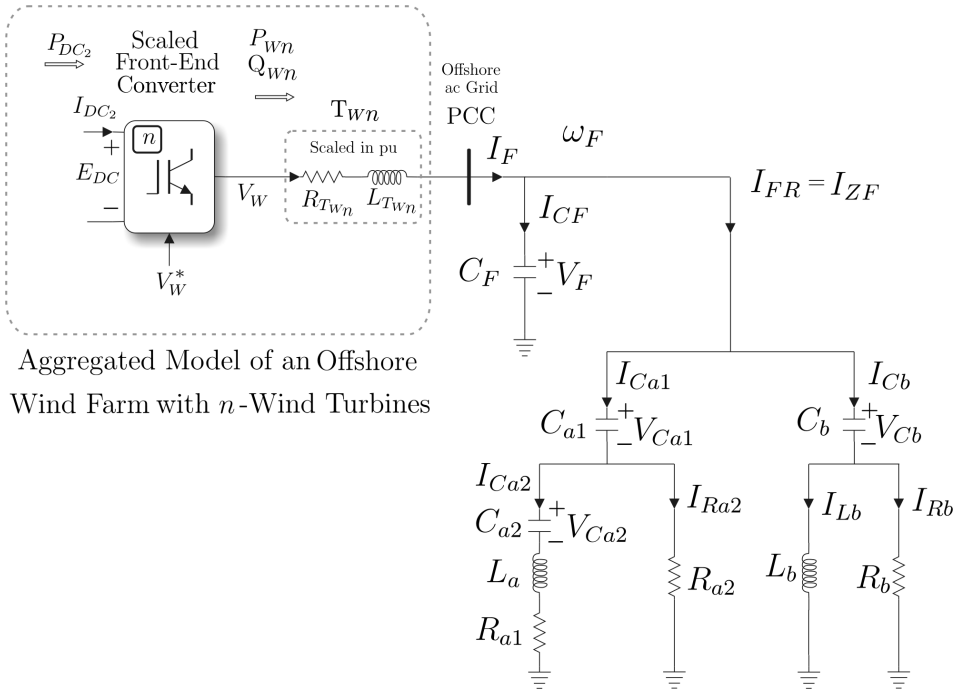

Figure 4.27: Offshore wind farm in islanded mode

According to figure 4.27, it is possible to modify the initial equations that have been used before to model the system in connected operation mode. The modifications are shown in the set of equations 4.119 to 4.131. In these equations, the dynamics of I_{Rdc}, I_{Idc} and V_L are not included. Besides, the non linear term $\frac{V_{Rdc}I_{Rdc}}{3K_{Dloss}V_{Fd}}$ defined for the dynamic equation of (V_{Fd}) in connected mode, has been neglected.

$$\frac{d}{dt}I_{Fd} = \frac{R_{T_{Wn}}}{L_{T_{Wn}}}I_{Fd} + \omega_F I_{Fq} + \frac{1}{L_{T_W}}V_{Wd} - \frac{1}{L_{T_W}}V_{Fd} \tag{4.119}$$

$$\frac{d}{dt}I_{Fq} = -\omega_F I_{Fd} - \frac{R_{T_{Wn}}}{L_{T_{Wn}}}I_{Fq} + \frac{1}{L_{T_W}}V_{Wq} \tag{4.120}$$

$$\frac{d}{dt}V_{Fd} = \frac{1}{C_F}I_{Fd} + \frac{1}{C_F R_{a2}}V_{Ca1d} - \frac{1}{C_F}I_{Lad} + \frac{1}{C_F R_b}V_{Cbd} - \frac{1}{C_F}I_{Lbd} - \frac{R_{a2}+R_b}{C_F R_{a2} R_b}V_{Fd} \tag{4.121}$$

$$\frac{d}{dt}V_{Ca1d} = -\frac{1}{R_{a2}C_{a1}}V_{Ca1d} + \omega_F V_{Ca1q} + \frac{1}{C_{a1}}I_{Lad} + \frac{1}{R_{a2}C_{a1}}V_{Fd} \tag{4.122}$$

$$\frac{d}{dt}V_{Ca1q} = -\omega_F V_{Ca1d} - \frac{1}{R_{a2}C_{a1}}V_{Ca1q} + \frac{1}{C_{a1}}I_{Laq} \tag{4.123}$$

$$\frac{d}{dt}V_{Ca2d} = \omega_F V_{Ca2q} + \frac{1}{C_{a2}}I_{Lad} \tag{4.124}$$

$$\frac{d}{dt}V_{Ca2q} = -\omega_F V_{Ca2d} + \frac{1}{C_{a2}}I_{Laq} \tag{4.125}$$

$$\frac{d}{dt}I_{Lad} = -\frac{1}{L_a}V_{Ca1d} - \frac{1}{L_a}V_{Ca2d} - \frac{R_{a1}}{L_a}I_{Lad} + \omega_F I_{Laq} + \frac{1}{L_a}V_{Fd} \tag{4.126}$$

$$\frac{d}{dt}I_{Laq} = -\frac{1}{L_a}V_{Ca1q} - \frac{1}{L_a}V_{Ca2q} - \omega_F I_{Lad} - \frac{R_{a1}}{L_a}I_{Laq} \tag{4.127}$$

$$\frac{d}{dt}V_{Cbd} = -\frac{1}{R_b C_b}V_{Cbd} + \omega_F V_{Cbq} + \frac{1}{C_b}I_{Lbd} + \frac{1}{R_b C_b}V_{Fd} \tag{4.128}$$

$$\frac{d}{dt}V_{Cbq} = -\omega_F V_{Cbd} - \frac{1}{R_b C_b}V_{Cbq} + \frac{1}{C_b}I_{Lbq} \tag{4.129}$$

$$\frac{d}{dt}I_{Lbd} = -\frac{1}{L_b}V_{Cbd} + \omega_F I_{Lbq} + \frac{1}{L_b}V_{Fd} \tag{4.130}$$

$$\frac{d}{dt}I_{Lbq} = -\frac{1}{L_b}V_{Cbq} - \omega_F I_{Lbd} \tag{4.131}$$

This set of equations can be written in compact form by the following state equation

$$\dot{x} = Ax + Bu \tag{4.132}$$

where, (x) represents the state vector defined by:

$$x = [I_{Fd}\ I_{Fq}\ V_{Fd}\ V_{Ca1d}\ V_{Ca1q}\ V_{Ca2d}\ V_{Ca2q}\ I_{Lad}\ I_{Laq}\ V_{Cbd}\ V_{Cbq}\ I_{Lbd}\ I_{Lbq}]^{\mathrm{T}} \tag{4.133}$$

(u) is the input vector defined by:

$$u = [V_{Wd}\ V_{Wq}]^{\mathrm{T}} \tag{4.134}$$

and, (B) is the input matrix defined by:

$$B = \begin{bmatrix} \frac{1}{L_{T_W}} & 0 & 0 & 0 & 0 & 0 & 0 & 0 & 0 & 0 & 0 & 0 & 0 \\ 0 & \frac{1}{L_{T_W}} & 0 & 0 & 0 & 0 & 0 & 0 & 0 & 0 & 0 & 0 & 0 \end{bmatrix}^{\mathrm{T}} \tag{4.135}$$

Notice that this system is completely linear and it represents the same system defined before for connected mode but without the states I_{Rdc}, I_{Idc}, V_L and the non linear term $\frac{V_{Rdc}I_{Rdc}}{3K_{Dloss}V_{Fd}}$. Moreover, the same nomenclature has been used in order to take advantage of the analysis carried out to include the controllers of current and voltage. Hence, if the system in islanded mode is described by $\dot{x} = Ax + Bu$, and additionally the same current and voltage controllers are used, then the equations 4.99 and 4.118 continues being valid during islanded operation.

Eigenvalues in islanded operation mode

Similarly to the analysis performed in connected mode, the system stability in islanded mode will be carried out by analyzing the eigenvalues location in presence of variations of (C_F) and (ω_F). During islanded mode of operation, the system works only in voltage control mode. Therefore, the stability will be defined by the eigenvalues of (A_{vl}) in equation 4.118. Figure 4.28 shows the eigenvalues plot when (C_F) is varied from $0.856\,\mu$F to $4.856\,\mu$F. Besides, figure 4.29 represents the zoom on the area closer to the right-hand plane. According to these figures it is clear that variations of (C_F) only affect the location of the poles that have less influence on the system dynamics. Moreover, figure 4.30 shows the eigenvalues plot when (ω_F) varies from $125.66\,\mathrm{rad/s}$ to $628.32\,\mathrm{rad/s}$. The zoom on the area closer to the right-hand plane is shown in figure 4.31. As in connected mode these variations of (ω_F) also affect negatively the system damping. However, in contrast to connected mode, during islanded operation, the system dynamics have been simplified (the HVdc link has not been included). Therefore, comparing figures 4.22, 4.26 and 4.31 it is clear that the eigenvalues show smaller position variation during islanded operation than during connected operation for a similar range of (C_F) and (ω_F) variation.

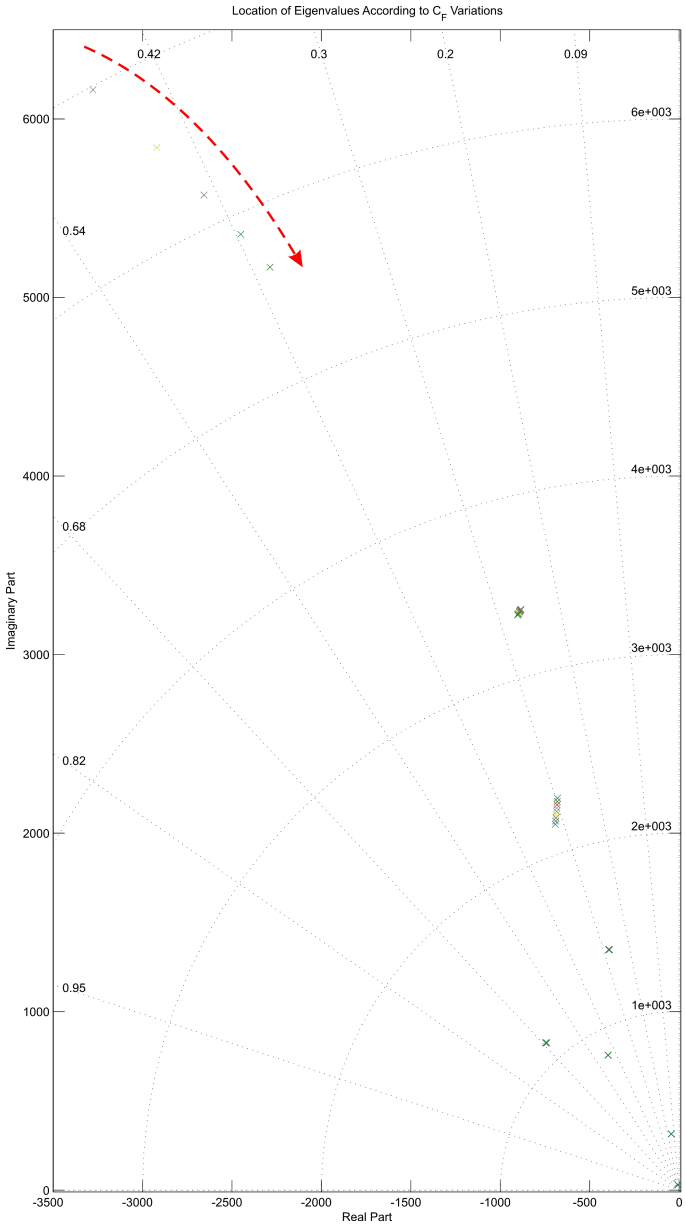

Figure 4.28: Eigenvalues in voltage control mode and islanded operation with (C_F) varying from 0.856 to 4.856 [μF]

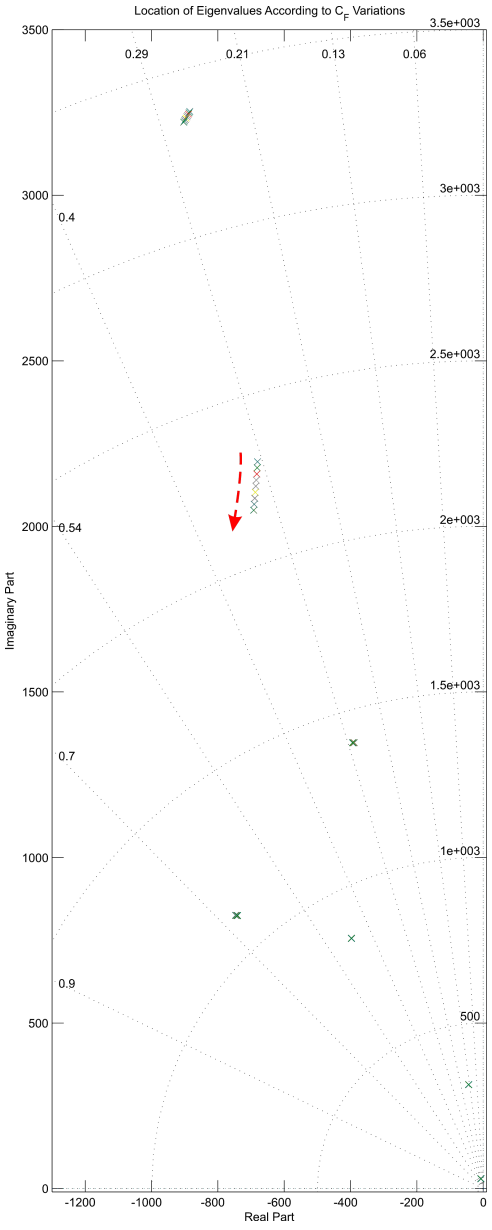

Figure 4.29: Zoom of the eigenvalues in voltage control mode and islanded operation with (C_F) varying from 0.856 to 4.856 [μF]

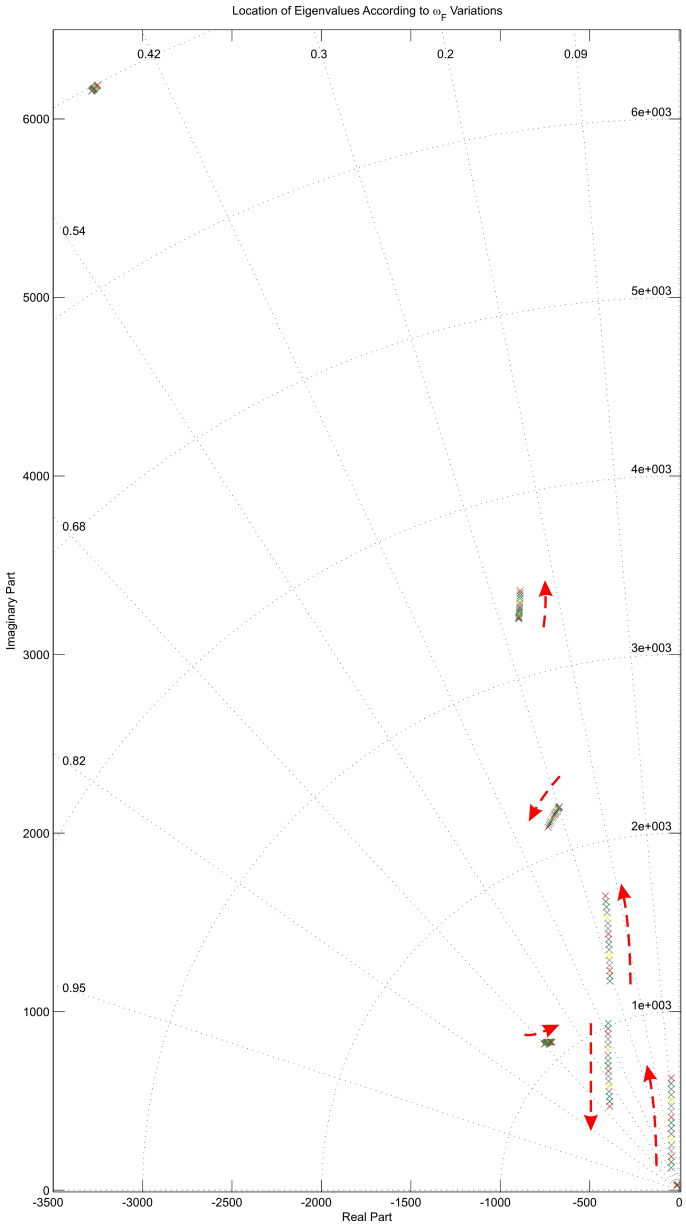

Figure 4.30: Eigenvalues in voltage control mode and islanded operation with (ω_F) varying from 125.6 to 628.32 [rad/s]

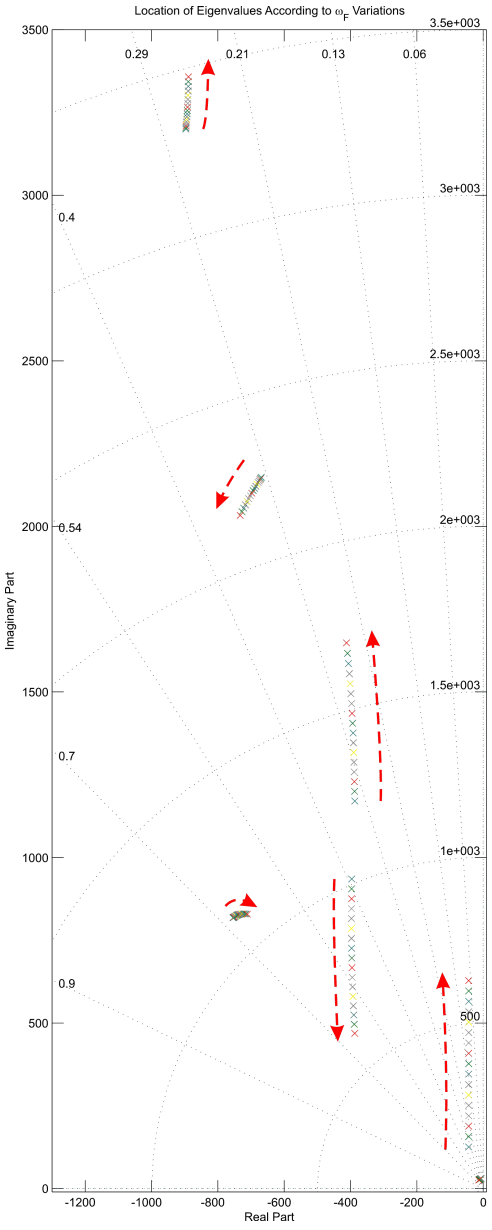

Figure 4.31: Zoom of the eigenvalues in voltage control mode and islanded operation with (ω_F) varying from 125.6 to 628.32 [rad/s]

4.5 Results

The validation of the previously described control strategy has been carried out using PSCAD^{TM} simulations. The parameters of the HVdc link have been obtained from the CIGRE benchmark model [39], wherein a diode-based rectifier has been used instead of a thyristor-based rectifier. Besides, the onshore inverter station has been modeled by means of a variable voltage dc-source emulating as well, an onshore inverter in voltage control mode of operation [25], [26].

Additionally, the bandwidth of the current control loop has been designed to be around 180 Hz. This bandwidth is consistent with a wind turbine front-end converter operating at 1 kHz switching frequency. When used, the base values for the corresponding per unit (pu) magnitudes are shown in table 4.11.

Table 4.11: Base values of the offshore ac grid and the HVdc link

Component	Parameter	Base Value	Units
Offshore ac-grid	V_F	193.6	(kV) L-N rms
	I_F	1.745	(kA) L-N rms
	ω_F	50	(Hz)
Transformer (T_R)	Rated Power	603.73	(MVA)
	Rated Freq.	50	(Hz)
	$V_{TR1} : V_{TR2}$	345/213	(kV) L-L rms
	$X_{L_{TR}}$	0.18	(pu)
HVdc Link	V_{Rdc}	500	(kV)
	P_{Rdc}	1000	(MW)

4.5.1 Offshore ac-grid and HVdc link start-up operation

Figure 4.32 shows the start-up operation of the offshore ac-grid. As mentioned before, the HVdc diode rectifier or, in general, an LCC rectifier cannot start the offshore ac-grid by itself, even if the HVdc link is energized. Therefore, the wind farm should perform this operation. Initially, it is assumed that an ancillary equipment energizes the HVdc link and ramps up the (V_{Rdc}) value. Once the HVdc voltage has reached its rated value, the voltage and frequency control loops of the wind farm are enabled and consequently, the voltage reference (V^*_{Fd}) is ramped-up to 1.1 pu in 1.7 s.

Note that the reactive current of the wind farm increases while the offshore ac-grid voltage reaches its rated value. This is due to the fact that the HVdc rectifier is not yet conducting and, therefore, the reactive power delivered by the capacitor bank is absorbed by the wind farm. Once (V_{Fd}) reaches the value $\frac{\sqrt{6}}{36}\frac{\pi}{N}V_{Rdc}$ (at t = 1.7 s), the HVdc diode rectifier starts conducting and (I_{Fd}) and (I_{Rdc}) increase to their rated values. At the same time, (I_{Fq}) decreases while the capacitor bank reactive power compensates the reactive power absorbed by both the leakage reactance of transformer (T_R) and the overlap angle of the HVdc rectifier. Note the reduction of ($I_{Fd\,\max}$) when (I_{Fq}) increases to keep the allowable output current below its rated level, as per equation 4.39.

When operating at rated (V_{Fd}) voltage, the active power delivered by the wind farm (P_{Wn}) is roughly proportional to wind farm active current (I_{Fd}). During operation at rated power, the wind farm delivered reactive power is zero. Figure 4.32 also shows the waveforms corresponding to phase r of (V_F) and the ac-side currents of the diode bridge (I_{FR}).

Figure 4.33 shows a detail of the previously shown start-up transient. When (V_{Fd}) reaches a value of 0.9 pu (at t = 1.7 s), the offshore rectifier starts conducting and currents (I_{Fd}) and (I_{Rdc}) increase. As current (I_{Rdc}) increases, the (V_{Rdc}) ripple increases due to the higher harmonic content at higher currents.

When (I_{Fd}) reaches its limit ($I_{Fd\,\max}$) at t = 1.89 s, the voltage control loop in figure 4.16 saturates and the offshore grid voltage (V_{Fd}) does no longer follow its reference. Therefore, figure 4.33 shows a smooth transition between voltage and current control

mode of operation.

The ac-grid frequency remains close to 50 Hz during the voltage ramp-up. However, once the rectifier starts conducting, the offshore ac-voltage shows an increased harmonic content, which causes the frequency and HVdc link voltage ripple in figure 4.33. When the diode rectifier is not conducting, wind turbine speed (ω_R) is kept at its rated value (14.8 rpm) by means of pitch control. Once the HVdc link starts conducting, active power is extracted from the wind farm causing a small drop in wind turbine speed. At this point, the pitch angle of the wind turbine (β) is reduced at its maximum rate. During the connection transient, the minimum wind turbine speed is 13.5 rpm. After the minimum pitch angle is reached $\beta = 0^o$, the wind turbine speeds returns to 14.8 rpm. The wind speed during the transient is 11.48 m/s.

The transients in figures 4.32 and 4.33 show reliable steady state operation at rated power. Moreover, before the HVdc diode rectifier starts conducting, the proposed control algorithm shows an excellent stand alone operation, with good voltage and frequency regulation.

4.5.2 Response to frequency changes at rated power

The performance of the frequency control loop is shown in figure 4.34. The system is operating in current control mode at rated power. At t = 0.1 s the frequency demand rises to 52 Hz (1.04 pu) and then is changed back to 50 Hz (at t = 0.3 s). A similar transient is carried out, but now reducing the frequency demand to 48 Hz. The behavior of the control system is remarkable as the actual frequency reaches its reference value in around 12 ms. The rest of the magnitudes remain constant during the transients. Only minor variations on (I_{Fq}), (V_{Fd}) and (Q_{Wn}) can be appreciated. These variations are due to the frequency dependant nature of the reactive power of the capacitor bank, filters and leakage reactances.

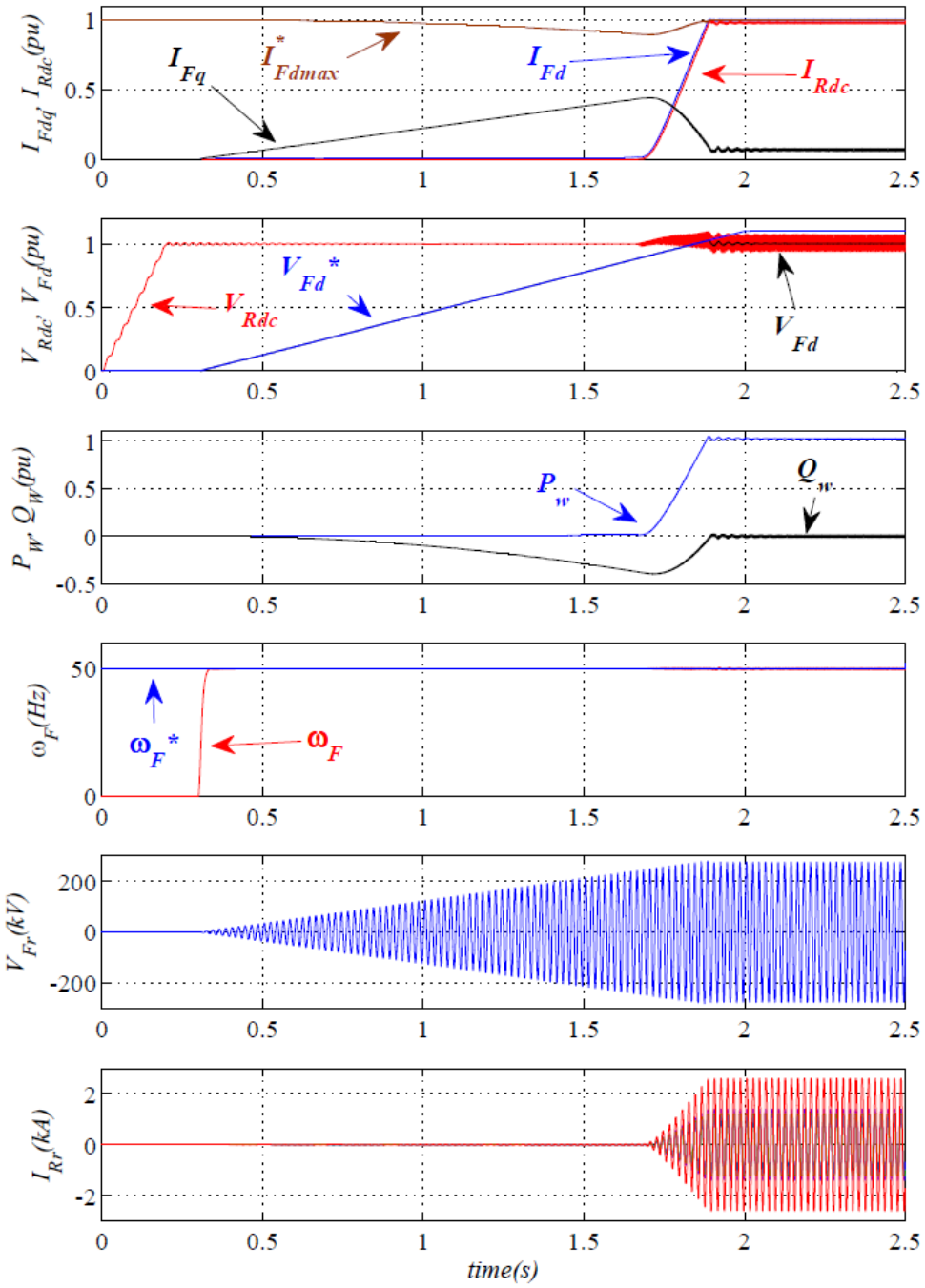

Figure 4.32: Offshore grid black-start operation

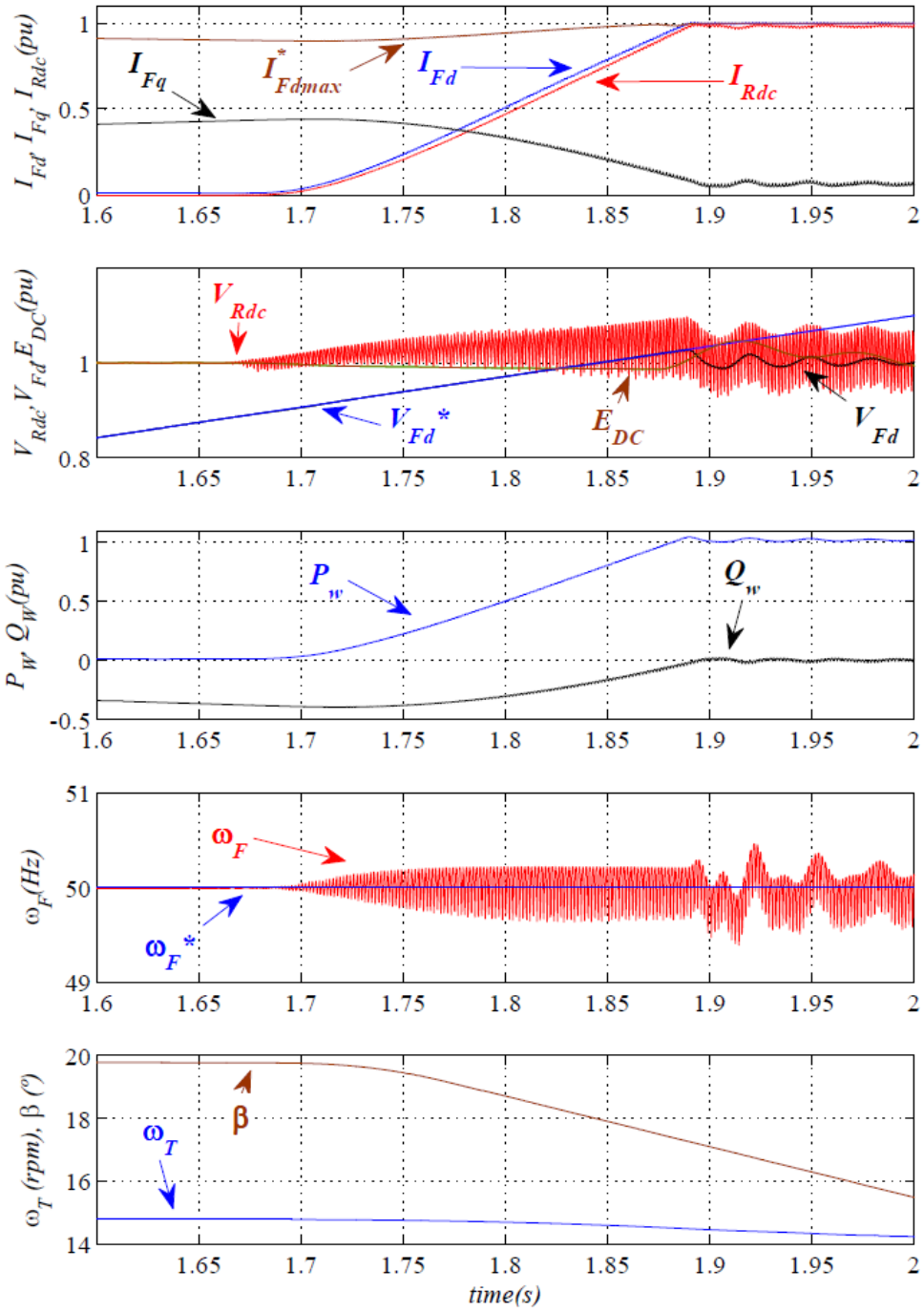

Figure 4.33: Response to offshore ac-voltage reference ramp

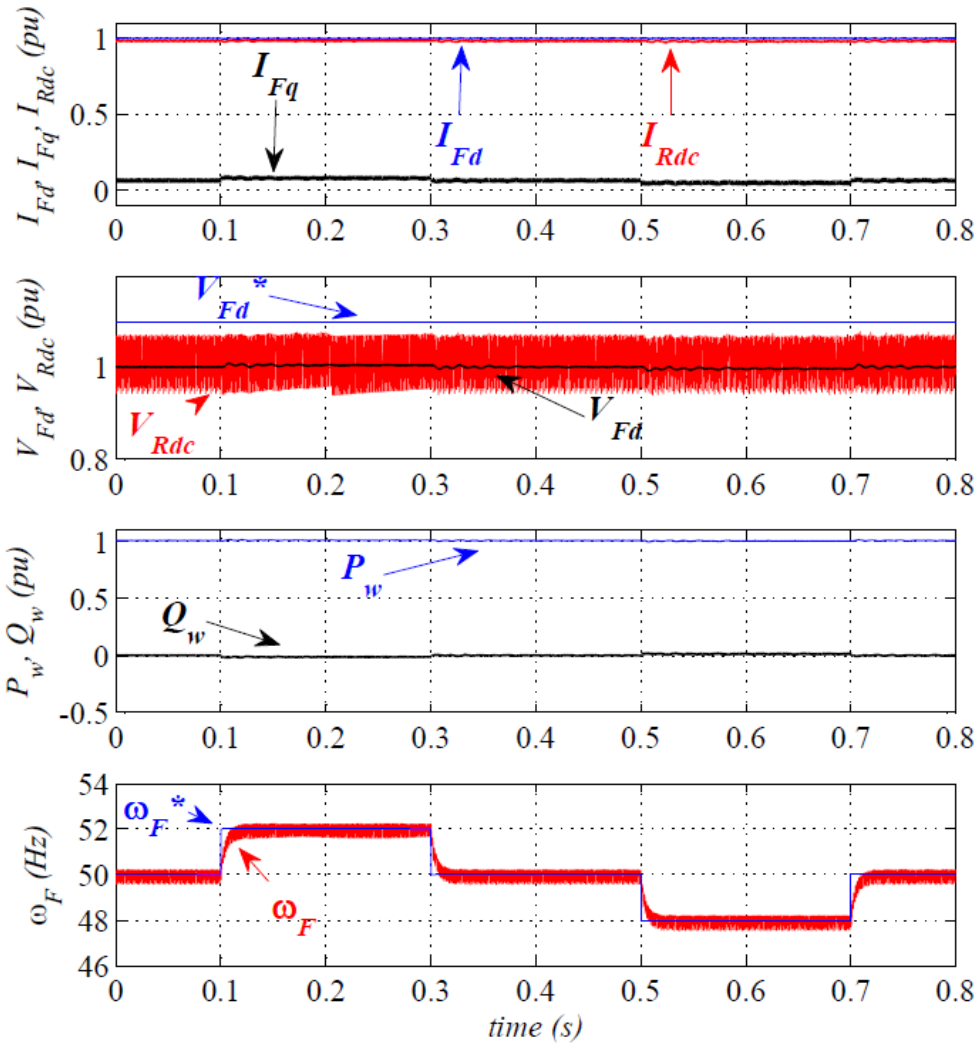

Figure 4.34: Response to frequency demand changes at rated power

4.5.3 Wind farm power control

Figure 4.35 shows the response of the system to changes in the wind farm power set-point. The value of ($I_{Fd\,\max}$) in figure 4.16 has been reduced from 1 to 0.1 pu in 0.3 s and then ramped up to 1 pu to simulate power variations for changing wind conditions.

Note (I_{Fq}) increases as (I_{Fd}) decreases, since the capacitor bank is overcompensating the reactive power absorbed by the rectifier transformer leakage reactance. This fact is consistent with the increased (Q_{Wn}) absorption shown in the third graph. On the other hand, the HVdc link and offshore ac-grid voltages decrease slightly along with (I_{Fd}) due to smaller voltage drop on the HVdc link resistance and rectifier transformer leakage reactance. It is worth noticing the decreased harmonic content in the HVdc link voltage (V_{Rdc}) at reduced power levels. During the complete transient, the offshore ac-grid frequency is kept very close to its reference value.

Note a 0.9 pu power transient in 0.3 s might not be realistic, as power generated from a wind farm of this size does not vary so rapidly. Nevertheless, figure 4.35 shows an excellent behavior of the proposed control system during power reference changes.

Optimal power tracking for different wind conditions is shown in figure 4.36. From an initial value of 5 m/s, the wind speed is increased to rated wind speed 11.48 m/s. The wind turbine rotational speed increases to reach rated speed and rated power operation. At t=14 s, the wind speed is further increased to 15 m/s to illustrate pitch angle (β) control at high wind speed.

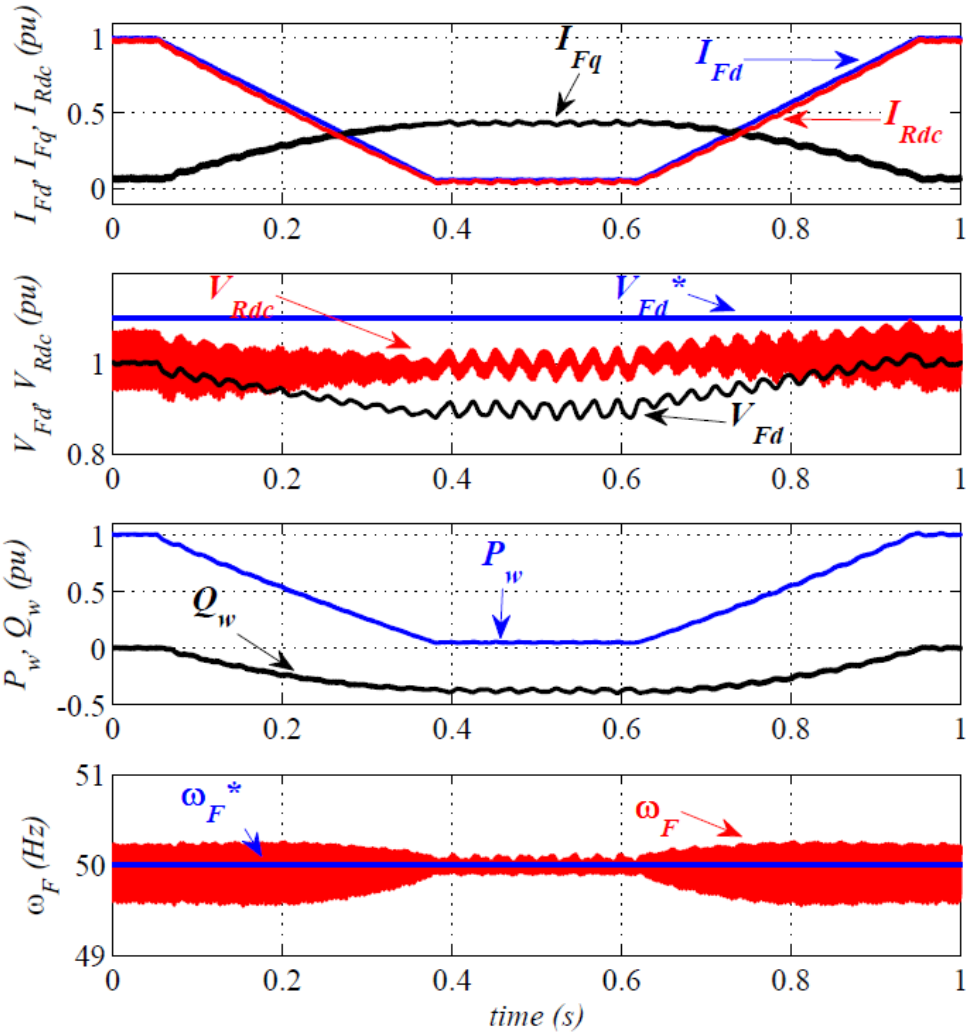

Figure 4.35: Response to changes in wind farm power set-point

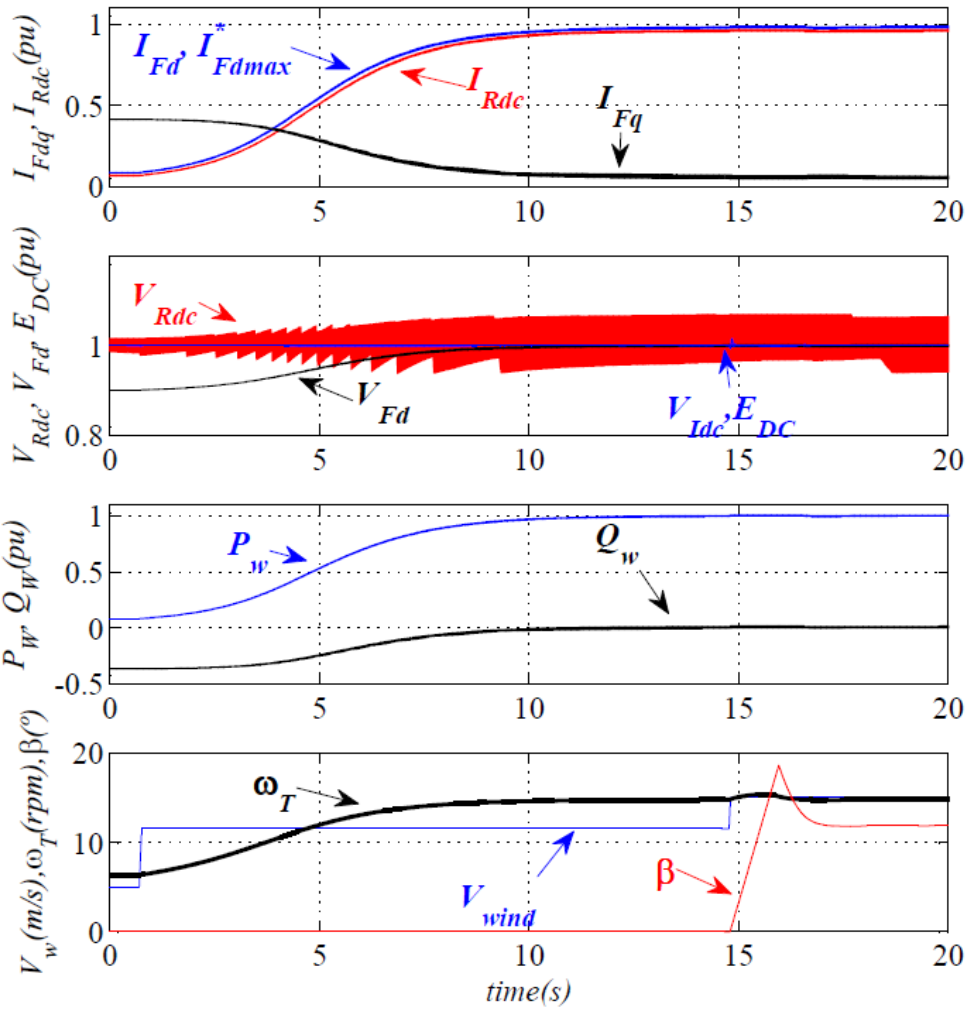

Figure 4.36: Optimal power tracking

4.5.4 Fault-ride-through performance during onshore faults

Figure 4.37 shows the response of the system to a three phase onshore grid short circuit at the inverter terminals. The fault has a duration of 400 ms, a 100% depth, and a 100 ms recovery time to 100% of the pre-fault voltage. During the fault, the VDCOL mechanism reduces (I_{Fd}) and (I_{Fq}) due to the small (V_{Fd}) values caused by the fault. As a result, the diode bridge stops conducting and the HVdc link (I_{Rdc}) current decreases following the link unforced dynamics.

The behavior of the HVdc link current has been analyzed theoretically assuming a short circuit at the onshore inverter terminals and an instantaneous voltage reduction at the offshore rectifier terminals. The HVdc link natural (unforced) response can be expressed as:

$$I_{Rdc} = 2e^{-\frac{R}{L}t} + \frac{1000\sqrt{C}}{\sqrt{8L-CR^2}} e^{-\frac{R}{2L}t} \sin(\omega_n t) \tag{4.136}$$

$$I_{Idc} = 2e^{-\frac{R}{L}t} + \frac{1000\sqrt{C}}{\sqrt{8L-CR^2}} e^{-\frac{R}{2L}t} \cos(\omega_n t) \tag{4.137}$$

where R, L, and C are the HVdc characteristic parameters and:

$$\omega_n = \frac{1}{2}\sqrt{\frac{8}{LC} - \frac{R^2}{L^2}} \tag{4.138}$$

Therefore, the maximum rectifier (and inverter) current will be:

$$\hat{I}_{Rdc} \backsimeq 2 + \frac{1000\sqrt{C}}{\sqrt{8L-CR^2}} \tag{4.139}$$

Substituting the R, L, C values used in the CIGRE benchmark yields $\omega_n = 57$ Hz and $\hat{I}_{Rdc\text{peak}} = 4.33$ kA $= 2.17$ pu. These values are consistent with the results shown in figure 4.37. Note the peak current is slightly higher in figure 4.37 ($\hat{I}_{Rdc} \backsimeq 2.5$ pu) as the rectifier side dc-voltage does not decrease to zero instantaneously. Clearly, in order to reduce ($\hat{I}_{Rdc}$), a good option would be an increased value of the serial smoothing reactance. However, such an increase will lead to longer current decay times according to equation 4.38. On the other hand, an increase on the cable capacitance will lead to larger maximum values of (I_{Rdc}).

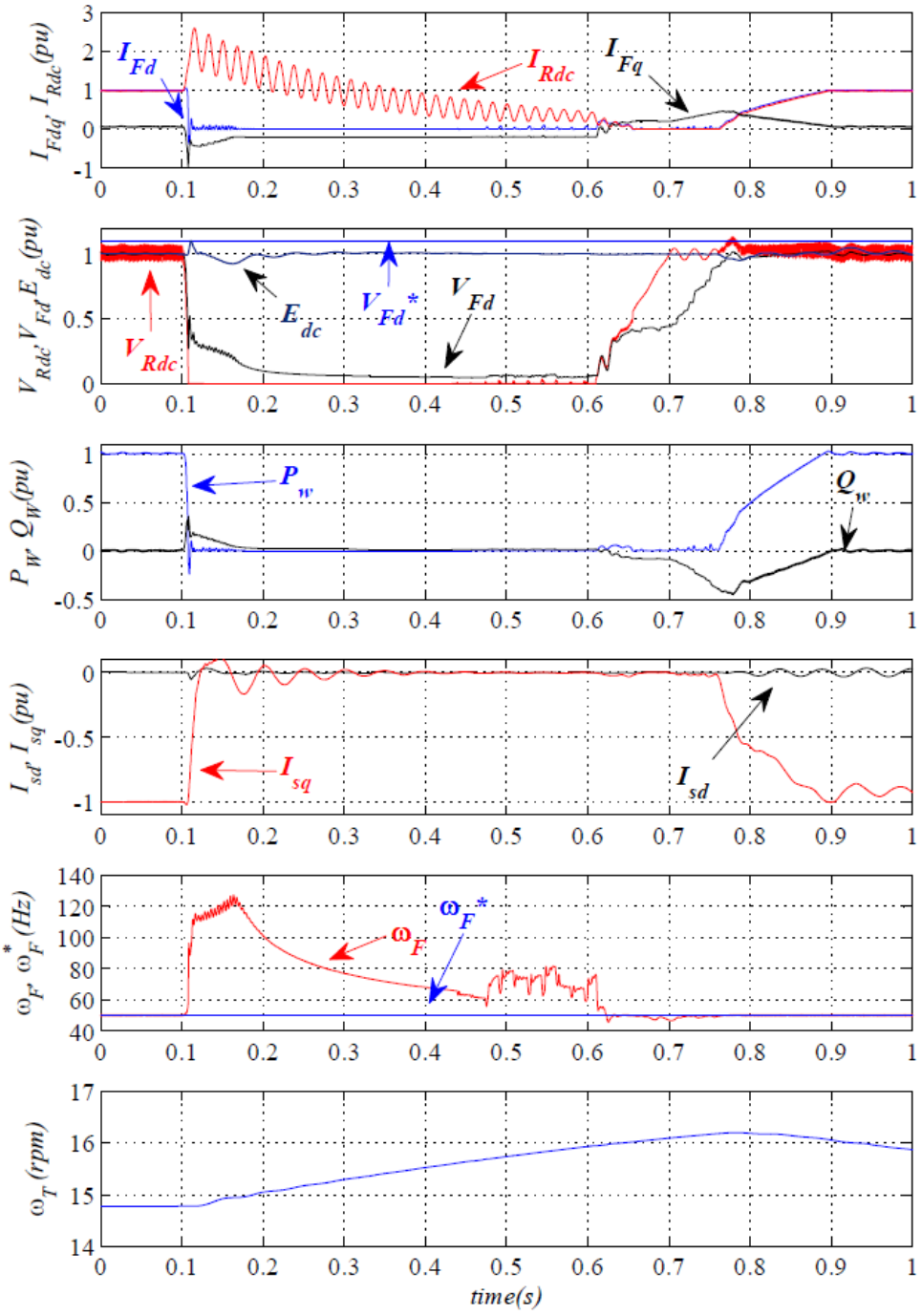

Figure 4.37: Response to a three phase fault at onshore inverter terminals

Note the present analytical study is also valid for HVdc link short circuits at the dc-inverter terminals when voltage source converters (VSC) are used.

It is clear, both from the transient in figure 4.37 and from equation 4.38, that the amount of time the rectifier current remains above its rated value is substantially higher than the one obtained with an offshore controlled rectifier.

At this stage, it is necessary to check if both ($\hat{I}_{Rdc}$) and ($\int I_{Rdc}^2 dt$) are within the operational limits of existing diodes and thyristors. For calculation simplicity, it is assumed that:

$$I_{Rdc} = I_{Rdc\infty} + \left(\hat{I}_{Rdc} - I_{Rdc\infty}\right) e^{-\frac{R}{2L}t} \tag{4.140}$$

Therefore

$$\int_0^T I_{Rdc}^2 dt = I_{Rdc\infty}^2 T + \frac{4LI_{Rdc\infty}\left(\hat{I}_{Rdc} - I_{Rdc\infty}\right)}{R} + \frac{L\left(\hat{I}_{Rdc} - I_{Rdc\infty}\right)^2}{R} \tag{4.141}$$

assuming (T) is large enough for the current to reach a new steady state current ($I_{Rdc\infty}$). With $T = 0.4$ s, $\hat{I}_{Rdc} = 5$ kA and $I_{Rdc\infty} = 0$ kA, we have $\int I_{Rdc}^2 dt = 5.99\text{x}10^6$ $\text{A}^2\,\text{s}$.

Both ($\hat{I}_{Rdc}$) and $\int I_{Rdc}^2 dt$ are within the operational limits of current high power diodes and thyristors. For example, high power thyristors of 6 kV / 2.5 kA have instantaneous maximum currents of more than 35 kA and values of $\int I_{Rdc}^2 dt$ in excess of $9\text{x}10^6$ $\text{A}^2\,\text{s}$.

Therefore, the proposed control system allows for the power electronic devices to remain within their operational limits during solid three-phase on-shore faults at inverter terminals. The system resumes operation at rated power 200 ms after the fault has been cleared. Note the duration of the fault has been deliberately extended, so, the natural discharge of the HVdc link can be appreciated.

The VDCOL protection system brings the offshore ac-voltage to a very low value during the fault. Therefore, the wind turbines should be able to continue their operation in the presence of low (V_F) voltages.

During the transient, the proposed control strategy keeps currents (I_F) and (I_G) within safe bounds. Moreover, (E_{DC}) overvoltage is kept below 1.1 pu by using

dynamic braking. Additionally, wind turbine speed is limited by means of standard pitch control, reaching a maximum of 16.3 rpm. These characteristics contribute to the wind turbine required low voltage ride-through performance.

Figure 4.38 shows the behavior of the system to a 0.8 pu voltage sag of 100 ms duration at the onshore inverter terminals. In this case, the behavior of the system is different from the one shown in figure 4.37, as the control system is capable of keeping (I_{Rdc}) below 2 pu while reducing it to 0.2 pu in less than 50 ms.

It is worth noticing that (I_{Fq}) reaches its limit during the transient. Therefore, the offshore grid frequency is no longer controlled and frequencies of up to 125 Hz are observed. However, these frequencies correspond mainly to the highly distorted voltages with low amplitudes that appear at the onset of the transient. After approximately 75 ms the frequency control loop is no longer saturated and the frequency returns rapidly to 50 Hz.

At the onset of the transient, the power delivered by the wind farm (P_{Wn}) becomes negative, implying an in-flowing power to the wind turbine converters. The in-flowing power would then create a momentary increase in the wind turbine DC link voltage (E_{DC}). As the energy absorbed by the wind turbine is small, standard protection schemes based on dynamic braking are sufficient to keep (E_{DC}) within reasonable bounds.

The overall transient, including restoration of rated power delivery lasts for around 350 ms, which is comparable to the one obtained with thyristor controlled rectifiers.

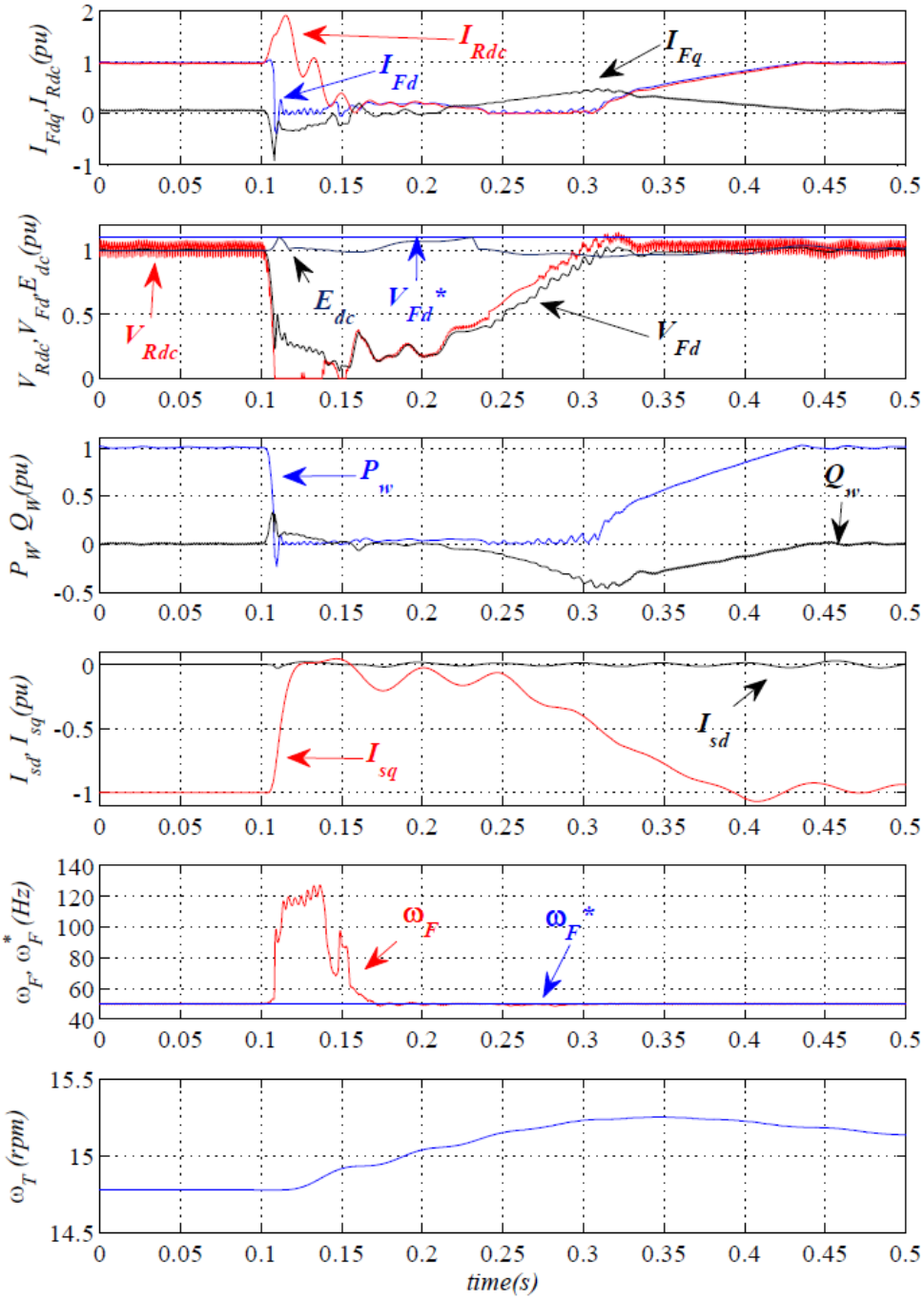

Figure 4.38: Response to a 0.8 pu voltage sag at onshore inverter terminals

4.5.5 Voltage and frequency control during rectifier ac-breaker operation

Some of the previously reported offshore frequency and voltage control strategies use the HVdc rectifier firing angle or the HVdc current (I_{Rdc}) as control actions [41]. However, these control actions are no longer available after the rectifier ac-breaker has tripped. In this situation, control of the offshore grid might be lost and power transmission would not be restored at breaker reclosure. Figure 4.39 shows the behavior of the proposed control system when the rectifier ac-breaker is opened at t = 0.1 s and reclosed after 200 ms. When the breaker trips, (I_{Fd}) drops to a value close to zero, and the voltage control loop shown in figure 4.16 is not longer saturated. Therefore the offshore grid voltage is controlled to its 1.1 pu reference. Note the 1.3 pu peak of (V_{Fd}) during 15 ms has to be within the design ratings of the wind turbine converters.

When the breaker is reclosed, power transmission is resumed in less than 40 ms. Note the (I_{Fd}) reference has not been ramped up, as in the previous cases, giving rise to the voltage and current oscillations seen in figure 16 after reconnection.

During the transient, the wind turbine dc-link voltage (E_{DC}) is again kept below 1.1 pu by means of dynamic braking. After the ac-breaker reclosure (E_{DC}) exhibits marked oscillations at the resonant frequency of the wind turbine two mass mechanical model. These oscillations could be mitigated by an enhanced design of the (E_{DC}) control loop or simply by using a rate limit on (I_{Fd}).

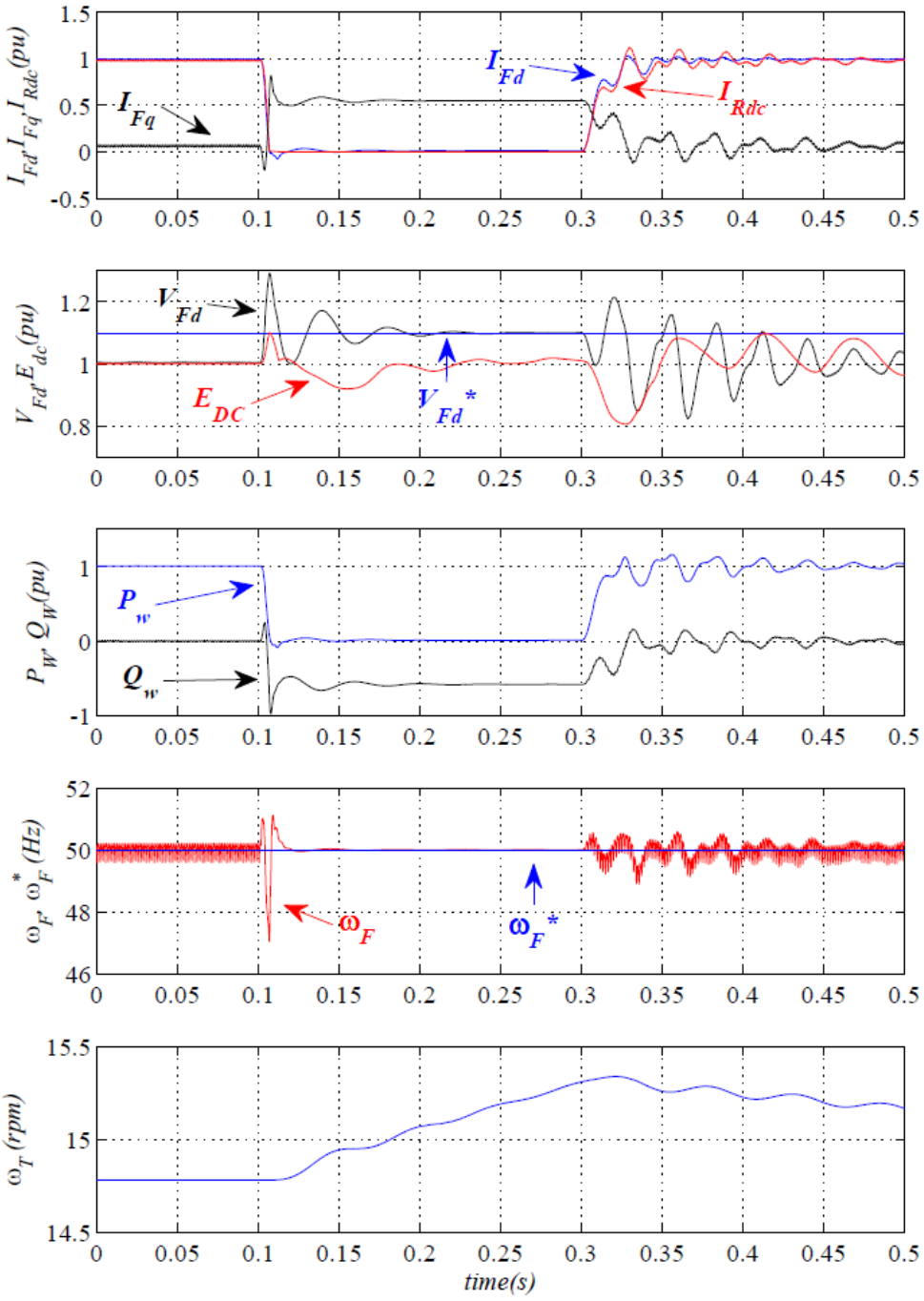

Figure 4.39: Response to operation of the diode rectifier ac-breaker

4.6 Summary

In this chapter all the wind turbines have been aggregated into a single equivalent machine. The characteristics of the rotor, the generator and the back-end converter are the same than in an individual wind turbine model. However, the front-end converter has been scaled to produce the equivalent power of the entire wind farm.

Moreover, the power generated has been delivered to the onshore grid by means of an HVdc transmission system based on diode rectifiers. Consequently, the control strategy of the wind turbine has been divided into three tasks.

The first task involves the rotor speed regulation. This task uses a scheduled controller by means of blade pitch angle variations. The strategy has shown the capability of being used to follow the optimal power tracking and besides, avoiding the wind turbine from overspeeding.

The second task corresponds to the (E_{DC}) voltage regulation. In this task the back-to-back dc-link has been set by using the back-end converter. Additionally, a chopper resistance has been included to protect the dc-link from overvoltages. As the adequate voltage regulation has been guaranteed, it has been possible to consider constant the value of the (E_{DC}). Therefore, the dynamics of the back-to-back converter have been decoupled into back-end converter dynamics and front-end converter dynamics.

The last task is related to the integration of the wind turbine to the offshore ac-grid. In this task it has been contemplated an islanded mode of operation and a connected mode of operation. In islanded mode of operation and during the transition to connected mode, the front-end converter has been employed to set the voltage and frequency of the offshore ac-grid. But, in connected mode of operation the voltage of the offshore ac-grid is clamped by the HVdc inverter. Therefore the front-end converter has been employed to set the power (P and Q) delivered to the offshore ac-grid.

In addition, a system stability analysis has been carried out for both connected and islanded operation. In this analysis different values of (C_F) and (ω_F) have been used to represent the parametric uncertainty due to both, filter bank switching and frequency flickers. As a result, the analysis of the poles location has shown the robustness of

the controller against variations of (C_F) and (ω_F). Finally, the last section of this chapter has described clearly the performed procedures and the obtained results.
In the following chapter a distributed control of the offshore wind farm will be implemented. A clustered model of the entire offshore wind farm will be used to describe the system dynamics. According to this model the power dynamics will be evaluated taking into account the mutual interaction between wind turbines. Additionally, these coupled dynamics will be considered not only during steady state but also in transient functioning. Finally, the chapter will include a stability analysis of the proposed control strategies and their corresponding validations by means of PSCAD simulations.

CHAPTER 5

Distributed Control of the Offshore Wind Farm

5.1 Introduction

In the previous chapter the control of the proposed offshore wind farm was carried out by using its aggregated model. In addition, it has been demonstrated that the control strategies used on a single model equivalent of the offshore wind farm allow delivering adequately the power to the onshore grid. Nevertheless, the aggregated model is not able to describe the mutual interaction between wind turbines during steady state and transient operation. Hence, this chapter will be focused on the study of the behavior of multiple wind turbines feeding a point of common coupling (PCC) in connected and islanded mode of operation.

Figure 5.1 shows how the proposed offshore wind farm is represented according to the cluster model defined before in section 2.3.3. Wherein, (n) wind turbines are lumped in (m) groups in order to define a cluster model equivalent of the offshore wind farm. In this model the dynamics of the rotor can be considered slower with respect to the power dynamics. This is due to the fact that rotor dynamics fluctuate within a time frame in seconds, whereas the power dynamics fluctuations are in milliseconds. As a consequence the rotor dynamics can be neglected because their dynamics are considered more than ten times slower than power dynamics.

Moreover, it is assumed an adequate control of the dc-link voltage associated to the j^{th} cluster, therefore the dynamics of the rotor, the generator and the back-end power converter are represented as a constant value (E_{DCj}).

It is important to remark that the main goal of this chapter is to extend the strategies used to control the aggregated model to the distributed case. Therefore, the following sections will describe the distributed control strategy used to perform the grid integration of the (m) wind turbine cluster models belonging to the offshore wind farm.

The proposed strategies will be implemented and validated by using PSCAD^{TM}. Additionally, the typical grid disturbances have been applied to the system in order to evaluate not only an adequate power sharing, but also, the impact on the power system dynamics.

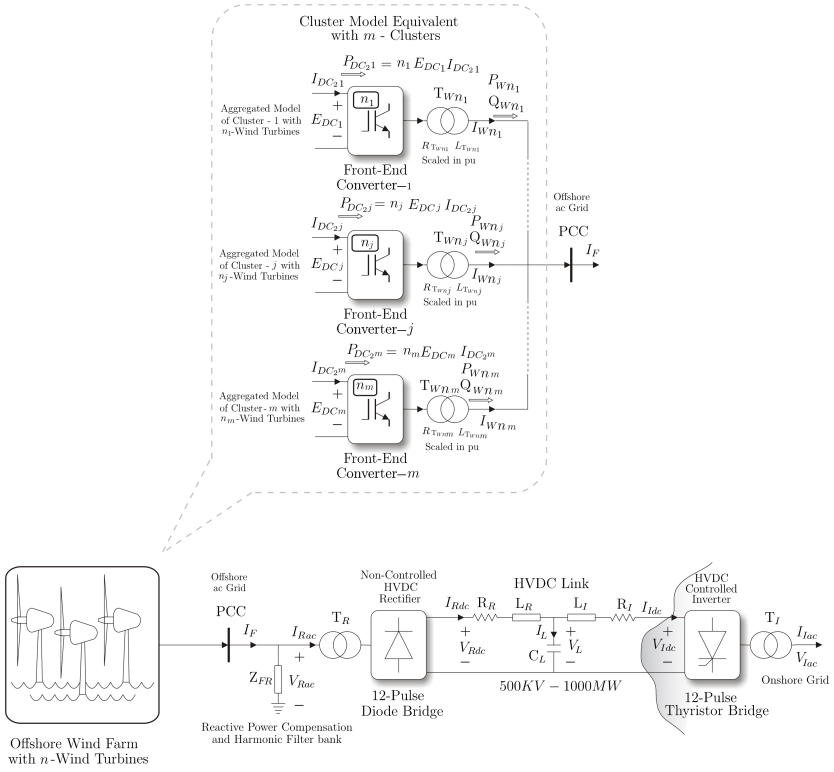

Figure 5.1: Cluster model of the offshore wind farm with n-wind turbines

5.2 Grid Integration of the j^{th} cluster

Starting from the techniques used to control the aggregated model of the offshore wind farm, it is possible to define a distributed control for the cluster model of the offshore wind farm shown in figure 5.1. As in the aggregated model, the same simplifying assumptions will be used for each cluster, i.e. the dc-link value will be considered as a constant valued (E_{DCj}), the offshore ac-line impedance will be considered negligible with respect to the wind turbine transformer leakage impedance and last, the transformer shunt branches will be not considered. Additionally, the same operational modes defined in Chapter 3 will govern the behavior of the offshore ac-grid.

Regarding to the above mentioned considerations, the proposed offshore wind farm is modelled as a total of five clusters of different power rating. The total power considered is 1 GW and each cluster corresponds to the aggregated model of multiple 5 MW wind turbines. Table 5.1 shows the considered clusters, their respective power rating and the number of wind turbines considered by each cluster model.

Table 5.1: Clusters belonging to the considered offshore wind farm

Cluster	N^o of Wind Turbines	Rated Power (MVA)
1	78	390
2	60	300
3	40	200
4	20	100
5	2	10

5.2.1 Current control of the j^{th} cluster model

The analysis of each cluster model is exactly the same analysis carried out for the aggregated model. This is because the cluster model is in turn an aggregated model with less wind turbines. The following set of equations can be derived from the five cluster model connected to the grid.

$$\frac{d}{dt}I_{Wdj} = -\frac{R_{T_{Wnj}}}{L_{T_{Wnj}}}I_{Wdj} + \omega_F I_{Wqj} + \frac{1}{L_{T_{Wnj}}}V_{Wdj} - \frac{1}{L_{T_{Wnj}}}V_{Fd} \tag{5.1}$$

$$\frac{d}{dt}I_{Wqj} = -\omega_F I_{Wdj} - \frac{R_{T_{Wnj}}}{L_{T_{Wnj}}}I_{Wqj} + \frac{1}{L_{T_{Wnj}}}V_{Wqj} \tag{5.2}$$

Wherein, the equations correspond to the j^{th} cluster model, besides all the variables are referred to the secondary side of the transformer ($\mathrm{T_{W}}nj$) and moreover (ω_F) is the instantaneous frequency of the voltage (V_F).

By analyzing separately the current equations of each cluster model it is possible to perform the current control loops likewise that was made in Chapter 4 with the aggregated model of the offshore wind farm. Figure 5.2 shows the stand-alone implementation of the two PI control loops in the j^{th} cluster connected to the offshore grid.

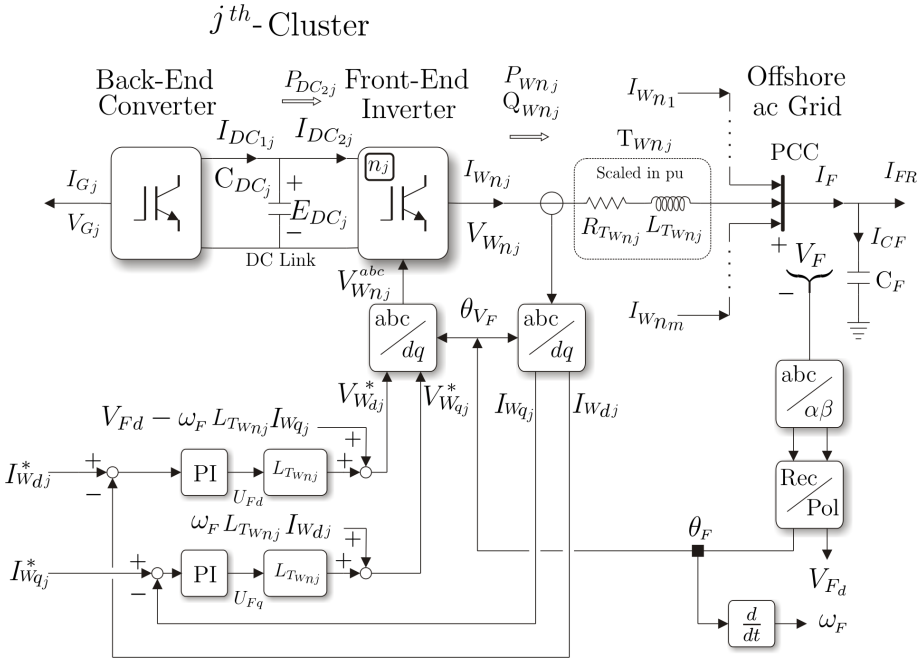

Figure 5.2: PI control loops in the j^{th} cluster connected to the offshore grid

The characteristics of the transformers corresponding to the five cluster models considered are shown in table 5.2. Besides, the values shown in table 5.3 correspond to

the parameters of the PI controllers. Due to the fact that the transformer characteristics are scaled in (pu), the resulting parameters of the PI controllers are identical for all the clusters used to model the offshore wind farm. These values have been obtained assuming the same constraints imposed before for the aggregated model, i.e. a damping ration greater than 0.707 ($DR > 0.707$) and a settling time less than 2ms ($ST < 2\text{x}10^{-3}$ s).

Table 5.2: Characteristics of the scaled transformers

Parameter	Units	Value				
Transformer	(-)	$\text{T}_{\text{W}n1}$	$\text{T}_{\text{W}n2}$	$\text{T}_{\text{W}n3}$	$\text{T}_{\text{W}n4}$	$\text{T}_{\text{W}n5}$
Rated Power	(MVA)	390	300	200	100	10
Rated Frequency	(Hz)	50	50	50	50	50
Winding 1	(kV L-L rms)	20	20	20	20	20
Winding 2	(kV L-L rms)	13.6	13.6	13.6	13.6	13.6
$R_{T_{Wn}}$ (0.005 pu)	(Ω)	1.526	1.984	2.976	5.951	59.513
$L_{T_{Wn}}$ (0.06 pu)	(mH)	58.28	75.774	113.66	227.32	2273.21

Table 5.3: PI controller parameters for the control of currents (I_{Wdj}) and (I_{Wqj})

Parameter	Value
K_{Pdj}	33.83
T_{Idj}	$3.5476\text{x}10^{-5}s$
K_{Pqj}	33.83
T_{Iqj}	$3.5476\text{x}10^{-5}s$

Assuming sufficiently fast dynamics in the aforementioned current control loops, the currents generated by the j^{th} cluster will follow their references, i.e. $I_{Wdj} = I^*_{Wdj}$ and $I_{Wqj} = I^*_{Wqj}$. Therefore, the dynamics of the offshore ac-voltage (V_{Fd}) and the frequency (ω_F) can be expressed as:

$$\frac{d}{dt}V_{Fd} = \frac{1}{C_F}\sum_{k=1}^{m} I^*_{Wdk} - \frac{1}{C_F}I_{FRd} \tag{5.3}$$

$$\omega_F V_{Fd} = \frac{1}{C_F}\sum_{k=1}^{m} I^*_{Wqk} - \frac{1}{C_F}I_{FRq} \tag{5.4}$$

It is important to remark that these expressions are only valid if the current loops are significantly faster than the voltage dynamics defined in equations 5.3 and 5.4. Therefore, as well as it was defined before in Section 4.3.1, the overall active current of the offshore wind farm cluster model ($\sum_{k=1}^{m} I^*_{Wdk}$) can be used to control the offshore ac-grid voltage (V_{Fd}), whereas the overall reactive current ($\sum_{k=1}^{m} I^*_{Wqk}$) can control the frequency (ω_F). As well as it was highlighted before, this is the opposite to the technique commonly used in power systems, where the active power is used to control the frequency and the reactive power to control the voltage. However, in our case, the grid topology and load (capacitor and filter bank) characteristics are well known, and their dynamics determine the coupling between ($\sum_{k=1}^{m} P_{Wnk}$), ($\sum_{k=1}^{m} Q_{Wnk}$), (V_{Fd}) and (ω_F).

5.2.2 Distributed voltage and frequency control

The distributed control of the offshore ac-grid voltage and frequency follows the same philosophy used to control the aggregated model. In addition, the protection strategies, the fault ride through capability and the self start capability can be guaranteed by using the same control schemes explained before in sections 4.3.2 to 4.3.4. However, in contrast to the aggregated model in the cluster model the overall power generated is split in (m) power sources. Therefore, it is necessary to define a coefficient of participation of each cluster according to its rated power. This coefficient of participation will be defined for each cluster as:

$$K_{DM_j} = \frac{\text{Rated power of the } j^{th} \text{ cluster}}{\text{Overall power of the offshore wind farm}} \quad \text{wherein} \sum_{j=1}^{m} K_{DM_j} = 1 \tag{5.5}$$

The following sections show how the control defined for the aggregated model is modified by including the coefficients of participation (K_{DM}) in the voltage and frequency

control loops.

Distributed control of the offshore ac-grid voltage

In section 4.3.2 the procedure to calculate the offshore ac-voltage controller for the aggregated model has been defined. But, the offshore ac-voltage dynamics is now defined by the equation 5.3 and therefore the currents of each cluster defined in the model shall be contemplated.

The plant to be controlled represents an integrator; hence, it can be easily controlled with the same PI controller defined in table 4.8. However, the voltage control loop requires a remote measurement of (I_{FRd}) as a compensation term. Due to the fact that this term is not available in practice, it must be estimated by using local variables. Therefore the estimation errors shall be corrected with the integral part of the controller. For this reason the controller proposal is defined with the proportional part of the controller placed in each cluster model and the integral part common to all cluster models.

The main idea is to calculate the controller in the same manner than the controller calculated for the aggregated model and then, split the control action according to the coefficient of participation of each cluster. This can be carried out multiplying the output of each control loop with remote integrator by the constant (K_{DM}) proportional to the rated power of each cluster. Thus, it is possible not only, to actuate with the proportional part of the controller as a traditional droop controller, but also to correct the steady state error with the centralized integrator. Figure 5.3 shows the proposed voltage control loops for the j^{th} cluster connected to the offshore ac-grid. Notice that, the control schema of the j^{th} cluster corresponds to a distributed control wherein the part enclosed in the dotted line is an integral part centralized, i.e. common to the complete wind farm.

Just as with the aggregated model, the voltage control loop will be functioning only in islanded operation and during the transition between islanded and connected mode. However, during connected operation the HVdc diode rectifier will act as a voltage clamp on (V_{Fd}) and the clusters will be operating in current control mode. Therefore, the different voltage control loops will be saturated and the j^{th} cluster will

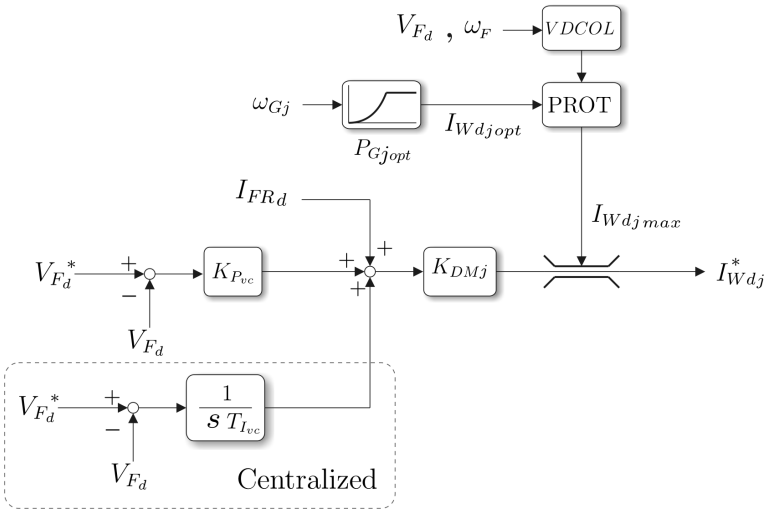

Figure 5.3: Offshore ac grid voltage control

inject a current ($I_{Wdj} = I_{Wdj\,\max}$) determined by both, the wind turbine optimal characteristic [44] and the protections defined before in sections 4.3.2 to 4.3.4, i.e. $I_{Wdj\,\max} = \min\left(\sqrt{|I_{Wnj}|^2_{\max} - I^2_{Wqj}}\ ,\ I_{Wdj\mathrm{opt}}\right)$ wherein $|I_{Wnj}|_{\max}$ is defined by the VDCOL protection characteristic according to figure 4.15. Moreover, once the distributed controller shown in figure 5.3 is no longer saturated, the offshore ac-grid voltage (V_{Fd}) will turn back again to be set by the aforementioned voltage control loop.

Notice that, the required remote measurement of (I_{FRd}) can be avoided either by not using the feed-forward term, with the corresponding performance degradation, or by estimating (I_{FRd}) from local variables.

Distributed control of the offshore ac-grid frequency

As previously mentioned, equation 5.4 implies that the clusters connected to the offshore ac-grid can use their reactive currents to control the offshore ac-grid frequency. However, in order to perform the distributed frequency control it is necessary that each cluster injects a current (I^*_{Wqj}) proportional to its rated power, i.e. $I^*_{Wqj} = K_{DM_j} I^*_{Fq}$. Wherein, $I^*_{Fq} = \sum_{k=1}^{m} I^*_{Wqk}$, and ($K_{DM_j}$) defined by the equation 5.5 as the coefficient

of participation of the j^{th} cluster.

Equation 5.4 is just an algebraic equation that could be used to perform the open control loop of the offshore frequency. But in the same manner as with the aggregated model, it can be improved by using an estimated value of (I_{FRq}) to close the control loop. This estimated value $(\hat{I}_{FRq})$ is calculated by including just local measurement. Additionally, the procedure to obtain this value was explained in section 4.3.3. Therefore, by using a similar procedure, it is possible to use the local values of the j^{th} cluster in order to define the following expression:

$$\hat{I}_{FRq} = \frac{1}{3K_{DM_j}} \frac{V_{Wqj}P_{Wnj} - V_{Wdj}Q_{Wnj}}{V_{Wdj}^2 + V_{Wqj}^2} - C_F\omega_F V_{Fd} \tag{5.6}$$

Using the equation 5.4 and substituting (I_{FRq}) by its estimated value $(\hat{I}_{FRq})$, the following relationship can be defined:

$$I_{Fq}^* = C_F V_{Fd}\left(\omega_F^* - \omega_F\right) + \frac{1}{3K_{DM_j}} \frac{V_{Wqj}P_{Wnj} - V_{Wdj}Q_{Wnj}}{V_{Wdj}^2 + V_{Wqj}^2} \tag{5.7}$$

This expression correspond to the frequency control loop of the j^{th} cluster connected to the offshore grid. Its corresponding block diagram is shown in figure 5.4.

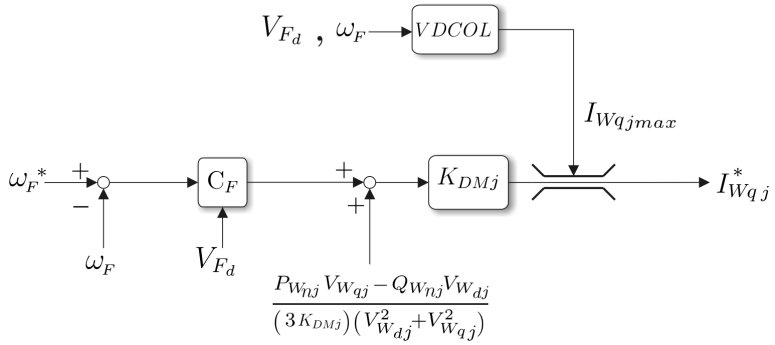

Figure 5.4: Offshore ac grid frequency control

Note that the frequency control loop corresponds to a simple proportional control with a feed-forward compensation term. Therefore, the offshore ac-grid dynamics has led to a scheme similar to traditional droop control. Additionally, the proportional contribution to set the frequency is defined according to the coefficient of participation

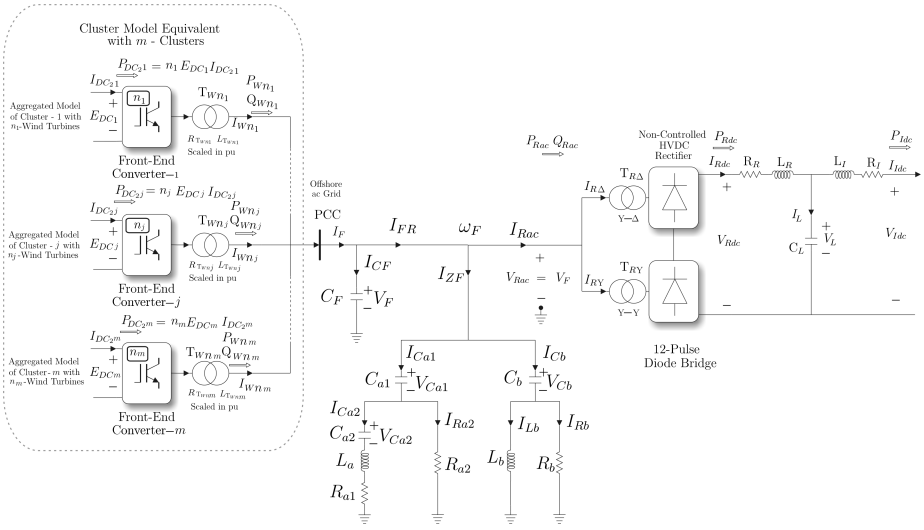

Figure 5.5: Cluster model of the offshore wind farm in connected mode

, i.e. $I^*_{Wqj} = K_{DM_j} I^*_{Fq}$. Moreover, the current injected by the cluster will be also limited by the VDCOL protection schema defined before in section 4.3.4, wherein $I_{Wqj\,\max} = |I_{Wnj}|_{\max}$.

According to this schema, it is clear that the frequency control system is more robust to C_F estimation errors. This is due to the fact that C_F now appears within the control loop and it can be considered as a loop gain, rather than a plant parameter. Besides, note that all the variables used in figure 5.4 are local to each cluster.

5.3 Stability Analysis

The stability analysis of the offshore wind farm with a distributed control will be carried out by analyzing its poles. In section 4.4 a similar analysis was carried out with the state space model of the complete offshore wind farm including all its control loops. This analysis was also carried out assuming both, connected and islanded operation. Therefore, it is clear that there is enough similarity between the analysis made on the aggregated model and the analysis that has to be made on the cluster model.

In the following sections only the more relevant changes with respect to the aggregated model analysis will be explained. Therefore, assuming that some expressions have been explained before in Chapter 4, their development will only be referenced.
Mainly, only two aspects have changed. First, the front-end converters connected to the PCC are more than one. Second, the dynamics of the offshore ac-grid will have to include all the front-end converters connected to the PCC. Hence, the state space model of the complete offshore wind farm will have to include not only, the new dynamics associated to each front-end converter, but also its new control loops.
As mentioned before, there will be considered five clusters ($m = 5$) connected to the PCC as shown in figure 5.5. This figure represents the connected operation mode and beside, the characteristics of each cluster have been shown before in table 5.1 and 5.2.
According to figure 5.5, the corresponding linearized state space model of the offshore wind farm in connected mode can be represented by the following equations:

Dynamics of the five front-end converters connected to the PCC

$$\frac{d}{dt}I_{Wd1} = -\frac{R_{T_W 11}}{L_{T_W 11}}I_{Wd1} + \omega_F I_{Wq1} + \frac{1}{L_{T_W 11}}V_{Wd1} - \frac{1}{L_{T_W 11}}V_{Fd} \tag{5.8}$$

$$\frac{d}{dt}I_{Wq1} = -\omega_F I_{Wd1} - \frac{R_{T_W 11}}{L_{T_W 11}}I_{Wq1} + \frac{1}{L_{T_W 11}}V_{Wq1} \tag{5.9}$$

$$\frac{d}{dt}I_{Wd2} = -\frac{R_{T_W 22}}{L_{T_W 22}}I_{Wd2} + \omega_F I_{Wq2} + \frac{1}{L_{T_W 22}}V_{Wd2} - \frac{1}{L_{T_W 22}}V_{Fd} \tag{5.10}$$

$$\frac{d}{dt}I_{Wq2} = -\omega_F I_{Wd2} - \frac{R_{T_W 22}}{L_{T_W 22}}I_{Wq2} + \frac{1}{L_{T_W 22}}V_{Wq2} \tag{5.11}$$

$$\frac{d}{dt}I_{Wd3} = -\frac{R_{T_W 33}}{L_{T_W 33}}I_{Wd3} + \omega_F I_{Wq3} + \frac{1}{L_{T_W 33}}V_{Wd3} - \frac{1}{L_{T_W 33}}V_{Fd} \tag{5.12}$$

$$\frac{d}{dt}I_{Wq3} = -\omega_F I_{Wd3} - \frac{R_{T_W 33}}{L_{T_W 33}}I_{Wq3} + \frac{1}{L_{T_W 33}}V_{Wq3} \tag{5.13}$$

$$\frac{d}{dt}I_{Wd4} = -\frac{R_{T_W 44}}{L_{T_W 44}}I_{Wd4} + \omega_F I_{Wq4} + \frac{1}{L_{T_W 44}}V_{Wd4} - \frac{1}{L_{T_W 44}}V_{Fd} \tag{5.14}$$

$$\frac{d}{dt}I_{Wq4} = -\omega_F I_{Wd4} - \frac{R_{T_W 44}}{L_{T_W 44}}I_{Wq4} + \frac{1}{L_{T_W 44}}V_{Wq4} \tag{5.15}$$

$$\frac{d}{dt}I_{Wd5} = -\frac{R_{T_W55}}{L_{T_W55}}I_{Wd5} + \omega_F I_{Wq5} + \frac{1}{L_{T_W55}}V_{Wd5} - \frac{1}{L_{T_W55}}V_{Fd} \tag{5.16}$$

$$\frac{d}{dt}I_{Wq5} = -\omega_F I_{Wd5} - \frac{R_{T_W55}}{L_{T_W55}}I_{Wq5} + \frac{1}{L_{T_W55}}V_{Wq5} \tag{5.17}$$

Dynamics of the offshore ac-grid voltage (V_{Fd}) and the HVdc filter bank

$$\begin{aligned}\frac{d}{dt}V_{Fd} &= \tfrac{1}{C_F}I_{Wd1} + \tfrac{1}{C_F}I_{Wd2} + \tfrac{1}{C_F}I_{Wd3} + \tfrac{1}{C_F}I_{Wd4} + \tfrac{1}{C_F}I_{Wd5} + \cdots \\ &\quad \cdots + \tfrac{1}{C_F R_{a2}}V_{Ca1d} - \tfrac{1}{C_F}I_{Lad} + \tfrac{1}{C_F R_b}V_{Cbd} - \tfrac{1}{C_F}I_{Lbd} + \cdots \\ &\quad \cdots - \tfrac{B\sqrt{6}NV_{Fd_0} - 2B\omega_F L_{T_R} I_{Rdc_0}}{\pi C_F K_{Dloss} V_{Fd_0}} I_{Rdc} - \left[\tfrac{B\omega_F L_{T_R} I_{Rdc_0}^2}{\pi C_F K_{Dloss} V_{Fd_0}^2} + \tfrac{R_{a2}+R_b}{C_F R_{a2} R_b}\right] V_{Fd}\end{aligned} \tag{5.18}$$

$$\frac{d}{dt}V_{Ca1d} = -\tfrac{1}{R_{a2}C_{a1}}V_{Ca1d} + \omega_F V_{Ca1q} + \tfrac{1}{C_{a1}}I_{Lad} + \tfrac{1}{R_{a2}C_{a1}}V_{Fd} \tag{5.19}$$

$$\frac{d}{dt}V_{Ca1q} = -\omega_F V_{Ca1d} - \tfrac{1}{R_{a2}C_{a1}}V_{Ca1q} + \tfrac{1}{C_{a1}}I_{Laq} \tag{5.20}$$

$$\frac{d}{dt}V_{Ca2d} = \omega_F V_{Ca2q} + \tfrac{1}{C_{a2}}I_{Lad} \tag{5.21}$$

$$\frac{d}{dt}V_{Ca2q} = -\omega_F V_{Ca2d} + \tfrac{1}{C_{a2}}I_{Laq} \tag{5.22}$$

$$\frac{d}{dt}I_{Lad} = -\tfrac{1}{L_a}V_{Ca1d} - \tfrac{1}{L_a}V_{Ca2d} - \tfrac{R_{a1}}{L_a}I_{Lad} + \omega_F I_{Laq} + \tfrac{1}{L_a}V_{Fd} \tag{5.23}$$

$$\frac{d}{dt}I_{Laq} = -\tfrac{1}{L_a}V_{Ca1q} - \tfrac{1}{L_a}V_{Ca2q} - \omega_F I_{Lad} - \tfrac{R_{a1}}{L_a}I_{Laq} \tag{5.24}$$

$$\frac{d}{dt}V_{Cbd} = -\tfrac{1}{R_b C_b}V_{Cbd} + \omega_F V_{Cbq} + \tfrac{1}{C_b}I_{Lbd} + \tfrac{1}{R_b C_b}V_{Fd} \tag{5.25}$$

$$\frac{d}{dt}V_{Cbq} = -\omega_F V_{Cbd} - \tfrac{1}{R_b C_b}V_{Cbq} + \tfrac{1}{C_b}I_{Lbq} \tag{5.26}$$

$$\frac{d}{dt}I_{Lbd} = -\tfrac{1}{L_b}V_{Cbd} + \omega_F I_{Lbq} + \tfrac{1}{L_b}V_{Fd} \tag{5.27}$$

$$\frac{d}{dt}I_{Lbq} = -\tfrac{1}{L_b}V_{Cbq} - \omega_F I_{Lbd} \tag{5.28}$$

Dynamics of the HVdc link

$$\frac{d}{dt}I_{Rdc} = \left[-\tfrac{R_R}{L_R} - \tfrac{3BL_{T_R}}{\pi L_R}\omega_F\right] I_{Rdc} + \tfrac{3NB\sqrt{6}}{\pi L_R}V_{Fd} - \tfrac{1}{L_R}V_L \tag{5.29}$$

$$\frac{d}{dt}I_{Idc} = -\tfrac{R_I}{L_I}I_{Rdc} - \tfrac{1}{L_I}V_{Idc} + \tfrac{1}{L_I}V_L \tag{5.30}$$

$$\frac{d}{dt}V_L = \tfrac{1}{C_L}I_{Rdc} - \tfrac{1}{C_L}I_{Idc} \tag{5.31}$$

It is worth noticing that in islanded mode the HVdc link is not conducting. Hence, this mode of operation can be represented by the equivalent circuit shown in figure 5.6, wherein $I_{Rdc} = 0$.

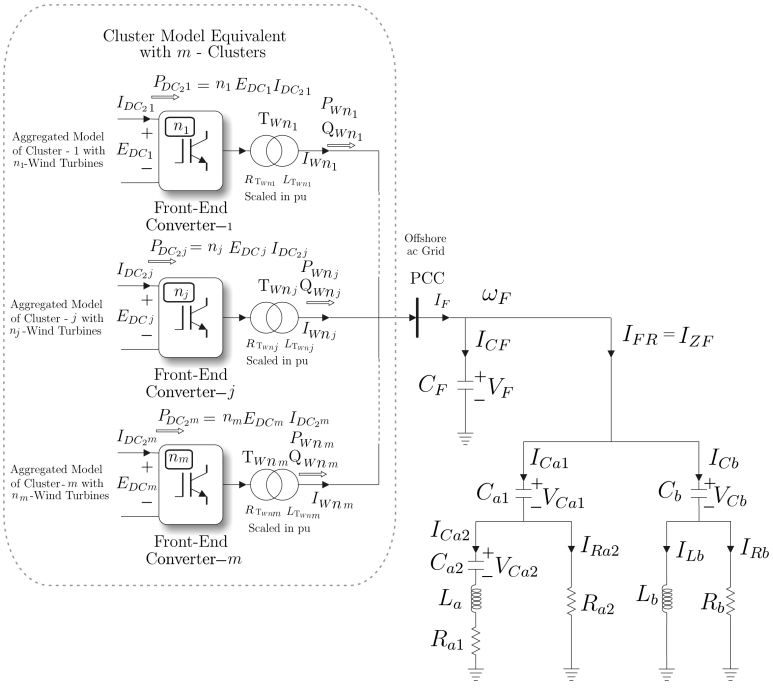

Figure 5.6: Cluster model of the offshore wind farm in islanded mode

After eliminate equations 5.29, 5.30 and 5.31, the abovementioned set of equations can be also used to represent the linearized state space model of the offshore wind farm in islanded mode.

Moreover, a similar procedure as the used before in section 4.4 to include the current controller and the voltage controller is carried out to include the control loops of the five clusters connected to the PCC.

Note that the voltage control loop requires a remote measurement of (I_{FRd}) that is considered as external perturbation during the stability analysis. This is due to the fact that, during connected operation the value of (I_{FRd}) can be considered similar to (I_{Rdc}); and during islanded operation its value tends to zero.

The parameters of the current and voltage controller are shown in table 5.3 and 4.8 respectively. The rest of the necessary parameters used to calculate the eigenvalues of the closed loop system have been defined before in tables 4.9 and 4.10.

Eigenvalues in connected operation mode

In connected operation mode the system can operate in both, current control mode and voltage control mode. Hence, the system stability in connected mode will be carried out analyzing the eigenvalues location of the system defined by equations 5.8 to 5.31 and their corresponding control loops.

As in the stability analysis of the aggregated model, the eigenvalues will be calculated in presence of variations of (C_F) and (ω_F). Figure 5.7 shows path of the eigenvalues when (C_F) varies from 0.856 μF to 4.856 μF. In this case, the system is being operated in current control mode. Notice that the zoom of the region closer to the inestability region is shown in figure 5.8. According to figure 5.7 and 5.8, it is possible to see that variations of (C_F) affect only to a pair of poles that have weak influence on the system dynamics.

Similarly, figure 5.9 shows path of the eigenvalues when (ω_F) varies from 125.66 rad/ s to 628.32 rad/ s. Additionally, the zoom of the region closer to the inestability region is also shown in figure 5.10. In contrast to figure 5.8, large variations of (ω_F) affect severely the system damping.

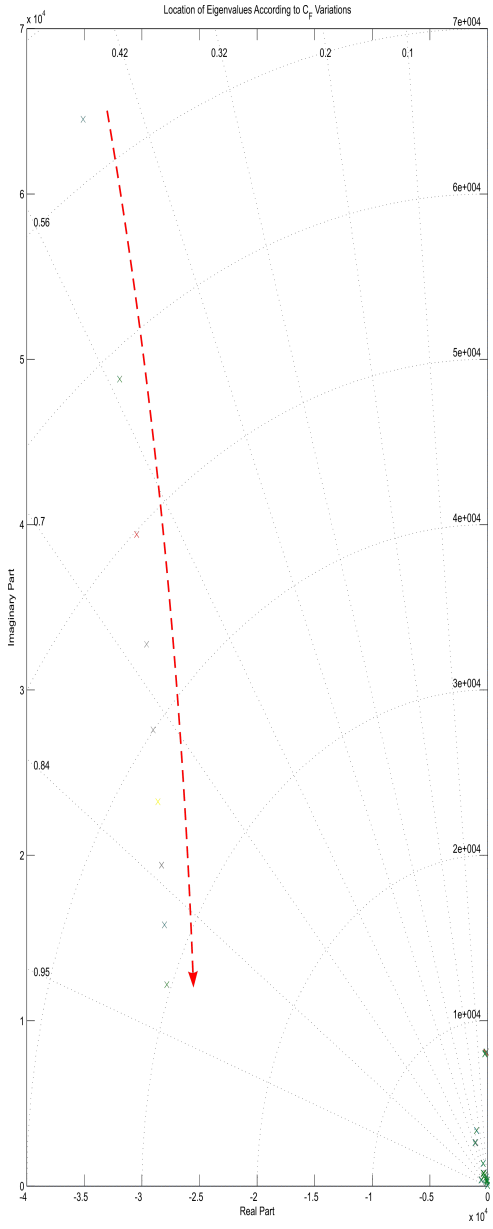

Figure 5.7: Eigenvalues in current control mode and variable (C_F) - Connected operation

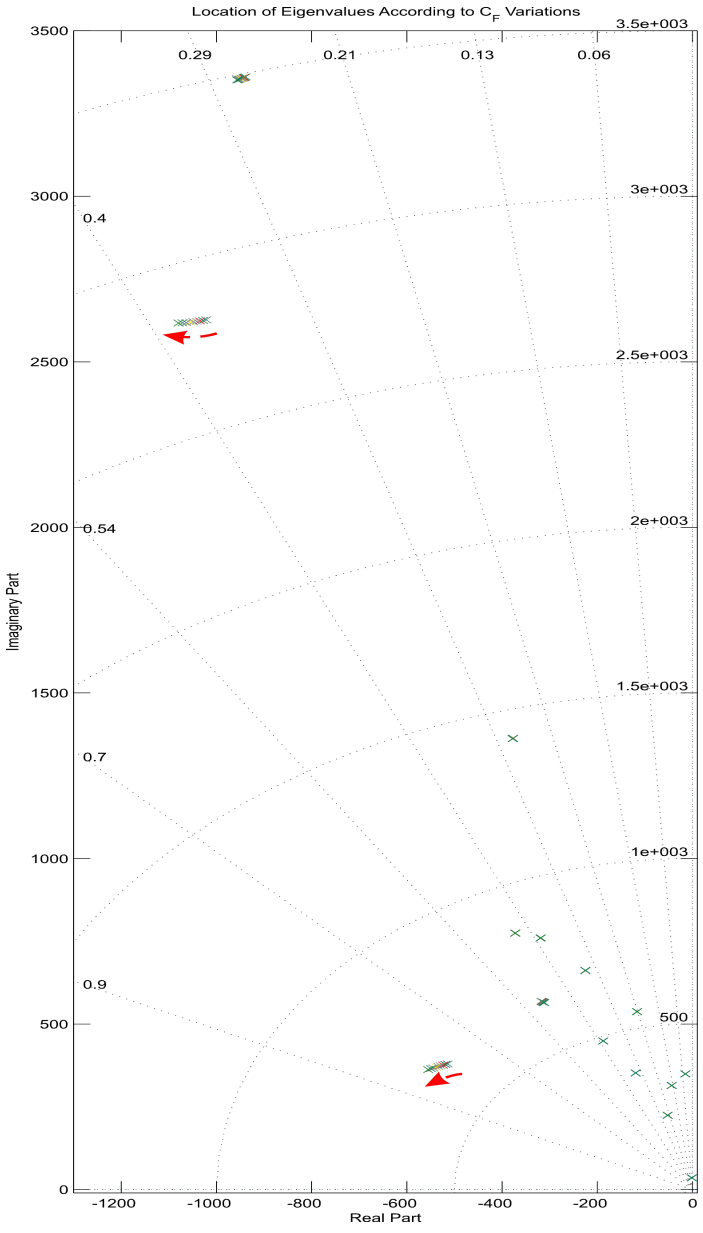

Figure 5.8: Zoom of the eigenvalues in current control mode and variable (C_F) - Connected operation

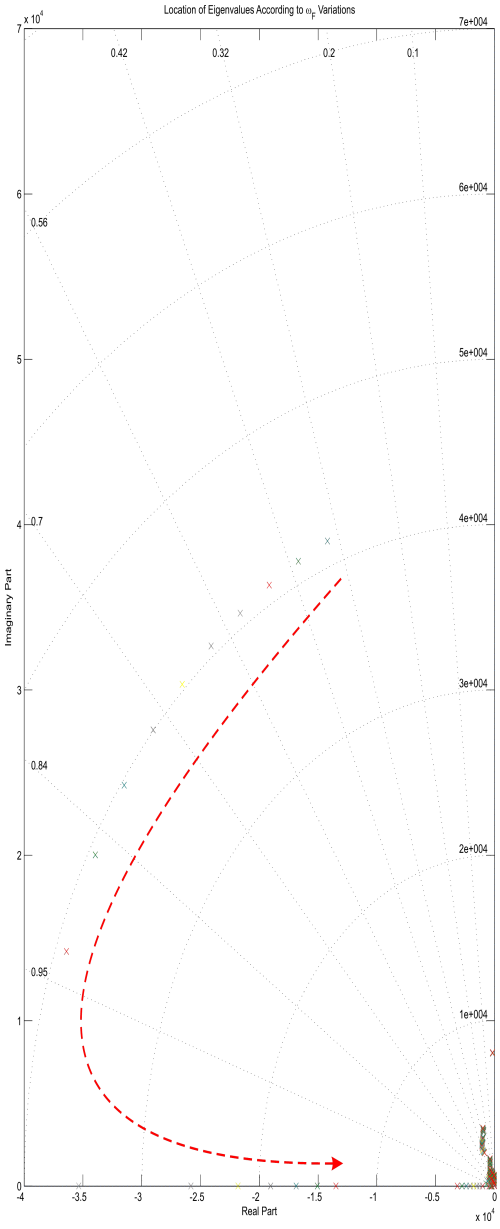

Figure 5.9: Eigenvalues in current control mode and variable (ω_F) - Connected operation

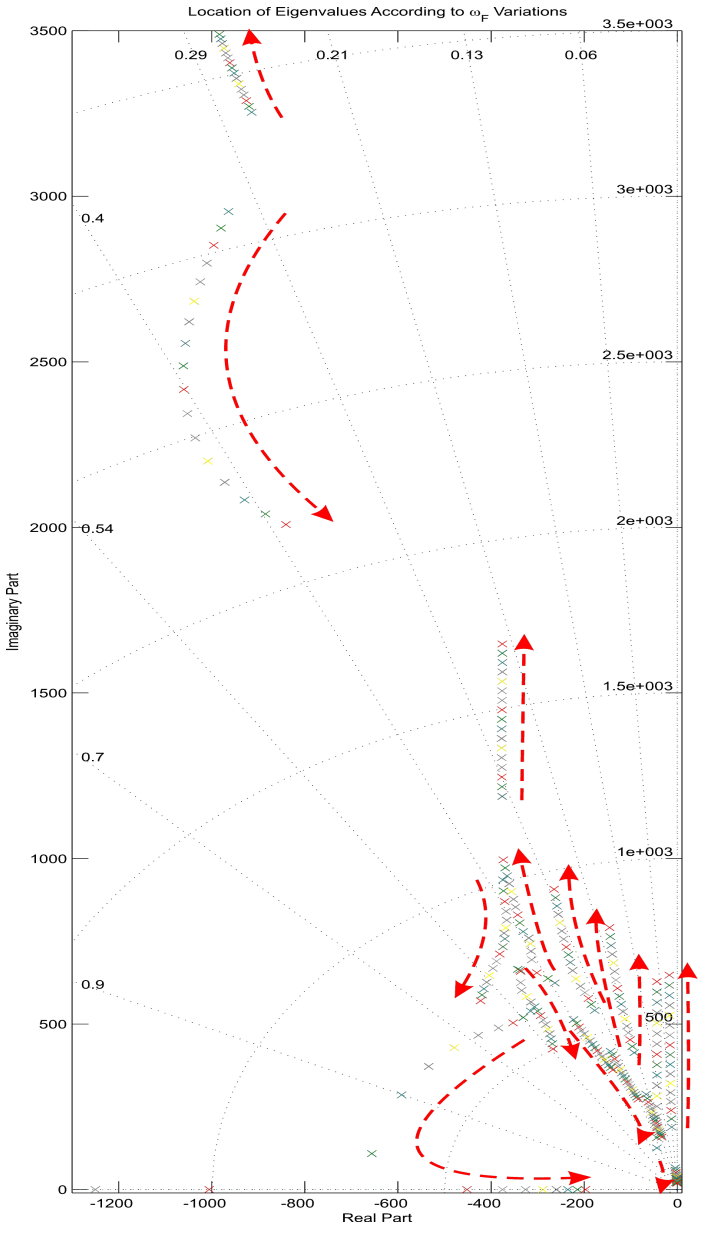

Figure 5.10: Zoom of the Eigenvalues in current control mode and variable (ω_F) - Connected operation

Moreover, during voltage control mode, the analysis will have to include not only the dynamics of the current controllers, but also the voltage controller dynamics. Again (C_F) varies from 0.856 μF to 4.856 μF and the eigenvalues are shown in figure 5.11. Notice that the zoom of the region closer to the inestability region is shown in figure 5.12.

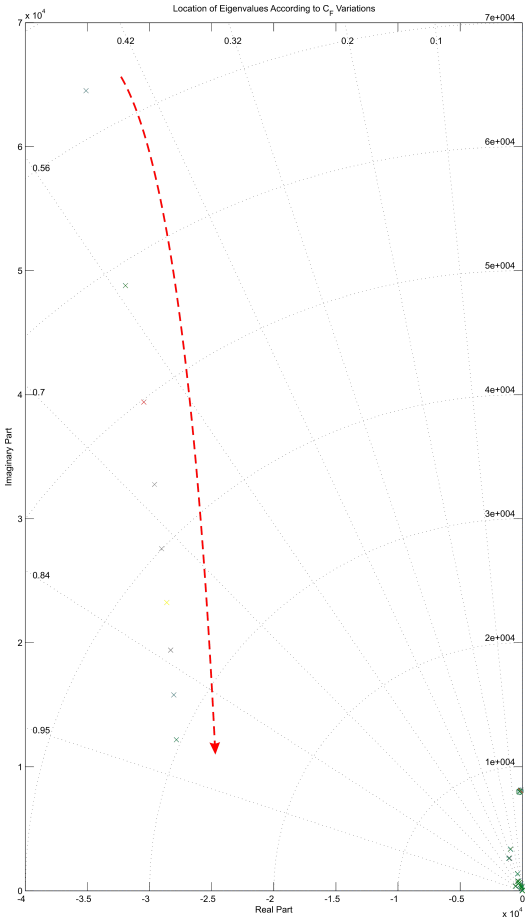

Figure 5.11: Eigenvalues in voltage control mode and variable (C_F) - Connected operation

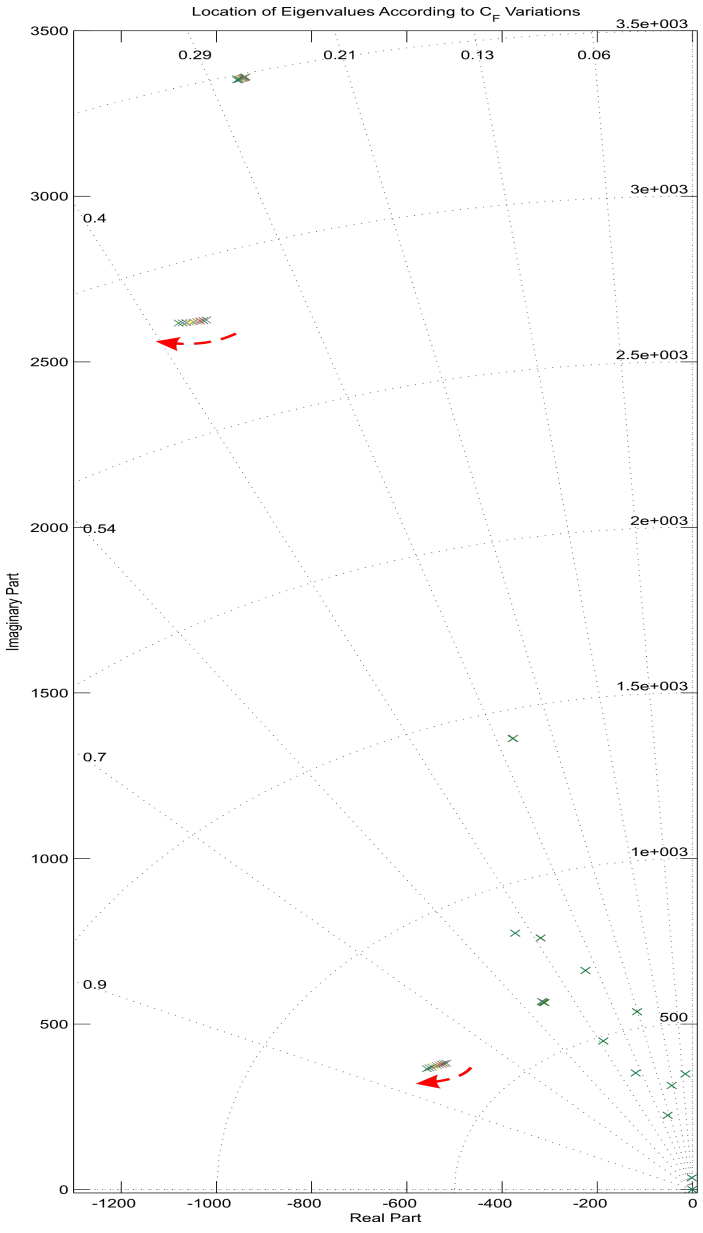

Figure 5.12: Zoom of the eigenvalues in voltage control mode and variable (C_F) - Connected operation

Similarly, figure 5.13 shows path of the eigenvalues when (ω_F) is varying from 125.66 rad/ s to 628.32 rad/ s. Additionally, the zoom of the region closer to the inestability region is also shown in figure 5.14.

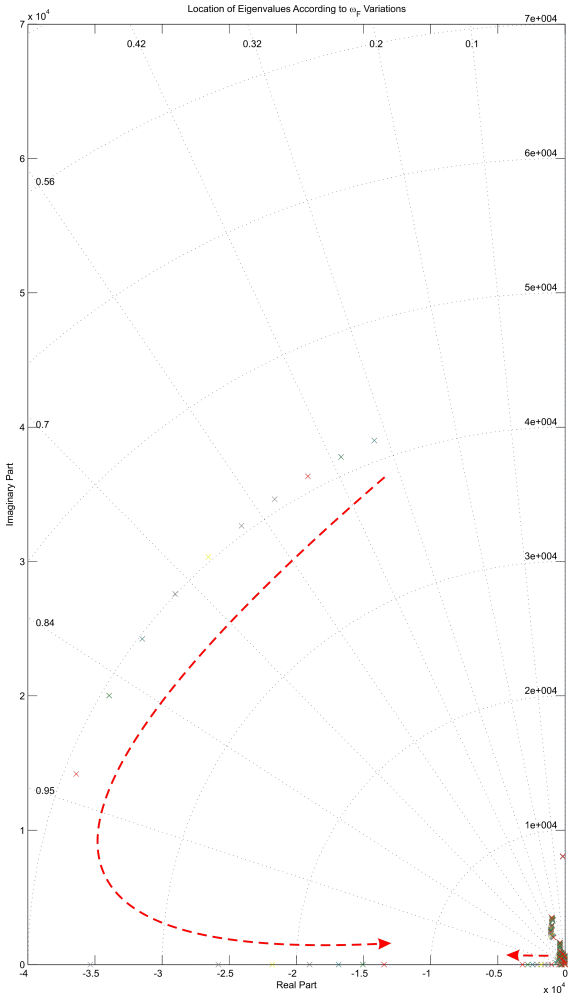

Figure 5.13: Eigenvalues in voltage control mode and variable (ω_F) - Connected operation

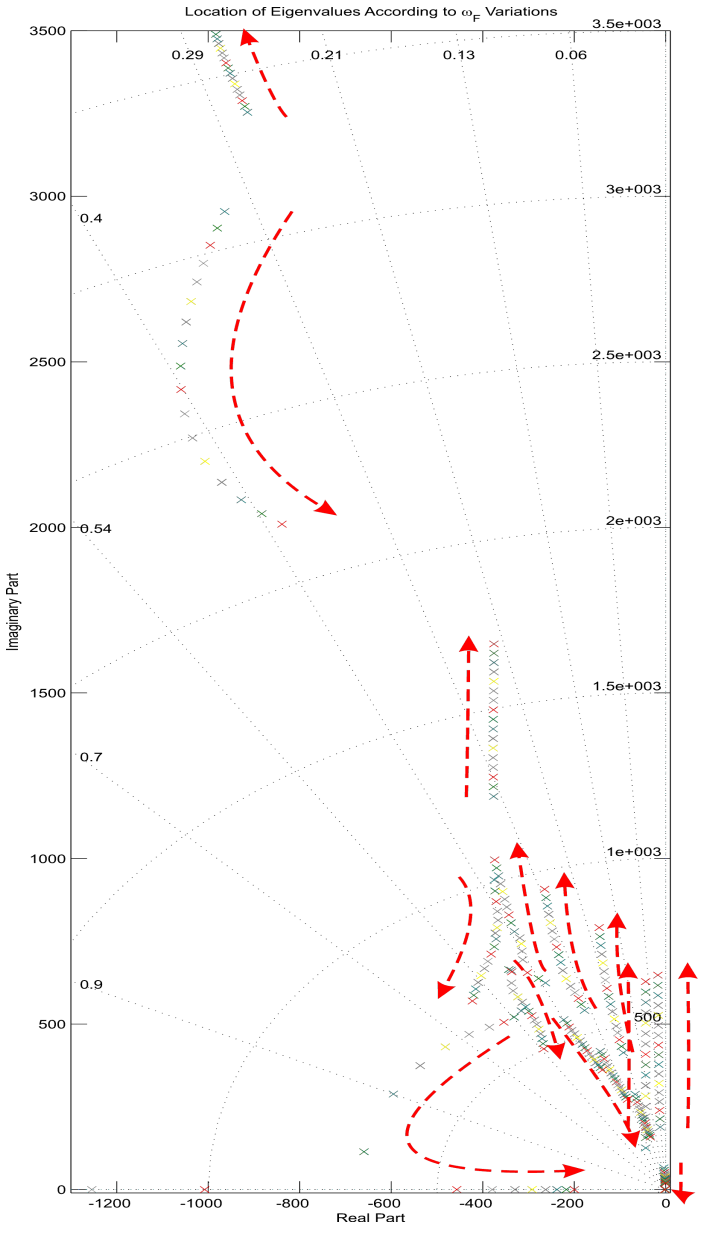

Figure 5.14: Zoom of the eigenvalues in voltage control mode and variable (ω_F) - Connected operation

Eigenvalues in islanded operation mode

During islanded mode of operation, the system works only in voltage control mode. Therefore, the analysis will have to include not only the dynamics of the current controllers, but also the voltage controller dynamics. The value of (C_F) varies from $0.856\,\mu$F to $4.856\,\mu$F and its corresponding eigenvalues are shown in figure 5.15. Notice that the zoom of the region closer to the inestability region is shown in figure 5.16. According to these figures it is clear that variations of (C_F) only affect the location of the poles that have less influence on the system dynamics.

Similarly, figure 5.17 shows path of the eigenvalues when (ω_F) is varies from $125.66\,\mathrm{rad/s}$ to $628.32\,\mathrm{rad/s}$. Additionally, the zoom of the region closer to the inestability region is also shown in figure 5.18. As can be seen in these figures, when there are variations of (C_F) and (ω_F), the system remains in stable conditions. Notice that, as in connected mode these variations of (ω_F) affect negatively the system damping.

In this operation mode the system dynamics have been simplified (the HVdc link has not been included). As a consequence, the offshore ac-grid dynamics start to be dominated by the capacitor and filter bank. In contrast to connected mode, during this mode the wind turbines will have to change the traditional (P/f) and (Q/V) strategies in order to control adequately the offshore ac-grid voltage and frequency.

Moreover, according to figures 5.12, 5.14, 5.16 and 5.18, it is clear that the eigenvalues show smaller position variation during islanded operation than during connected operation for a similar range of (C_F) and (ω_F) variation.

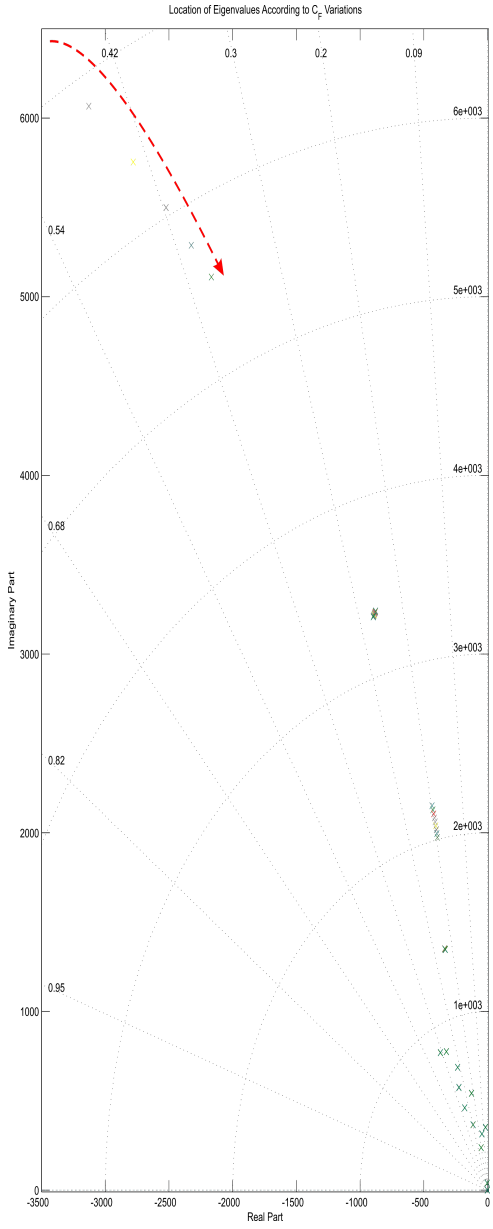

Figure 5.15: Eigenvalues in current control mode and variable (C_F) - Islanded operation

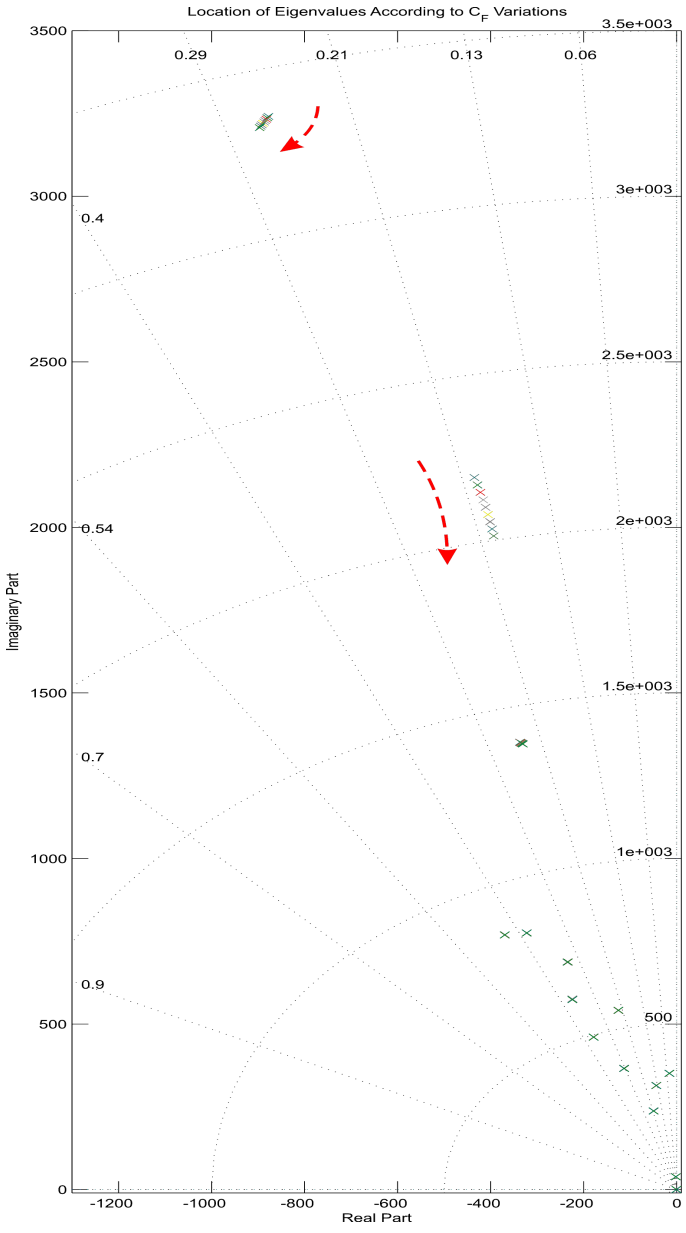

Figure 5.16: Zoom of the eigenvalues in current control mode and variable (C_F) - Islanded operation

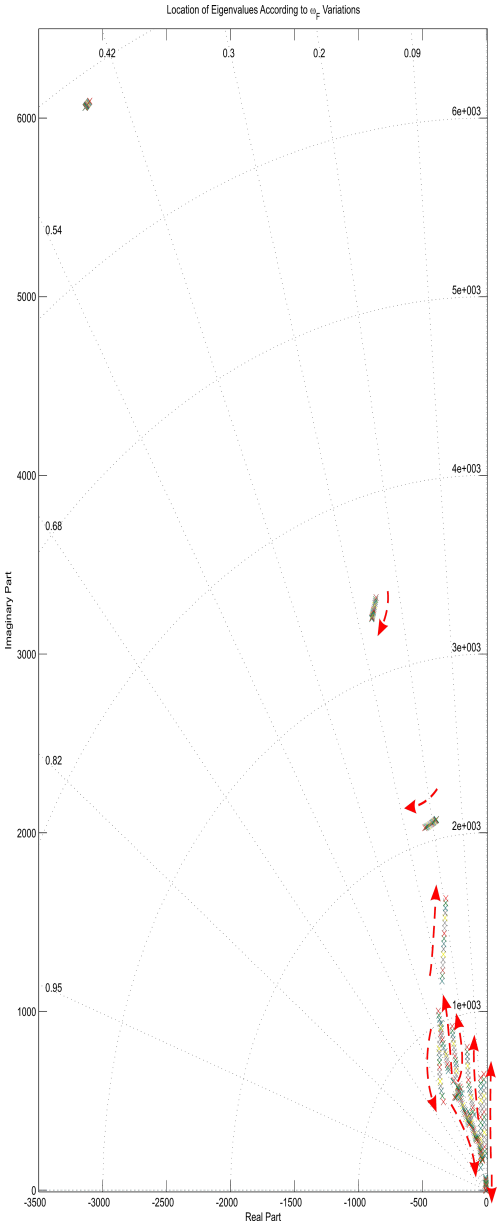

Figure 5.17: Eigenvalues in current control mode and variable (ω_F) - Islanded operation

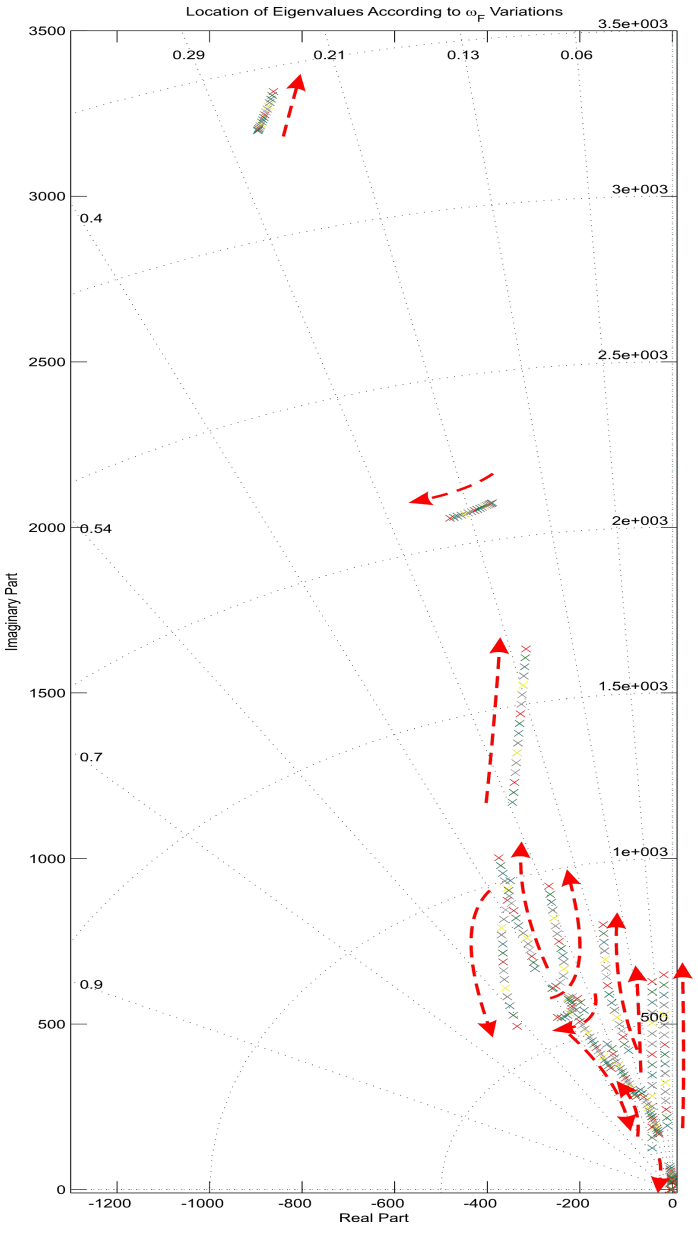

Figure 5.18: Zoom of the eigenvalues in current control mode and variable (ω_F) - Islanded operation

5.4 Results

The control strategies previously described have been validated using PSCAD™ simulations. Several scenarios have been considered to check voltage and frequency control during islanded operation, adequate start-up procedure, response to power generation variations and response during different transient conditions (on-shore faults, generation disconnection, HVdc rectifier ac-breaker tripping and reconnection and capacitor bank switching). The parameters of the HVdc link have been obtained from the CIGRE benchmark model [39], using a diode rectifier instead of a thyristor rectifier and modelling the onshore inverter station by the means of a variable voltage dc-source [41, 40]. The wind farm has been modelled using a total of five equivalent cluster models that in the following will be considered as wind turbines of different rated power. The rated power of each cluster has been defined in table 5.1. Additionally, the coefficient of participation was defined before by equation 5.5, being the overall power of the offshore wind farm also the base power for the whole system, i.e. $S_{RT} = 1000\text{MVA}$.

A switching frequency of 1kHz has been assumed for the wind turbine front-end converters. Therefore, the front-end converter current loop bandwidth has been designed to be around 180Hz. The offshore ac-grid voltage control loop is designed to have a 20 Hz closed loop bandwidth, therefore, communication delays on the centralized integrator in the range of 5-10ms can be easily tolerated.

5.4.1 Islanded operation (operation mode A)

The performance of the proposed voltage and frequency control systems has been initially tested with the offshore grid operating in islanded mode, i.e. the HVdc diode rectifier is not conducting. Figure 5.19 shows the response of the proposed control system to load changes and to frequency reference changes during islanded operation. Initially, the offshore grid is operated at no-load and rated voltage and frequency.

At $t = 0.1s$, a 0.5 pu resistive load is connected. After a transient lasting approximately 40ms, the system returns to the steady state, showing an excellent sharing of active and reactive power amongst the different turbines. At $t = 1s$, the resistive

load is disconnected. The minimum voltage during load connection is 0.85pu and the maximum voltage during load disconnection is 1.15 pu. Note the sudden connection and disconnection of a 500MW local load on the offshore grid represents an extreme scenario, unlikely to happen in an actual system. Nevertheless the good response to such a load variation proves the good voltage regulation and load sharing capability of the proposed control strategy.

During the previously mentioned load transient, a frequency reference change of $\pm$2Hz is carried out in order to show the performance of the frequency control loop. The frequency reference is reached in $10ms$.

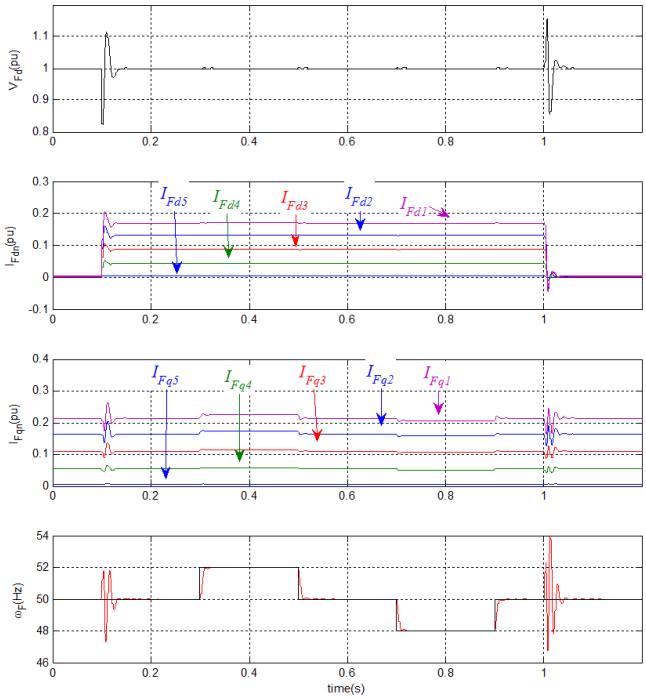

Figure 5.19: Response to load and frequency reference changes during islanded operation

Self-start operation (transition between modes A – B – C)

As shown in figure 5.2, the wind turbine front-end converter current control loops are oriented on (V_{Fd}). Therefore, when the offshore ac-grid is not operational ($V_{Fd} = 0$), an adequate start-up procedure is required for wind turbine connection.

Figure 5.20 shows the start-up transient, including the HVdc link energization. At $t = 0s$, the onshore inverter starts operating, rising the HVdc link voltage from 0 to its rated value. At $t = 0.3s$, after rated HVdc link voltage has been reached, the offshore ac-grid voltage and frequency control loops are enabled and the (V_{Fd}) demand is increased linearly from 0 to 1.1 pu. Frequency reference is kept constant at 50Hz. From $t = 0.3s$ to $t = 1.7s$, the HVdc rectifier is not conducting, and the offshore ac-grid is effectively operated in islanded mode, with a fixed frequency reference and a variable voltage reference.

Note that the reactive current components (I_{Wqj}) are relatively large when the HVdc diode rectifier is not conducting. Clearly, when the diode rectifier is not conducting, the capacitor and filter bank are overcompensating and the wind turbines must balance the excess of reactive power produced by the capacitor bank.

When (V_{Fd}) reaches a value of 0.87 pu (at $t = 1.7s$), the off shore rectifier starts conducting and currents (I_{Wdj}) and (I_{Rdc}) increase. As current (I_{Rdc}) increases, the (V_{Rdc}) ripple increases due to the higher harmonic content at higher currents. When (I_{Wdj}) reaches a value of 1 pu, the voltage control loop in fig. 5.4 saturates and the offshore ac-grid voltage (V_{Fd}) does no longer follow its reference. Therefore, figure 5.20 shows a smooth transition between voltage and current control mode of operation, as well as a smooth transition between islanded and connected operation. The ac-grid frequency (ω_F) remains close to 50 Hz during the transient.

The transient in figure 5.20 shows reliable steady state operation at rated power and stand alone operation of the wind farm with good voltage and frequency regulation when the HVdc diode rectifier is not conducting and excellent active and reactive power sharing during the complete transient. It is worth stressing that all wind turbine front-end converters are controlled as grid-forming inverters and therefore all of them contribute to the control of the offshore grid during start-up.

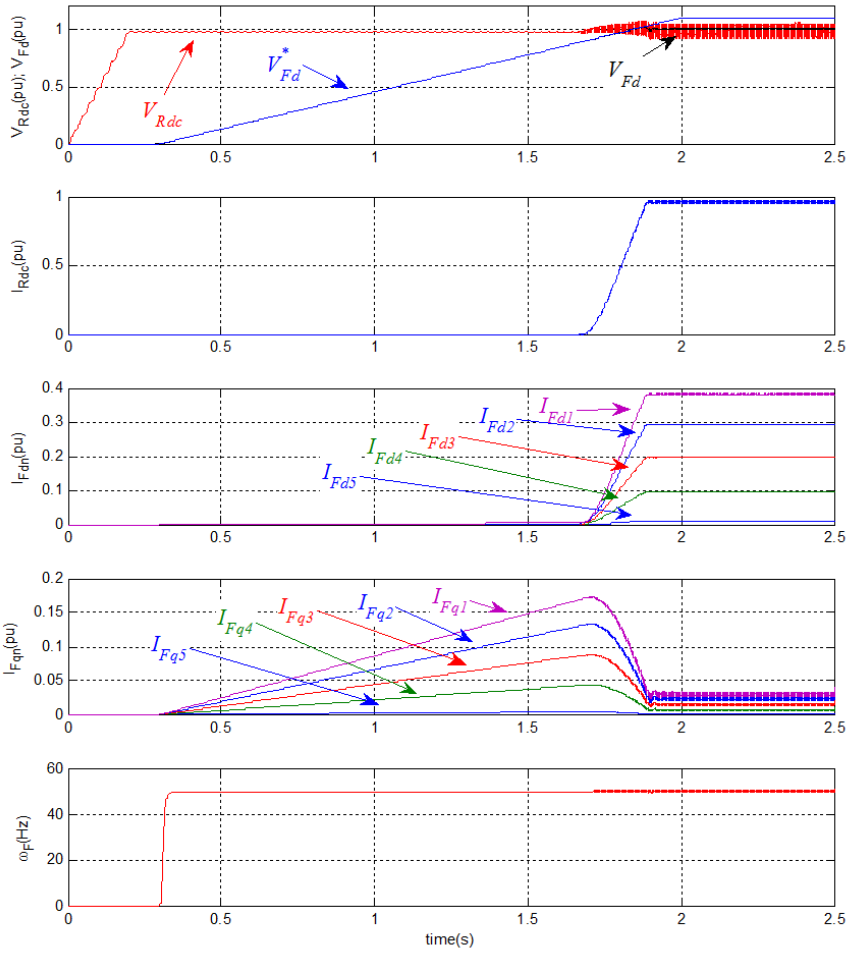

Figure 5.20: HVdc link and off-shore ac grid start-up operation

Self start operation with power limits in some wind turbines

The connection transient shown in figure 5.20 assumes that rated active power is available from all the wind turbines. However, depending on the wind conditions, wind turbines might not be able to deliver full rated active power. To consider this situation, the active power delivered by the 390MVA wind turbine is limited to 30% of its rated value. The connection of the wind farm with this active power constraint is shown in figure 5.21.

The behavior of the system is exactly the same as the unconstrained case up to 0.16s. At this point, (I_{Wd1}) saturates and stops contributing to the offshore ac-grid voltage control. Nevertheless, the rest of the wind turbines would still be keeping (V_{Fd}) very close to its reference. Notice the increase slope on (I_{Wd2}) to (I_{Wd5}) to compensate for (I_{Wd1}) saturation. At $t = 0.24$s, all the wind turbines saturate and the system can no longer track the reference value of (V^*_{Fd}).

During the transient there are no constraints on reactive power components (I_{Wqj}) and therefore reactive power is shared amongst all wind turbines. Note that, in contrast with figure 5.20, the reactive current components do not reach a zero value after the transient. This effect is caused again by the overcompensation of capacitor and filter banks when the HVdc diode rectifier is not operating at full power.

It is worth stressing that, from $t = 0.16$s to $t = 0.24$s, some of the wind turbines are controlling the ac-grid voltage, while some others are saturated due to insufficient wind resource. As seen in figure 5.21, the proposed distributed control algorithm does handle this situation automatically.

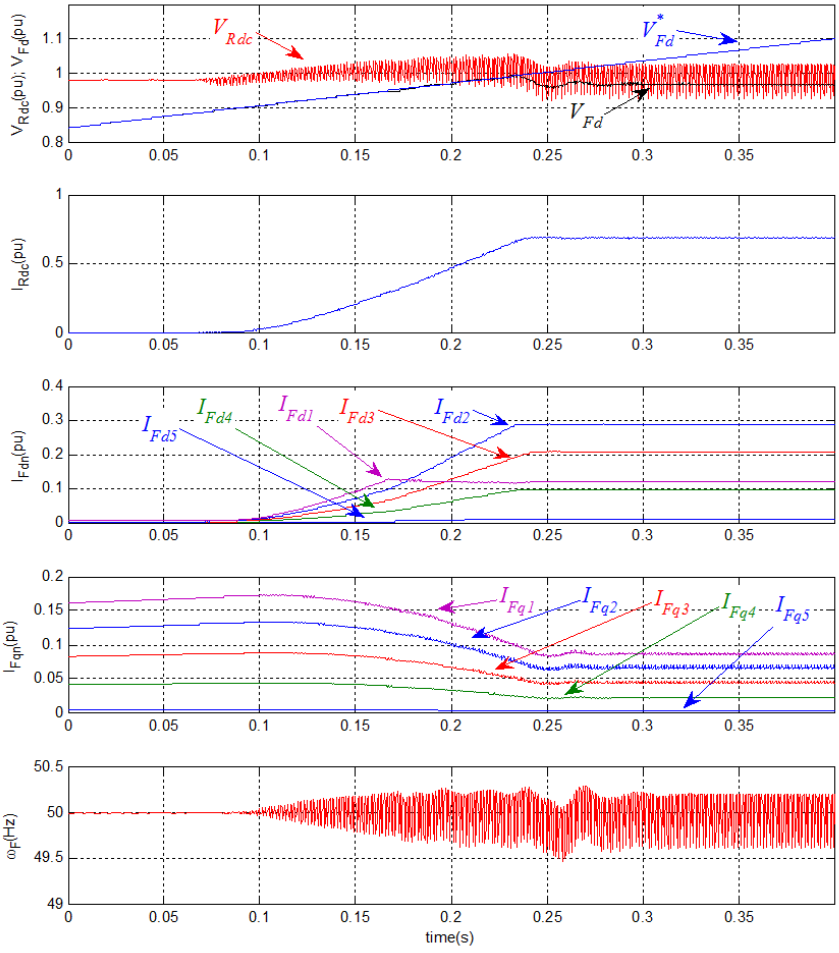

Figure 5.21: Offshore ac grid voltage ramp-up with power constraints

5.4.2 Connected operation

Frequency control

The performance of the frequency control loop is shown in figure 5.22, while the system is operating in current control mode at rated power. At $t = 0.1$s the frequency demand rises to 52 Hz (1.04 pu) and then is changed back to 50 Hz (at $t = 0.3$s). Similarly, a reduction on frequency demand (to 48Hz) is carried out at $t = 0.5$s. In both cases, the actual frequency reaches its reference value in around 12ms. The wind turbine active currents (I_{Wdj}) remain constant during the transients. On the other hand (I_{Wqj}) show minor variations, due to the frequency dependant nature of the reactive power of the capacitor bank, filters and leakage reactances.

Power tracking (MPPT)

Figure 5.23 shows the response of the system to changes in the 390MVA wind turbine power reference, i.e. $j = 1$. The value of ($I^*_{Wdj\,\max}$) in figure 5.3 has been reduced from 390 MW to 200 MW in 0.1s, kept constant for 0.2s, ramped down to 39 MW, kept constant again for 0.2s and then ramped up to 390 MW to simulate power variations for changing wind conditions. Note a 351MW power transient in 0.2 s might not be realistic, as power generated from a wind farm of this size does not vary so rapidly. Therefore, the behavior during realistic power changes would always be better than the one shown in figure 5.23.

It should be pointed out that the wind turbine front-end reactive currents (I_{Wq1} to I_{Wq5}) increase as (I_{Wd1}) decreases, as the capacitor and filter bank are again overcompensating the reactive power absorbed by the rectifier transformer leakage reactance. On the other hand, the HVdc link and offshore ac-grid voltages decrease slightly along with (I_{Wd1}) due to smaller voltage drop on the HVdc link resistance and rectifier transformer leakage reactance. During the whole transient, the frequency of the offshore ac-grid follows its reference value.

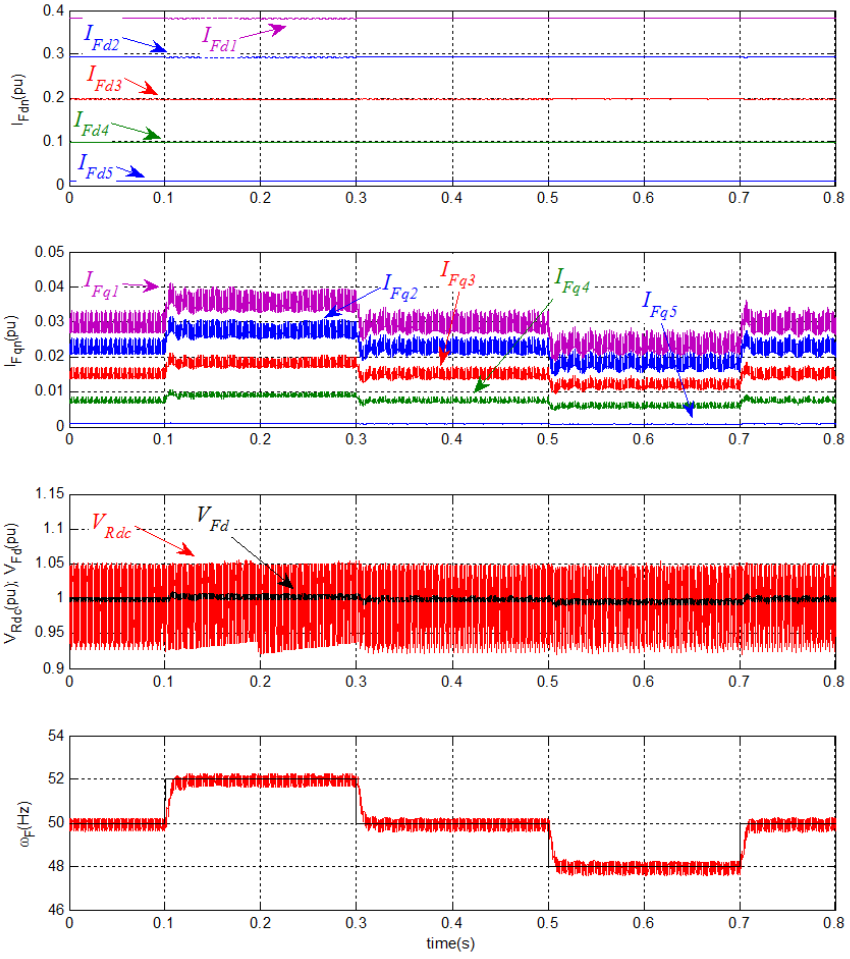

Figure 5.22: Response to frequency demand changes at rated power

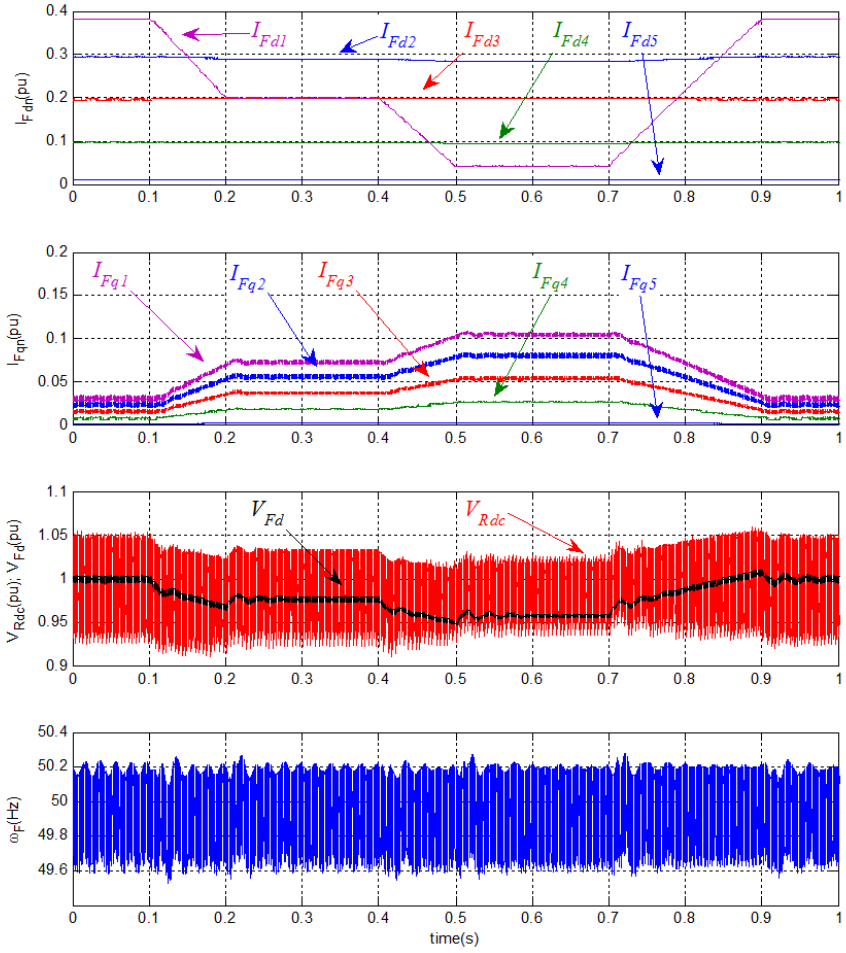

Figure 5.23: Response to changes in wind farm power set point

5.4.3 Transient performance

Capacitor bank switching

The reactive power absorbed by both the leakage inductances of the transformers and the overlap angle of the HVdc rectifier are functions of the generated power. Although, as shown in the previous figures, the wind turbine front-end converters can compensate for reactive power variations, the capacitor banks would usually be switched on and off depending on the required overall reactive power.

Figure 5.24 shows the response of the system to the connection of a 100MVA capacitor bank at $t = 0.05s$ and subsequent disconnection at $t = 0.25s$, when the system is being operated at rated power. The connection transient lasts for about $50ms$. When the capacitor bank is connected, the control system reacts by absorbing the additional reactive power generated by the capacitor bank. Note the adequate reactive power sharing amongst the different wind turbines.

During the connection transient, the offshore ac-grid voltage reaches a maximum value of 1.1pu. However, during capacitor bank disconnection, the transient is almost negligible. This difference in behavior is due to the fact that all the front-end converters are initially operating at rated current, therefore, when they are required to provide additional reactive current, the front-end current references are limited by the protections defined before in sections 4.3.2 to 4.3.4, i.e. $I_{Wdj\,\max} = \min\left(\sqrt{|I_{Wnj}|^2_{\max} - I^2_{Wqj}}\ ,\ I_{Wdj\mathrm{opt}}\right)$ and $I_{Wqj\,\max} = |I_{Wnj}|_{\max}$. Note the front-end inverter active currents are reduced to provide enough reactive current capability for the system to restore rated voltage and frequency. When the transient is over ($t = 0.1s$), rated power operation is resumed.

It is worth stressing that the controller parameters have not been modified during this transient, showing therefore, good robustness to relatively large sudden changes of the system overall capacitance.

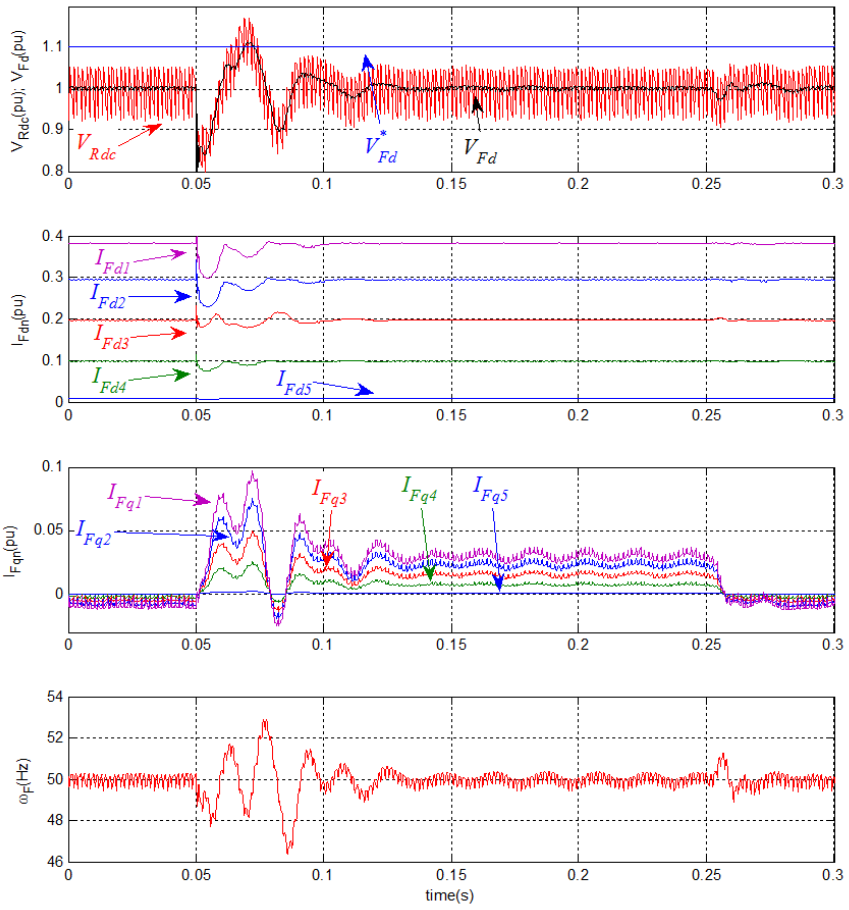

Figure 5.24: Response to the switching of a 100MVA capacitor bank

Fault ride through operation

Onshore ac-grid voltage dip (80%) Figure 5.25 shows the response of the system to an 80% voltage sag at the on-shore inverter terminals. The fault has a duration of 500 ms with a 350ms recovery time to 100% of the pre-fault voltage. As the HVdc link voltage reduces, the offshore ac-voltage (V_{Fd}) will reduce almost proportionally. This behavior is caused by the HVdc diode rectifier voltage clamp on (V_{Fd}). Therefore, the VDCOL mechanism on each independent cluster will sense the ac-grid voltage reduction and therefore the active and reactive currents limits ($I_{Wdj\,\max}$ and $I_{Wqj\,\max}$) will decrease in each cluster. When all reactive current components (I_{Wqj}) reach their saturation limits, the frequency control loop saturates and the frequency of the offshore ac-grid reaches a maximum of 120 Hz during less than 100ms. After 100 ms (I_{Wqj}) are no longer saturated and frequency control is regained. Full power delivery is resumed as the voltage (V_{Rdc}) recovers its pre-fault value. It is worth stressing that the peak HVdc link current is below 2pu, which is comparable to the values obtained with fully controlled rectifiers.

Note that the wind turbine active currents (I_{Wd1} to I_{Wd5}) are positive during the complete transient, except from few milliseconds right after the fault ($t = 0.1$s). Therefore, during this period of time, active power will flow into the wind turbine front-end converters. The maximum power flowing into the wind turbine front end converters is 60MW (0.06pu) and the negative power flow lasts for less than 3 milliseconds. Therefore, the overall energy flowing into the converters is at most 180 KJ and it could be easily absorbed by the dynamic breaking protection of the wind turbines.

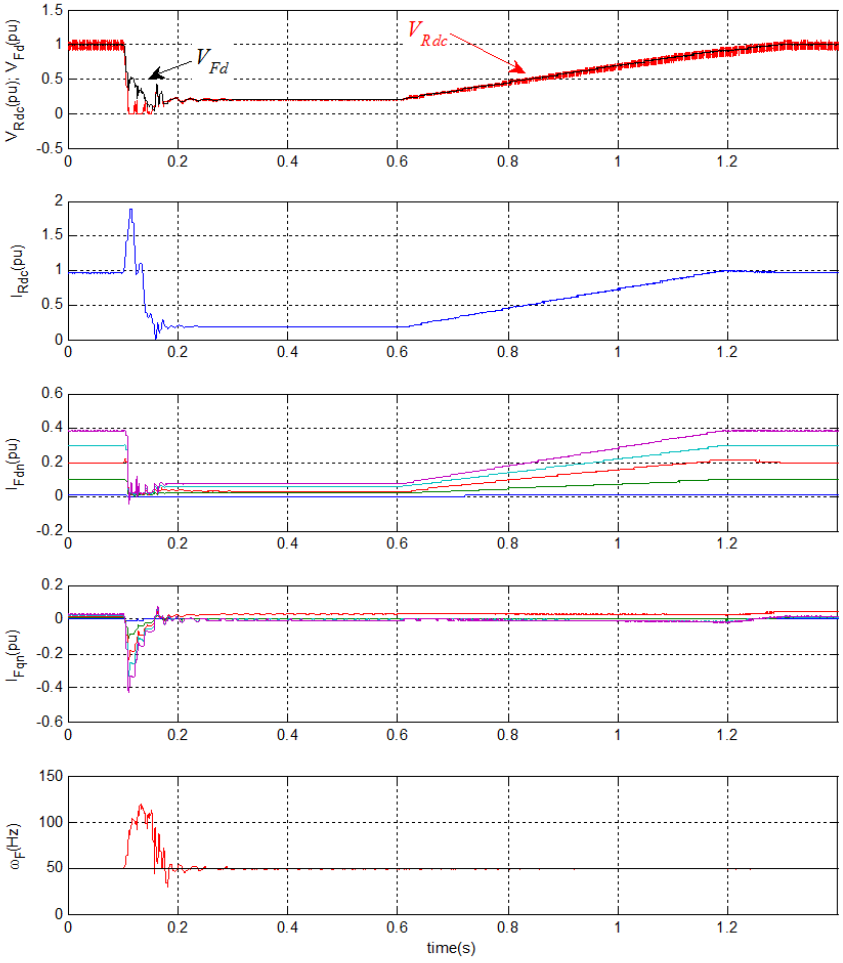

Figure 5.25: Response to an 80% voltage sag at onshore inverter terminals

Disconnection of a substantial number of wind turbines The response to a sudden disconnection of 10% of the wind turbines is shown in figure 5.26. At $t = 0.1$s wind turbine 4 (100MVA) breaker is opened. After a small transient, lasting less than 50ms, the offshore ac-grid voltage and current return to their reference values, while the HVdc current (I_{Rdc}) reflects the 10% reduction in generating power. Again, the remaining wind turbines have to provide the reactive power required to keep the offshore ac-grid frequency at 50Hz. As in previous transients, the wind turbines have to absorb the reactive power excess compensation provided by the capacitor and filter bank.

HVdc rectifier breaker trip and reclosure Figure 5.27 shows the response of the control system to a sudden trip of the HVdc rectifier ac-breaker and its subsequent reclosure. At $t = 20ms$ the HVdc rectifier ac-breaker trips, disconnecting the rectifier and the transformer banks from the offshore ac-grid. As a consequence of the disconnection, the offshore ac-grid voltage (V_{Fd}) is no longer limited by the HVdc diode rectifier and it increases up to 1.22pu. After approximately $40ms$ the control system drives (V_{Fd}) to its reference value (1.1pu). Note the decrease of the HVdc link current (I_{Rdc}) and the front-end active currents. At the same time, the front-end reactive current increases to compensate for the capacitor bank overcompensation, now that the HVdc rectifier is not conducting.
At $t = 70ms$ the HVdc breaker is reclosed and, after a transient lasting approximately $50ms$, normal operation is resumed with rated active power transmission. The offshore ac-grid voltage (V_{Fd}) is again being determined by the HVdc link inverter. During the whole transient, both active and reactive currents are adequately shared amongst all the front-end inverters.

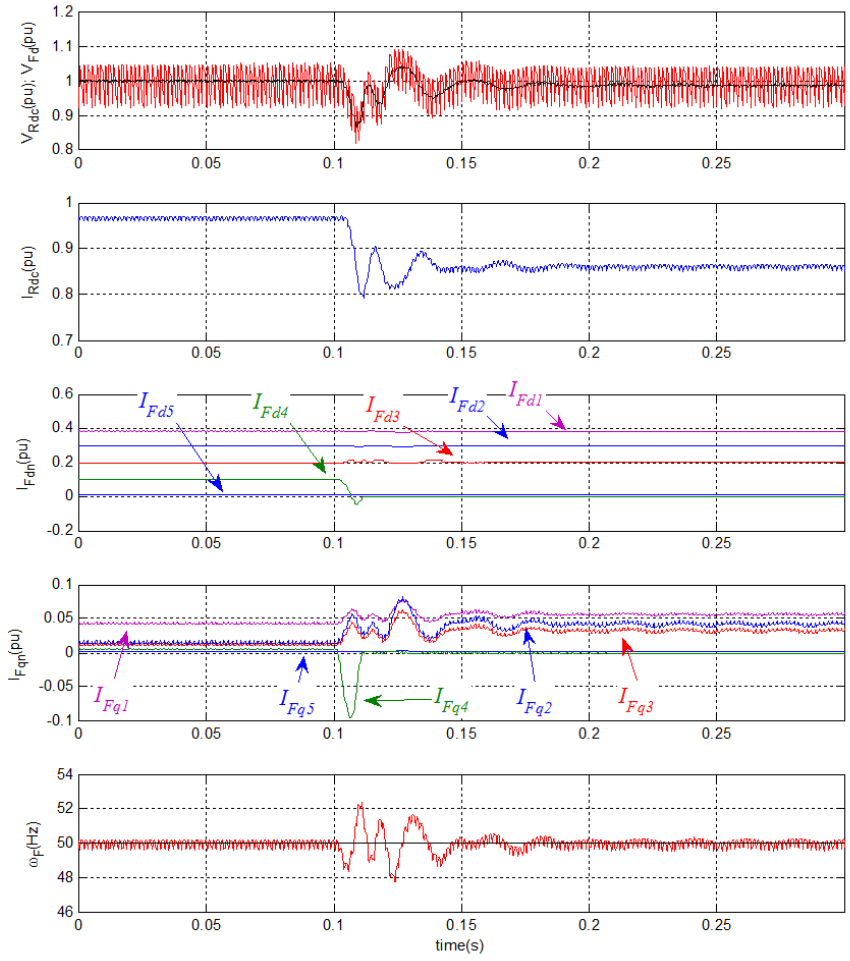

Figure 5.26: Response to a sudden disconnection of 10% of the wind turbines

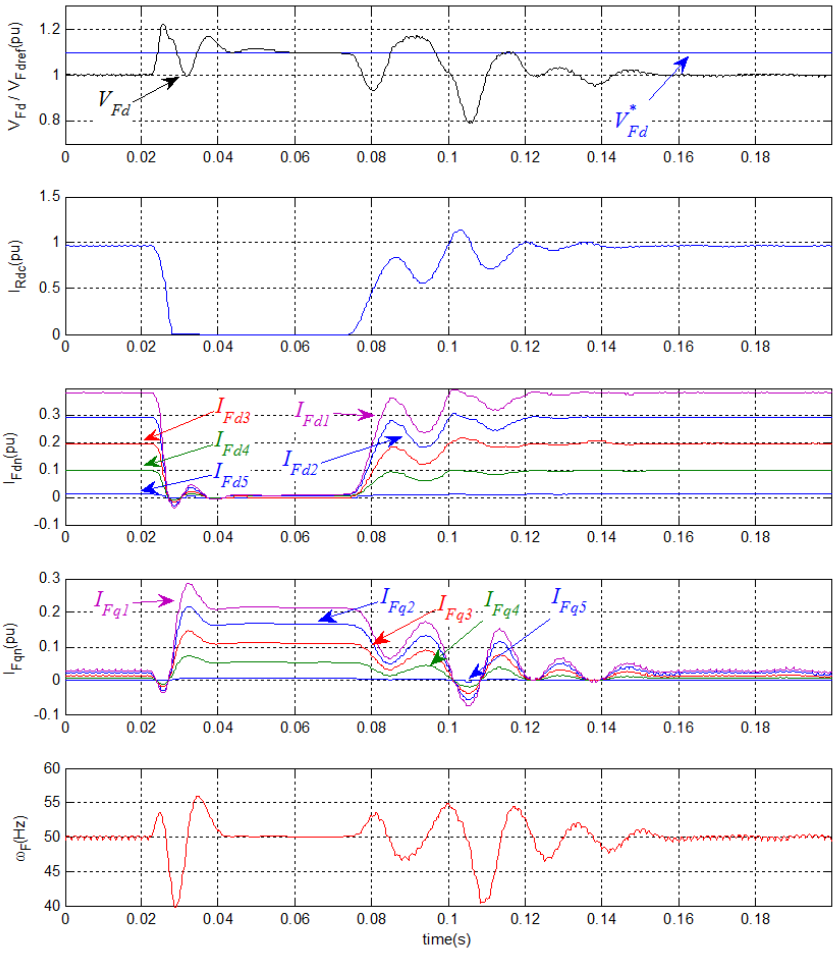

Figure 5.27: Response to a HVdc rectifier ac-breaker trip and reclosure

5.5 Summary

This chapter has been focused on the study of a clustered model on an offshore wind farm. The main goal has been to extend the strategies used to control the aggregated model to this distributed case. As in the aggregated model, the total power generated has been delivered to the onshore grid by means of an HVdc transmission system based on diode rectifiers. But, in contrast, this system has included multiple wind turbines feeding a point of common coupling (PCC).

A clustered model of the offshore wind farm has been used. In this model all the wind turbines belonging to the offshore wind farm have been lumped in a finite number of small aggregated models or clusters. The rated power of each cluster is equivalent to the sum of the rated power of all wind turbines included into it.

According to this model the control strategies shown in chapter 4 have been modified. Firstly, it has been assumed an adequate control of the dc-link voltage associated to the power converter of each cluster. Consequently, the dynamics of the rotor, the generator and the back-end power converter have been replaced by a constant dc-link voltage. Secondly, distributed voltage and frequency control loops have been developed to perform its integration to the offshore ac-grid. This has been due to the fact that the power dynamics of the (PCC) depends on the dynamics of each cluster.

Considering the conduction state of the HVdc link, it has been contemplated both, islanded mode of operation and connected mode of operation. On one hand, in islanded mode of operation and during the transition to connected mode, the front-end converters of each cluster have been employed coordinately to set the voltage and frequency of the offshore ac-grid. But, on the other hand, during connected mode of operation the voltage of the offshore ac-grid is clamped by the HVdc inverter. Therefore the front-end converters of each cluster have been employed coordinately to set the power (P and Q) delivered to the offshore ac-grid.

Similarly to chapter 4, the system stability analysis has been carried out for both operation modes. During the analysis different values of (C_F) and (ω_F) have been used to represent the parametric uncertainty due to both, filter bank switching and frequency flickers. As a result, the analysis of the poles location has shown the

robustness of the controller against variations of (C_F) and (ω_F). Finally, the last section of this chapter has described clearly the validation of the proposed strategies. The results have been obtained during steady state and transient functioning by means of PSCAD simulations.

CHAPTER 6

Conclusions and Future Works

6.1 Conclusions

6.1.1 More relevant information

This dissertation has contributed to demonstrate the technical feasibility of HVdc links with a diode-based rectifier. However, important changes related to the typical strategies used to control the wind turbines have had to be carried out. In previous chapters it has been described step by step not only the followed procedure, but also the proposed strategies and the obtained results. According to these results, the more relevant information obtained during the development of the project can be summarized as follows :

In chapter 1, the offshore wind energy trends have been analyzed. According to the last projected offshore wind farms, a clear trend has been found with respect to the offshore wind energy. This trend shows that the next generation of offshore wind farms will be larger, located in deeper waters and faraway from the coastline. In addition they will be conformed by wind turbines based on PMSG and fully rated converters.

In chapter 2, the model of the entire offshore wind farm has been developed. Dur-

ing this chapter, it has been shown that depending on the electrical dynamic to be studied, the offshore wind farm could be analyzed based on three approaches. The first approach is based on the reduction of the model complexity by using an aggregated model. The second approach uses a distributed model of the wind farm, and it is used for the analysis of wind turbines during simultaneous operation. The third approach is the clustered model of the offshore wind farm. This corresponds to an intermediate solution to obtain a reduced model of the entire wind farm that can be analyzed during simultaneous operation.

Moreover, the offshore wind farm is connected to an HVdc link. The model of this power transmission system has been based on the CIGRE Benchmark model for HVdc studies. According to this model it has been demonstrated that the power dynamics of a diode-based HVdc link is mainly dominated by the value of the current passing through the rectifier. Therefore, three operational zones have been defined according to the conduction constraints imposed by the diode rectifier. These zones correspond to operational modes that shall be contemplated in order to perform the grid integration of the wind turbine. The operational modes defined for the offshore wind farm are: Islanded operation mode, connecting operation mode with rectifier voltage control and connecting operation mode with rectifier current control.

In chapter 3 the wind turbine control strategy is analyzed with regards to the restrictions imposed by the non-controlled rectifier. According to this chapter the main drawback of using a diode-based HVdc rectifier station corresponds to the fact that offshore ac-grid is no longer controlled by the rectifier. However, this lack of control can be overcome by using an adequate control on the wind turbines converters. Therefore, this chapter is focused on dividing the tasks of the power converter. On one hand, the back-end converter is used to set the dc-link voltage. Whereas, on the other hand, the front-end converter is used to set both, the offshore ac-grid voltage and frequency.

Finally, this chapter also describes the different operation modes that have to be contemplated. This shows that the system can operate in three different modes depending of the conduction condition of the HVdc diode rectifier. Therefore, three strategies have been proposed to perform the offshore ac-grid control during islanded

and connected mode of operation.

First, in islanded operation mode, the offshore ac-grid dynamics is well known and dominated by the HVdc capacitor and filter bank. But, the diode rectifier is not conducting in this operation mode. Therefore, the control strategy is focused on regulating the offshore ac-grid voltage.

Second, in connecting operation mode with rectifier voltage control, the ac-grid voltage overcomes the conduction condition of the diode rectifier. However, the current passing through the rectifier is not large enough to reach the maximum current limit defined by the rectifier. Therefore, the control strategy is focused on performing a smooth transition between of the offshore ac-voltage defined by the islanded operation mode and the voltage imposed by the conduction of the diode based HVdc rectifier.

Third, in connecting operation mode with rectifier current control, the ac-grid voltage overcomes the conduction condition of the diode rectifier. In addition, the current passing through the rectifier reaches the maximum value defined by the rectifier. Therefore, the control strategy is focused on limiting the current delivered by each wind turbine according to both, the optimal power tracking and protection strategies.

6.1.2 More relevant contributions

Latest trends have shown that depending of the wind farm size and its distance to the coastline, the best economical solution for bulk power transmission is based on the HVdc technologies. Under these assumptions it is possible to consider the offshore wind farms as power plants with unidirectional power flow. Therefore, the HVdc links with diode based rectifier are introduced as a feasible alternative to the traditional thyristor-based rectifier. Additionally, this research also found that by using new control strategies it is possible to eliminate not only the transformer tap changer, but also, the external voltage and the reactive compensation. In chapter 4 and 5 the stand-alone and the distributed control strategies have been proved. According to the obtained results it is possible to highlight the following characteristics:

Offshore ac-grid Self-Start Capability

During islanded operation mode, the HVdc diode rectifier is not able to start the offshore ac-grid by itself. However, it has been shown that the offshore ac-voltage

can be smoothly set with the proposed strategy. Therefore, it is possible to carry out the grid forming task. This additional characteristic fulfils the self-start requirement often cited as an important shortcoming of the LCC-HVdc technologies in comparison with VSC-HVdc technologies.

Voltage and Current control mode

In connected mode of operation, it is possible to operate the wind farm and the HVdc diode rectifier focusing either, on setting the voltage or on setting the current at the dc-terminals of the HVdc rectifier. This behavior is similar to industrial practice in LCC-HVdc links.

Fault protection capability

By limiting the current references in the front-end converters, it is possible to implement a fault protection strategy similar to the standard VDCOL strategies. In addition, this strategy could keep the devices within their operational limits in presence of faults, with recovery times comparable to those achieved with controlled HVdc rectifiers. Moreover, by using this protection strategy the control system reacts adequately to substantial generation disconnection, capacitor bank switching and HVdc rectifier ac-breaker tripping and reclosure.

The aforementioned contributions have been validated by means of simulations considering both aggregated and clustered models of the offshore wind farm.

6.2 Future Works

As mentioned before, this dissertation has been based mainly on the control of the offshore wind farm. Nonetheless, once proved the technical feasibility of the HVdc diode rectifier, the following aspects have been proposed in order to be assessed in future projects.

- **The optimization of the power system dynamics.** According to the proposed systems the STATCOM has been eliminated, and both filter and capacitor bank have been reduced. Therefore, the control strategy should be focused on maximizing the energy production with an optimal regulation of the active and reactive power.

- **A more broad research to perform a complete structural analysis of the wind turbines.** By means of this analysis will be possible to define a control design procedure that consider not only the power dynamics, but also the ultimate and fatigue loading of the wind turbines components.

- **A detailed economical feasibility based on the cost of energy.** According to this analysis the savings obtained by using diode bridges (efficiency, losses, components, structures, equipment, maintenance, etc.) should be considered. In addition, this analysis could provide the possibility of comparing quantitatively the price per KWH with regards to any other power generation system.

- **A robust control strategy for the offshore ac-frequency (ω_F).** Clearly, whereas changes on (C_F) have little effects on the position of the closed loop eigenvalues; changes on (ω_F) decrease the damping of the dominant poles. So, a robust control strategy could guarantee controllers operating adequately in a wide range of frequencies.

BIBLIOGRAPHY

[1] N. B. Negra, J. Todorovic, and T. Ackermann, "Loss evaluation of HVAC and HVDC transmission solutions for large offshore wind farms," *Electric Power Systems Research*, vol. 76, no. 11, pp. 916 – 927, 2006.

[2] P. Kundur, N. J. Balu, and M. G. Lauby, *Power system stability and control*. McGraw-Hill, Jan. 1994.

[3] J. Arrillaga, Y. H. Liu, and N. R. Watson, *Flexible power transmission: the HVDC options*.
John Wiley and Sons, Nov. 2007.

[4] J. Bowles, "Multiterminal HVDC transmission systems incorporating diode rectifier stations," *Power Apparatus and Systems, IEEE Transactions on*, vol. PAS-100, no. 4, pp. 1674–1678, 1981.

[5] S. Hungsasutra and R. Mathur, "Unit connected operator with diode valve rectifier scheme," *Power Systems, IEEE Transactions on*, vol. 4, no. 2, pp. 538–543, 1989.

[6] R. Blasco-Gimenez, S. Ano-Villalba, J. Rodriguez-D'Derlee, S. Bernal-Perez, and F. Morant, "Diode-based HVdc link for the connection of large offshore wind farms," *IEEE Transactions on Energy Conversion*, vol. 26, pp. 615 –626, June 2011.

[7] R. Blasco-Gimenez, S. Ao-Villalba, J. Rodriguez-D'derlee, F. Morant, and S. Bernal-Perez, "Distributed voltage and frequency control of offshore wind farms connected with a diode-based HVdc link," *IEEE Transactions on Power Electronics*, vol. 25, pp. 3095 –3105, Dec. 2010.

[8] M. Liserre, R. Cardenas, M. Molinas, and J. Rodriguez, "Overview of multi-MW wind turbines and wind parks," *IEEE Transactions on Industrial Electronics*, vol. 58, pp. 1081 –1095, Apr. 2011.

[9] A. D. Hansen and G. Michalke, "Multi-pole permanent magnet synchronous generator wind turbines' grid support capability in uninterrupted operation during grid faults," *IET Renewable Power Generation*, vol. 3, pp. 333–348, Sept. 2009.

[10] R. Blasco-Gimenez, S. Ano-Villalba, J. Rodriguez, F. Morant, and S. Bernal, "Uncontrolled rectifiers for HVDC connection of large off-shore wind farms," in *Power Electronics and Applications, 2009. EPE '09. 13th European Conference on*, pp. 1–8, 2009.

[11] R. Blasco-Gimenez, S. Ano-Villalba, J. Rodriguez, V. Aldana, A. Correcher, F. Morant, and E. Quiles, "Variable voltage off-shore distribution network for wind farms based on synchronous generators," in *Electricity Distribution - Part 1, 2009. CIRED 2009. 20th International Conference and Exhibition on*, pp. 1–4, 2009.

[12] R. Blasco-Gimenez, S. Ao-Villalba, J. Rodriguez, V. Aldana, S. Bernal, and F. Morant, "HVDC connection of off-shore wind farms based on synchronous generators," in *Sustainable Alternative Energy (SAE), 2009 IEEE PES/IAS Conference on*, pp. 1–5, 2009.

[13] N. Fichaux and J. Wilkes, "Oceans of opportunity - harnessing europes largest domestic energy resource," Sept. 2009.

[14] T. Ackermann, *Wind power in power systems*.
John Wiley and Sons, 2005.

[15] D. Energy, S. Vattenfall, and D. S.-o. naturstyrelsen, *Danish offshore wind: key environmental issues*.
Published by DONG Energy, Vattenfall, the Danish Energy Authority and the Danish Forest and Nature Agency, 2006.

[16] Hyong Sik Kim and D. D.-C. Lu, "Wind energy conversion system from electrical PerspectiveA survey," *Smart Grid and Renewable Energy*, vol. 1, no. 3, pp. 119–131, 2010.

[17] H. Li and Z. Chen, "Overview of different wind generator systems and their comparisons," *Renewable Power Generation, IET*, vol. 2, no. 2, pp. 123–138, 2008.

[18] F. D. Bianchi, H. D. Battista, and R. J. Mantz, *Wind turbine control systems: principles, modelling and gain scheduling design*.
Springer, 2007.

[19] H. Polinder, F. Van Der Pijl, G.-J. De Vilder, and P. Tavner, "Comparison of direct-drive and geared generator concepts for wind turbines," *IEEE Transactions on Energy Conversion*, vol. 21, pp. 725–733, Sept. 2006.

[20] L. H. Hansen, L. Helle, F. Blaabjerg, E. Ritchie, S. Munk, H. Bindner, P. Srensen, B. Bak-jensen, A. Daniela, H. Peter, and H. Madsen, "Ris-r-1205(EN) conceptual survey of generators and power electronics for wind turbines," *NREL Report*, 2001.

[21] Z. Chen, J. Guerrero, and F. Blaabjerg, "A review of the state of the art of power electronics for wind turbines," *Power Electronics, IEEE Transactions on*, vol. 24, no. 8, pp. 1859–1875, 2009.

[22] R. Melicio, V. Mendes, and J. Catalao, "Harmonic assessment of variable-speed wind turbines considering a converter control malfunction," *Renewable Power Generation, IET*, vol. 4, no. 2, pp. 139–152, 2010.

[23] R. Melcio, V. Mendes, and J. Catalo, "Comparative study of power converter topologies and control strategies for the harmonic performance of variable-

speed wind turbine generator systems," *Energy*, vol. 36, pp. 520–529, Jan. 2011.

[24] S. Kouro, M. Malinowski, K. Gopakumar, J. Pou, L. G. Franquelo, B. Wu, J. Rodriguez, M. A. Perez, and J. I. Leon, "Recent advances and industrial applications of multilevel converters," *Industrial Electronics, IEEE Transactions on*, vol. 57, no. 8, pp. 2553–2580, 2010.

[25] R. Melcio, V. Mendes, and J. Catalo, "Power converter topologies for wind energy conversion systems: Integrated modeling, control strategy and performance simulation," *Renewable Energy*, vol. 35, pp. 2165–2174, Oct. 2010.

[26] R. W. Erickson, S. Angkititrakul, and K. Almazeedi, *A new family of multilevel matrix converters for wind energy applications.*
NREL Report - National Renewable Energy Laboratory, 2006.

[27] J. Arrillaga, *High voltage direct current transmission.*
IET, 1998.

[28] C. W. G. 14.29, *Coordination of controls of multiple FACTS/HVDC links in the same system*, vol. CIGRE REPORT 149.
CIGRE, 1999.

[29] K. Kanngiesser, H. Huang, H. Lips, N. Cristl, and G. Wild, *HVDC systems and their planing.*
SIEMENS AG, PTD H 1T, rev.4 ed., 1994.

[30] M. Davies, M. Dommaschk, J. Dorn, J Lang, D. Retzmann, and D. Soerangr, "HVDC PLUS - basics and principle of operation," *Answer for energy SIEMENS AG*, 2009.

[31] M. P. Bahrman and B. K. Johnson, "The ABCs of HVDC transmission technologies," *IEEE Power and Energy Magazine*, vol. 5, pp. 32–44, Apr. 2007.

[32] A. GRID, "HVDC-VSC: transmission technology of the future," *Think Grid N 8 (Spring - Summer) - Alstom Grid Magazine - France*, 2011.

[33] C. Du, M. H. Bollen, E. Agneholm, and A. Sannino, "A new control strategy of a VSCHVDC system for high-quality supply of industrial plants," *IEEE Transactions on Power Delivery*, vol. 22, pp. 2386–2394, Oct. 2007.

[34] C. Du, E. Agneholm, and G. Olsson, "Use of VSC-HVDC for industrial systems having onsite generation with frequency control," *IEEE Transactions on Power Delivery*, vol. 23, pp. 2233–2240, Oct. 2008.

[35] T. Machida, I. Ishikawa, E. Okada, and E. Karasawa, "Control and protection of HVDC systems with diode valve converter," *Electrical Engineering in Japan*, vol. 98, no. 1, pp. 62–70, 1978.

[36] S. Heier, *Grid integration of wind energy conversion systems*. Wiley, May 2006.

[37] J. Conroy and R. Watson, "Aggregate modelling of wind farms containing full-converter wind turbine generators with permanent magnet synchronous machines: transient stability studies," *Renewable Power Generation, IET*, vol. 3, no. 1, pp. 39–52, 2009.

[38] V. Akhmatov and H. Knudsen, "An aggregate model of a grid-connected, large-scale, offshore wind farm for power stability investigations–importance of windmill mechanical system," *International Journal of Electrical Power & Energy Systems*, vol. 24, pp. 709–717, Nov. 2002.

[39] M. Szechtman, T. Wess, and C.V. Thio, "First benchmark model for HVDC control studies," *Electra*, vol. 135, no. 4, pp. 54–73, 1991.

[40] S. Bozhko, R. Blasco-Gimenez, R. Li, J. Clare, and G. Asher, "Control of offshore DFIG-Based wind farm grid with line-commutated HVDC connection," *Energy Conversion, IEEE Transactions on*, vol. 22, no. 1, pp. 71–78, 2007.

[41] R. Li, S. Bozhko, and G. Asher, "Frequency control design for offshore wind farm grid with LCC-HVDC link connection," *Power Electronics, IEEE Transactions on*, vol. 23, no. 3, pp. 1085–1092, 2008.

[42] K. Z. stergaard, J. Stoustrup, and P. Brath, "Linear parameter varying control of wind turbines covering both partial load and full load conditions," *Inter-*

national Journal of Robust and Nonlinear Control, vol. 19, pp. 92–116, Jan. 2009.

[43] K. Selvam, S. Kanev, J. W. van Wingerden, T. van Engelen, and M. Verhaegen, "Feedbackfeedforward individual pitch control for wind turbine load reduction," *International Journal of Robust and Nonlinear Control*, vol. 19, pp. 72–91, Jan. 2009.

[44] R. Pena, J. C. Clare, and G. M. Asher, "Doubly fed induction generator using back-to-back PWM converters and its application to variable-speed wind-energy generation," *Electric Power Applications, IEE Proceedings* -, vol. 143, pp. 231–241, May 1996.

[45] R. Cardenas, R. Pena, G. M. Asher, J. Clare, and R. Blasco-Gimenez, "Control strategies for power smoothing using a flywheel driven by a sensorless vector-controlled induction machine operating in a wide speed range," *IEEE Transactions on Industrial Electronics*, vol. 51, pp. 603– 614, June 2004.

[46] M. Chinchilla, S. Arnaltes, and J. C. Burgos, "Control of permanent-magnet generators applied to variable-speed wind-energy systems connected to the grid," *IEEE Transactions on Energy Conversion*, vol. 21, pp. 130– 135, Mar. 2006.

[47] M. C. Chandorkar, D. M. Divan, and R. Adapa, "Control of parallel connected inverters in standalone AC supply systems," *IEEE Transactions on Industry Applications*, vol. 29, pp. 136–143, Feb. 1993.

[48] R. H. Lasseter and P. Paigi, "Microgrid: a conceptual solution," in *Power Electronics Specialists Conference, 2004. PESC 04. 2004 IEEE 35th Annual*, vol. 6, pp. 4285– 4290 Vol.6, IEEE, June 2004.

[49] F. D. Kanellos and N. D. Hatziargyriou, "Control of variable speed wind turbines in islanded mode of operation," *IEEE Transactions on Energy Conversion*, vol. 23, pp. 535–543, June 2008.

[50] N. Pogaku, M. Prodanovic, and T. C. Green, "Modeling, analysis and testing of autonomous operation of an inverter-based microgrid," *IEEE Transactions*

on Power Electronics, vol. 22, pp. 613–625, Mar. 2007.

[51] T. Green and M. Prodanovi, "Control of inverter-based micro-grids," *Electric Power Systems Research*, vol. 77, no. 9, pp. 1204 – 1213, 2007.

[52] C. K. Sao and P. W. Lehn, "Control and power management of converter fed microgrids," *IEEE Transactions on Power Systems*, vol. 23, pp. 1088–1098, Aug. 2008.

[53] I. J. Balaguer, Q. Lei, S. Yang, U. Supatti, and F. Z. Peng, "Control for grid-connected and intentional islanding operations of distributed power generation," *IEEE Transactions on Industrial Electronics*, vol. 58, pp. 147–157, Jan. 2011.

[54] F. Iov, A. Hansen, P. Srensen, and N. Cutululis, "A survey of interconnection requirements for wind power," *Proceedings of Nordic Wind Power Conference, NWPC 2007*, Dec. 2010.